DIC and Cohesive FE-analysis of glulam beams with two large, circular holes

PHILIP NYGREN

SUPERVISORS

Vidar Hellum, Assistant professor at University of Agder, Grimstad.

Dag Pasquale Pasca, Researcher at the Norwegian Institute of Wood Technology.

University of Agder, 2022

Faculty of Engineering and Science

Department of Engineering Sciences

Obligatorisk egenerklæring/gruppeerklæring

Den enkelte student er selv ansvarlig for å sette seg inn i hva som er lovlige hjelpemidler, retningslinjer for bruk av disse og regler om kildebruk. Erklæringen skal bevisstgjøre studentene på deres ansvar og hvilke konsekvenser fusk kan medføre. Manglende erklæring fritar ikke studentene fra sitt ansvar.

1.	Jeg/vi erklærer herved at min/vår besvarelse er mitt/vårt eget arbeid, og at jeg/vi ikke har brukt andre kilder eller har mottatt annen hjelp enn det som er nevnt i besvarelsen.	☒
2.	Jeg/vi erklærer videre at denne besvarelsen: - ikke har vært brukt til annen eksamen ved annen avdeling/universitet/høgskole innenlands eller utenlands. - ikke refererer til andres arbeid uten at det er oppgitt. - ikke refererer til eget tidligere arbeid uten at det er oppgitt. - har alle referansene oppgitt i litteraturlisten. - ikke er en kopi, duplikat eller avskrift av andres arbeid eller besvarelse.	☒
3.	Jeg/vi er kjent med at brudd på ovennevnte er å betrakte som fusk og kan medføre annullering av eksamen og utestengelse fra universiteter og høgskoler i Norge, jf. Universitets- og høgskoleloven §§4-7 og 4-8 og Forskrift om eksamen §§ 31.	☒
4.	Jeg/vi er kjent med at alle innleverte oppgaver kan bli plagiatkontrollert.	☒
5.	Jeg/vi er kjent med at Universitetet i Agder vil behandle alle saker hvor det foreligger mistanke om fusk etter høgskolens retningslinjer for behandling av saker om fusk.	☒
6.	Jeg/vi har satt oss inn i regler og retningslinjer i bruk av kilder og referanser på biblioteket sine nettsider.	☒

Publiseringsavtale

Fullmakt til elektronisk publisering av oppgaven

Forfatter(ne) har opphavsrett til oppgaven. Det betyr blant annet enerett til å gjøre verket tilgjengelig for allmennheten (Åndsverkloven. §2).

Alle oppgaver som fyller kriteriene, vil bli registrert og publisert i Brage Aura og på UiA sine nettsider med forfatter(ne)s godkjennelse.

Oppgaver som er unntatt offentlighet eller taushetsbelagt/konfidensiell vil ikke bli publisert.

Jeg/vi gir herved Universitetet i Agder en vederlagsfri rett til å

gjøre oppgaven tilgjengelig for elektronisk publisering: ☒JA ☐NEI

Er oppgaven båndlagt (konfidensiell)? ☐JA ☒NEI

(Båndleggingsavtale må fylles ut)

- Hvis ja:

Kan oppgaven publiseres når båndleggingsperioden er over? ☒JA ☐NEI

Er oppgaven unntatt offentlighet? ☐JA ☒NEI

(inneholder taushetsbelagt informasjon. Jfr. Offl. §13/Fvl. §13)

Preface

This master's thesis was conducted at the University of Agder, in Norway, at the Faculty of Engineering and Science, Grimstad. It is written in the spring of 2022 as the concluding work of the master's in the civil engineering program, weighing 30 ECTS points. The present work would not have been possible without help and assistance from the involved people.

The author greatly acknowledges the advisory and assistance from his supervisor at the Norwegian Institute of Wood Technology, Dr. Eng. researcher Dag Pasca, who introduced the theme and was available for guidance throughout this project. In addition, the general advice by Assoc. Prof. Vidar Hellum at the University of Agder regarding the thesis and planning is appreciated.

The funding of materials by the Norwegian Institute of Wood Technology, Kjellstad Trelast AS, and the University of Agder made this project possible and is acknowledged by the author.

The author would like to express his gratitude to Harald Sauvik and Cecilie Ødegård (UiA) at the Mechatronics laboratory for your thorough help in developing a setup for the experiments, which proved to be much more time consuming than expected. Thank you for being so patient.

Anette Heimdal and Ingrid Lande (UiA), who provided help and expertise regarding Digital Image Correlation setup and methodology, are greatly appreciated. The author thanks Sigurd K. Brinch (UiA) for the technical assistance in setting up the virtual server to conduct numerical analyses more efficiently.

Thank you, Mohtasham Ghaderi (Agder Fylkeskommune) and Olav Osa (Mesta AS), for the loan of concrete road elements used in the experiments, and Assoc. Prof. Ephrem Taddesse (UiA), who established the contact with them. Urdal Services AS provided a free-of-cost loan of the Linear Variable Differential Transducer (LVDT). Thank you for this, Jan Ove Urdal.

Technical guidance through e-mail correspondence from Robert Weiß (Correlated Solutions) and the author of ACDM, Nicola Gehri (ETH Zürich), is appreciated.

I wish to thank my wife, Anette, for enduring the difficult times throughout the past five years, especially the last seven months since our son was born, for being critical of my work when needed and pushing me to achieve my goals. At last, I would like to thank my son, Max, for giving me joy every day.

_____

Philip Nygren

27th of May 2022 - Grimstad

Abstract

Introducing a large hole into a load-bearing timber beam causes stress concentrations in the hole vicinity. Tensile stress perpendicular to the grain presents a particular crack initiation and propagation risk. Unfortunately, beam design with holes is not integrated into the current Eurocode 5, even though research has proven that reinforcement can prevent premature failure of holes with a diameter up to 40 % of beam height. This thesis has addressed even bigger holes by analyzing the fracture behavior of holes constituting 57 % of beam height. Four glulam beam experiments utilizing a standard four-point bending setup, each with two consecutive large circular cavities within the shear and moment region. Two of the beams had glued-on plywood reinforcement. High-resolution images got captured utilizing a dual-camera Digital Image Correlation (DIC) setup to study displacement fields in an area surrounding the holes. In addition, the ACDM tool automatically detected cracks by DIC-data, which enabled the computing of the crack length in MATLAB. Moreover, a Finite Element (FE) model was created in ABAQUS with cohesive layers to apply non-linear fracture mechanics considerations to the model, with a bilinear traction-separation behavior.

The analysis of the two unreinforced beams uncovers crack initiation to begin at the hole closest to the support, at an approximate inclination of 45°, caused by tension perpendicular to the grain. The two reinforced specimens did not experience crack development near holes, and failure was due to tensile bending in the middle of the beams. The numerical FE-analysis overestimates capacity when using an initial, literature-based guess of parameters, and subsequently, cracks initiate at a later loading stage compared to the experiments. Although this is not validated, reducing crack initiation capacity in fracture modes I and II will reduce the difference between model and experiments. Therefore, a model-updating procedure is suggested based on a stochastic optimization algorithm identifying the error between the model's DIC-measured strain-field points and crack length. More research is necessary to validate the proposed procedure and larger sample sizes to conclude if reinforcement of large holes can retain its strength as if the beams would have been intact.

Table of contents

List of figures

List of tables

Abbreviations and symbols

Word	Explanation
UN	United Nations
GHG	greenhouse gas
CO_2-eq.	carbon-dioxide equivalents (used to express emissions)
DIC	digital image correlation
GDP	gross domestic product
LCA	life cycle assessment
CLT	cross-laminated timber
GLT	glue-laminated timber
Glulam	glued laminated timber
C3D8R	continuum 3D eight-node element with reduced integration (brick mesh type)
FM	fracture mechanics
LVL	laminated veneer lumber
LEFM	linear-elastic fracture mechanics
NLFM	non-linear fracture mechanics
LVDT	linear variable differential transducer
ABAQUS	finite element analysis software
OSB	oriented strand board
VIC-3D	digital image correlation software to analyze high-quality photographs
ACDM	automated crack detection and measurement software
MOE	modulus of elasticity
FOV	field of view
AOI	area of interest
FE	finite element
FEM	finite element method
FEA	finite element analysis
CPU	central processing unit
GPU	graphics processing unit
BDSTAT	bond state of a cohesive node in ABAQUS
SCZM	surface cohesive zone model

List of symbols

Symbols throughout the thesis are listed here and in the text the first time they are mentioned, with explanations below.

Misc.	Explanation
$(\boldsymbol{L}, \boldsymbol{R}, \boldsymbol{T})$	*local coordinate system (timber directions)*
$(\boldsymbol{n}, \boldsymbol{s}, \boldsymbol{t})$	*local coordinate system (fracture mechanics)*
$(\boldsymbol{x}, \boldsymbol{y}, \boldsymbol{z})$	*global coordinate system*
$(\mathbf{1}, \mathbf{2}, \mathbf{3})$	*global coordinate system*
$\boldsymbol{i}, \boldsymbol{j}, \boldsymbol{k}, \boldsymbol{l}$	*replacement variables*
$\boldsymbol{M}, \boldsymbol{N}, \boldsymbol{O}, \boldsymbol{P}$	*integer variables*

Latin	Explanation	Unit
$\boldsymbol{a}$	*crack length*	$[\mathrm{mm}]$
$\boldsymbol{b}$	*breadth of a beam*	$[\mathrm{mm}]$
$\boldsymbol{b_r}$	*reinforcement edge to hole edge, distance*	$[\mathrm{mm}]$
$[\boldsymbol{C}]$	*compliance matrix*	$[-]$
$\boldsymbol{D}$	*damage variable*	$[-]$
$\boldsymbol{D_v}$	*viscous stiffness degradation variable*	$[-]$
$[\boldsymbol{D}]$	*stiffness matrix*	$[-]$
$\boldsymbol{F_{max}}$	*the maximum force applied to a specimen*	$[\mathrm{N}]$
$\boldsymbol{F_{t,90,Ed}}$	*total tensile stress perpendicular to the grain*	$[\mathrm{N/mm^2}]$
$\boldsymbol{F_{t,90,Rd}}$	*design tensile strength perpendicular to the grain*	$[\mathrm{N/mm^2}]$
$\boldsymbol{F_{t,M,Ed}}$	*moment contribution to the total tensile stress*	$[\mathrm{Nm}]$
$\boldsymbol{F_{t,V,Ed}}$	*shear contribution to the total tensile stress*	$[\mathrm{N}]$
$\boldsymbol{f_{b2,d}}$	*design glue-line strength*	$[\mathrm{N/mm^2}]$
$\boldsymbol{f_{t,d}}$	*design tensile strength of the glued-on plate*	$[\mathrm{N/mm^2}]$
$\boldsymbol{G_I}$	*fracture energy in opening mode*	$[\mathrm{N/mm}]$
$\boldsymbol{G_{II}}$	*fracture energy in the first shearing mode*	$[\mathrm{N/mm}]$

G_{Ic}	*critical release rate in opening mode*	$[\mathrm{N/mm}]$
G_{IIc}	*critical release rate in the first shearing mode*	$[\mathrm{N/mm}]$
G_c	*elastic energy at damage traction maxima*	$[\mathrm{N/mm}]$
G_F	*total fracture energy*	$[\mathrm{N/mm}]$
G_{ij}	*moduli of rigidity (shear moduli)*	$[\mathrm{N/mm^2}]$
h	*height of a beam*	$[\mathrm{mm}]$
h_1	*distance from the top or bottom of the reinforcement the to hole edge*	$[\mathrm{mm}]$
K_k	*reduction factor related to hole-reinforcement*	-
L	*longitudinal*	-
L	*beam span*	$[\mathrm{mm}]$
L_0	*initial length*	$[\mathrm{mm}]$
l_{ad}	*distance from the top of plane reinforcement to the theoretical, potential crack line*	-
M	*bending moment*	$[\mathrm{Nm}]$
m	*first exponent*	-
m_{dry}	*the mass of a timber specimen in dry condition*	$[\mathrm{Kg}]$
m_{wet}	*the mass of a timber specimen with moisture content*	$[\mathrm{Kg}]$
m_ω	*mass of the moisture content*	$[\mathrm{Kg}]$
n	*second exponent*	-
n_r	*number of reinforcements*	-
R	*radial*	-
T	*tangential*	-
T	*traction (stress)*	$[\mathrm{N/mm^2}]$
T_m	*effective traction*	$[\mathrm{N/mm^2}]$
T_{max}	*traction maxima*	$[\mathrm{N/mm^2}]$
V	*shear force*	$[\mathrm{N}]$
V_ω	*the volume of a timber specimen at a specific moisture content*	$[\mathrm{m^3}]$

Greek	Explanation	Unit
α	*exponential coefficient*	$[-]$
ΔL	*change in length*	$[-]$
δ	*separation*	$[\mathrm{mm}]$
δ_c	*critical separation at traction maxima*	$[\mathrm{mm}]$
δ_e	*complete separation*	$[\mathrm{mm}]$
δ_m	*effective separation (combined of all relevant fracture modes)*	$[\mathrm{mm}]$
E_{ii}	*moduli of elasticity in a specific direction*	$[\mathrm{N/mm^2}]$
ε	*strain*	$[-]$
ε_{ij}	*strain tensor component*	$[-]$
μ	*viscosity coefficient*	$[-]$
v_{ij}	*directional Poisson's ratio of an orthotropic material*	$[-]$
ρ_ω	*the density of a timber specimen at a specific moisture content*	$[\mathrm{Kg/m^3}]$
σ	*stress*	$[\mathrm{N/mm^2}]$
σ_{ii}	*stress tensor component*	$[\mathrm{N/mm^2}]$
σ_{ini}	*crack (damage) initiation normal stress – mode I*	$[\mathrm{N/mm^2}]$
$\sigma_{t,90}$	*tensile stress perpendicular to the grain*	$[\mathrm{N/mm^2}]$
τ_{ij}	*shear stress tensor component*	$[\mathrm{N/mm^2}]$
τ_{ini}	*crack (damage) initiation shear stress – mode II*	$[\mathrm{N/mm^2}]$
φ	*angle*	$[^\circ]$
Ψ	*replacement parameter for orthotropic Poisson's ratio*	$[-]$
ω	*moisture content*	$[\%]$

1 Introduction

1.1 Background

Timber is a material with many advantages that exist in proximity in most areas of Europe. It is usually a short distance from the logging site to the building location. Its high strength-to-weight ratio is an important property to consider in structural design. Additionally, timber is a renewable and sustainable material with versatile usages and has a low energy demand. However, wood is complex in structural design due to its heterogeneous anisotropic properties such as knots, curvature, and growth rings. Natural phenomena such as moisture also significantly affect its strength and longevity.

Resistance to forces perpendicular to the grain is one of timber's weaknesses, particularly tension stress and shear. Cracks along grain direction account for approximately 75 % of structural failures in glued laminated timber out of 140 cases examined in 2007 . This category contains tension and shear failure perpendicular to the grain and cracks due to slip of glue line; however, some of these can be due to moisture-induced stresses. Another research [3] evaluated the failure reason on 245 large-span glued laminated timber beams, where 17 % of these subjects suffered damage from perpendicular to grain tension. Engineered timber products have a design to minimize stress in those directions when the element is intact. However, timber connections and beams that are either; curved, tapered or have notches and holes are especially prone to cracking due to tension and shear perpendicular to grain [2]. Figure 1.1 illustrates some situations that may experience this type of critical stress.

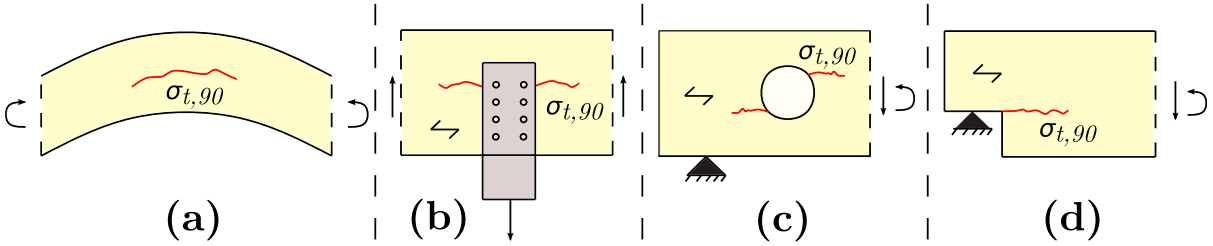

Figure 1.1: Sketch of critical zones susceptible to cracks by tension perpendicular to grain under certain loading conditions. (a) shows a curved beam, (b) mechanical connection with a tensile component, (c) beam with a hole, and (d) a notched beam end.

1.2 Problem area

Cutting holes in load-bearing beams are sometimes necessary to create a path for technical infrastructure, e.g., ventilation, plumbing, and electrical installations. In addition, cavities present a challenge of concentrated tension and compression stress at the hole vicinity, such that fracture mechanics principles apply. Moreover, researchers have often addressed fracture implications using linear-elastic and probabilistic approaches. However, recent methods with a non-linear nature, such as the cohesive zone model [4, 5] have proven to be efficient and closer to reality because of the ability to analyze the strain-softening behavior of crack evolution.

When structural beams have large holes, practitioners need to evaluate reinforcement options to prevent crack initiation and propagation so that the beam retains its original failure mode. Unfortunately, the primary design practice for timber, Eurocode 5 [8], does not include members with holes which is necessary to have equal design opportunities as concrete and steel structures [9].

The main objective is to investigate the fracture behavior of two consecutive holes in glulam beams and evaluate reinforcement options to prevent premature damage. This thesis will conduct experiments using established methods to interpret fracture behavior and compare it with a non-linear finite element model. Additional research on model-updating with the experimental data in mind is also within the scope of this thesis.

1.3 Current design practices

A previous version of the current Eurocode 5 (2004) included a section with holes based on an empirical linear elastic fracture mechanics method. However, experimental results proved this method inconsistent; thus, it was withdrawn [5]. Now that Eurocode 5 no longer covers beam members with holes, national annexes, handbooks, and individual reports have emerged to cover this gap. Unfortunately, these methods use significantly different theoretical material, such that there is a considerable variation in results , and it is, therefore, intricate to figure out which design criteria to choose. Nevertheless, there are plans to expand Eurocode 5 soon with a section that includes members with holes, with and without reinforcement [12].

Currently, the DIN-annex (Germany) [7] is possibly the most acknowledged of these additions. This annex is substantially implemented in the Nordic glulam handbooks [14] with minor adjustments (used in Finland, Norway, and Sweden). These guidelines set the hole diameter limitation to 50 mm for unreinforced hole zones. However, with reinforcement, the hole diameter can be increased to 30% of the beam height for internal and 40% for external reinforcement [14].

1.4 Thesis structure

- Chapter 1 introduces the main problem area and briefly mentions the current state-of-the-art design practices.
- Chapter 2 presents a broader perspective on the use of timber in general and how it can be related to achieving UN goals. The impact of glued laminated timber is reviewed compared to other common building materials based on literature.
- Chapter 3 presents basic theory regarding mechanical and physical timber properties. An evaluation of stress distribution around holes relative to hole placement is presented based on published literature, leading to an introduction to fracture mechanics, including the theory behind cohesive fracture zones. The progress regarding a new version of Eurocode 5 is revised. Next, a summary presents commonly used reinforcement types. This chapter shows the theoretical background for the test equipment used for the experiments. Lastly, a literature review regarding experiments on glulam beams with holes, with and without reinforcement, is listed.
- Chapter 4 presents the scope of the thesis in the form of research questions and the limitations. These questions are the main objectives to be answered throughout the following chapters.
- Chapter 5 presents materials used for experiments, including identification and pictures of heterogenous imperfections.

- Chapter 6 presents the experimental setup, methods used to obtain the results, and the finite element modeling steps.
- Chapter 7 presents the findings of the experimental and numerical work.
- Chapter 8 discusses the applied methods with the results' limitations, interpretations, and implications.
- Chapter 9 presents specific conclusions of the framework in this study.
- Chapter 10 presents the author’s recommendations for future research based on findings and shortcomings.

2 Societal perspective

This chapter is about UN goals related to this project and the sustainability of timber compared to other common building materials. The environmental factors evaluated include sustainable forest management and how it can contribute to sequestration of CO_2 emissions.

2.1 United Nations goals of decarbonization

Findings from research regarding human impact on the earth's atmosphere and biosphere have resulted in a dedicated focus on sustainability [15]. These consequences have led to a signed agreement within the United Nations, where the objective is a climate-neutral world by 2050. Therefore, it is vital to establish comprehensive policy frameworks and manage ecosystems sustainably to mitigate climate change and reach preindustrial levels of greenhouse gas emissions [16]. In 2019, the European Commission took specific measures to achieve this goal; hence, they formed the European Green Deal, parallel to the Paris Agreement [17]. Furthermore, one of United Nations goals - 12.2 is to manage our natural resources sustainably [18]. Therefore, the building industry must adapt to all the relevant UN goals by contributing across all segments while adapting to new regulations accordingly. The energy sector is the cause of around 75% of all greenhouse gas (GHG) emissions [19], and renewable energy is limited. Therefore, the building industry can contribute by opting for low energy-intensive materials to reach net-zero energy-related CO2 emissions by 2050.

Concrete and steel are the leading pollutants in the building industry, and materials from these industries are sometimes irreplaceable, which presents a challenge. Therefore, it is imminent to implement future solutions to decarbonize, e.g., sustainable bioenergy, because it is a source to remove CO_2 from the atmosphere. Although wood as a building material is not suited for every task or design, it plays a central role in sustainable energy supply to steel and concrete production and transportation as biofuel. The demand for bioenergy is estimated to go up 60 % within 2050 [19], and an increase in production will protect hotspots in biodiversity if managed correctly, achieving UN goal 15 [20]. CO_2-removal technologies can limit climate change, such as afforestation or direct absorption from forestry and carbon storage and capture through bioenergy production [19]. Wood plays an eminent factor in many sectors and has essential socio-economic functions. Society must transition towards a carbon-neutral, bio-based circular economy to accomplish sustainability goals [21].

2.1.1 Forest sustainability

UN has a specific goal of protecting forest ecosystems, 15.2 [22], which can be achieved by correctly utilizing sustainable harvest systems and management standards [23] to mitigate causes of forest destruction, like unsustainable industrial timber plantations [24]. Forest degradation and deforestation are a part of the global climate crisis, which accelerates biodiversity loss and global warming, accounting for 12% of the global net anthropogenic emissions annually [25]. An estimate from the past three decades shows that around 10% of the worldwide forest is gone because of deforestation [26]. In addition, the forest plays a crucial part in the global terrestrial carbon cycle by capturing and sequestration of carbon dioxide [27]. Therefore, keeping a sustainable regrowth rate contributes to decarbonization.

Reference [28] states that European forest areas have increased by 9% since 1990, which adds to a growing stock increase of 40 m^3/ha, as shown in Figure 2.1(a). Therefore, harvesting from a healthy

growing stock can provide sustainable materials that society needs. Figure 2.1(c) shows that only 73 % of the forest surplus is reduced annually [28]. Furthermore, forestry and afforestation contribute to decreased temperatures in the atmosphere [28], and the forests in the EU capture 155 million tonnes of carbon annually and act as a carbon sink, as shown in Figure 2.1(b), which is roughly 10% of gross anthropogenic GHG emissions.

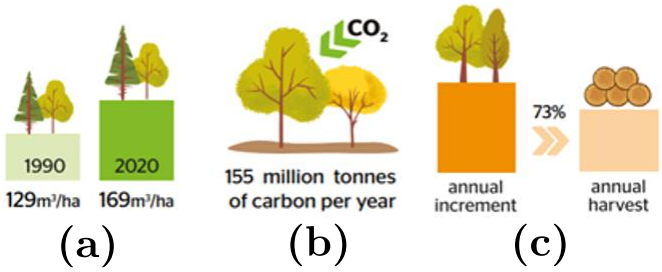

Figure 2.1: (a) Total growing stock per hectare on average in European forests between 1990-2020, (b) sequestration of carbon annually between 2010-2020 in Europe. Finally, (c) illustrates the annual growth in European forests vs. the harvest rate. The figures are from Ref. [28].

2.1.2 Norwegian forests

Norway has large amounts of timber available locally; hence short distances to processing factories and construction sites, which result in low climate impact from transportation. Norwegian growing stock has increased approximately 70% since 1990 [29], compared to Europe with a 9% increase in the same period [28]. The coniferous softwood species, Norway Spruce, can be sustainably regrown in approximately 40 years and then be ready to be harvested again [28]. In addition, it is the most common specie used to make structural timber, such as GLT. The government has set goals to increase forestry production, which aligns with the UN goals, and they have also expressed an interest in becoming leading innovators in raw wood products [30].

2.2 Comparative review of emissions related to three building materials

To accomplish the net-zero agreement, engineers and architects should ideally contribute by utilizing life cycle analyses (LCA) when selecting materials based on holistic environmental impact. Therefore, it is indispensable to have reliable, up-to-date research to make well-informed choices. When comparing the environmental impact of wood-based materials with steel and concrete, there is an emission reduction potential by replacing heavy energy-consuming products. In the steel and concrete industry, the total CO_2 and energy consumption are determined mainly by the demand for materials per capita, with close connections to economics. Over the last decades, the global increase in material demand has exceeded population growth and gross domestic product (GDP) growth [31]. Therefore, it is imperative to implement material efficiency strategies, such as carbon taxes, new technology, end of life reuse and recycling, and decoupling population growth and economics from the global material demand to decrease the environmental pressure [31]. Energy-heavy sectors like the concrete and steel industries have a complex task of decarbonizing because the total abatement cost is high per tonnes of CO_2 saved [32]. The Energy Transitions Commission report [32] shows a projection with the possibility of becoming climate neutral within 28 years, even for these hard-to-abate industries. However, the same report demonstrates that it will have a low effect on the consumer economy and cost approximately 5% of global GDP [32].

The following sections discuss the current impact of three environmental categories of structural building materials and the inclusion criteria of timber.

2.2.1 Timber net carbon savings

Calculating the climate impact is somewhat complex, and it depends on the scope of the analysis, especially in end-of-life circumstances. Nevertheless, a simplified procedure to calculate the net carbon savings can be as follows: **(i)** wood production; **(ii)** minus burning of the wood remains; **(iii)** minus stored carbon in the material; **(iv)** and minus the avoided emissions from alternative products like steel and concrete; and **(v)** represents total carbon net savings. Further elaboration is presented below, based on Ref. [33]:

(i) *Wood production, gross emissions from carbon = Biogenic CO_2 + Fossil CO_2*

The total energy consumption is related to raw material harvesting, transportation to the factory, and energy used in the manufacturing process. The emissions from these processes heavily depend on geographic location and energy source.

(ii) *Burning of wood remains, gross emissions from carbon = Biogenic CO_2*

In the manufacturing process of timber, left-over materials become a subproduct, e.g., bioenergy. Emissions from burning wood can be deducted since all carbon released initially stems from the atmosphere.

(iii) *Carbon storage in finished wood products*

Dry wood contains approximately half of its weight in carbon. Therefore, a common approach is to deduct the carbon stored in the wood, absorbed by photosynthesis.

(iv) *Avoided emissions from alternate products*

This accounts for the carbon emissions that are avoided by replacing a heavy energy-consuming material in favor of wood.

(v) *Carbon net savings*

This accounts for the net carbon emission savings from choosing wood instead of e.g. concrete or steel alternatives. Defining an appropriate functional unit is key to obtaining a basis for comparison, and for structural building materials, this could be bearing capacity. A negative carbon net savings indicate a reduction in climate impact.

2.2.2 Impact of glued-laminated timber

Recent research [34, 35] estimates that proper forest management can mitigate up to 60% of the logging impact compared to conventional logging. The energy consumption to produce 1 tonne of sawn wood is approximately 0,09 MWh/t [36]. According to Ref. [37], the freshwater consumption to make glulam is 1,1 m^3/t glulam (converted with the density assumption of 400 kg/m^3) in a cradle-to-gate perspective. Glulam contains 1-2% of its weight in glue, and 10% of the energy consumption is associated with raw materials needed for glue production [38]. GLT used in this project contains emulsion polymer isocyanate (EPI) adhesive, which has a GWP of 2 t CO_2-eq. [39], and water consumption of 0,6 m^3 per tonne of glue.

Given that forest management is carried out sustainably, the remaining forest's yearly carbon released from logging gets absorbed. As a result, the atmosphere will not have an increase in net CO_2 emissions. Living trees and timber products contain about 1 t CO_2/m^3 [40].

2.2.3 Impact of steel

Steel and iron industry sectors are amongst the leading contributors to the rise of CO_2 levels. They released approximately 3,6 Gt in 2019 [41], which equals 11 % of the total global emissions because they rely on fossil fuels. Crude steel production releases 1,9 t CO_2 emissions for every tonne of product manufactured, and the energy intensity from production is 5,6 MWh/t [42]. Additionally, it is important to consider other environmental factors, such as water footprint. Water scarcity is a global problem due to increased urbanization, industrialization, and population growth. The freshwater intensity for steel is approximately 3,3m^3 per tonne of finished product [43].

Various LCA methodologies were considered in Ref. [44]. In this study, GLT has an overall lower climate impact regarding the manufacturing process than steel, although different end-of-life scenarios significantly affect the total assessment. For example, glulam had a lower GWP in the incineration scenario even with emission timing and biogenic CO_2 treatment disregarded. Moreover, glulam had a significantly lower GWP than steel if the GLT ended up in a landfill as a carbon sink instead of incineration.

2.2.4 Impact of concrete

The cement industry accounts for approximately 7% of the total global anthropogenic emissions of CO_2 and even more as a finished product of concrete [45]. There is close to a 1:1-ratio between one tonne of cement production to CO_2-equivalents, which includes the energy in the calcination process, which is the thermal treating process to remove CO_2 from limestone [46]. In 2020, the global intensity of thermal energy used to produce clinker, the main ingredient in cement, is close to 1 MWh/t [46]. In a finished unreinforced concrete mix, the total required energy equals approximately 0,4 MWh/t [47]. The cement industry accounts for 5 % of the global energy consumption [48], excluding reinforcing steel bars.

A problem for the cement industry is environmental impacts from their high-water consumption and generation of wastewater, directly or indirectly, in the manufacturing process. According to Ref. [49], the total water consumption is on averagely 0,2 m^3/m^3 concrete, which equals approximately 0,1 m^3/t.

Another comparative LCA [50] looked into laminated timber and reinforced concrete. In this Canadian case study, 10 out of 11 impact assessment categories in a cradle-to-gate perspective favored GLT. In the worst case, a concrete framed building had a 71 % higher GWP impact than a timber design. Additionally, concrete surpassed timber by 70 % in GHG emissions, including carbon storage within the wood.

2.2.5 Section summary

The quantifications found in the literature are in Figure 2.2. However, it is also crucial to consider other categories and impacts regarding sustainable building design to get a broader perspective, such as social, life cycle cost, and other economic indicators [50]. From a societal point of view, contributing toward the standardization of holes in timber beams could give a better choice of building material and ultimately offer a sustainable replacement. If holes in members become an alternative, then suspended ceiling designs are avoidable since the holes provide a passage for technical infrastructure directly through the beams instead, thus reducing materials.

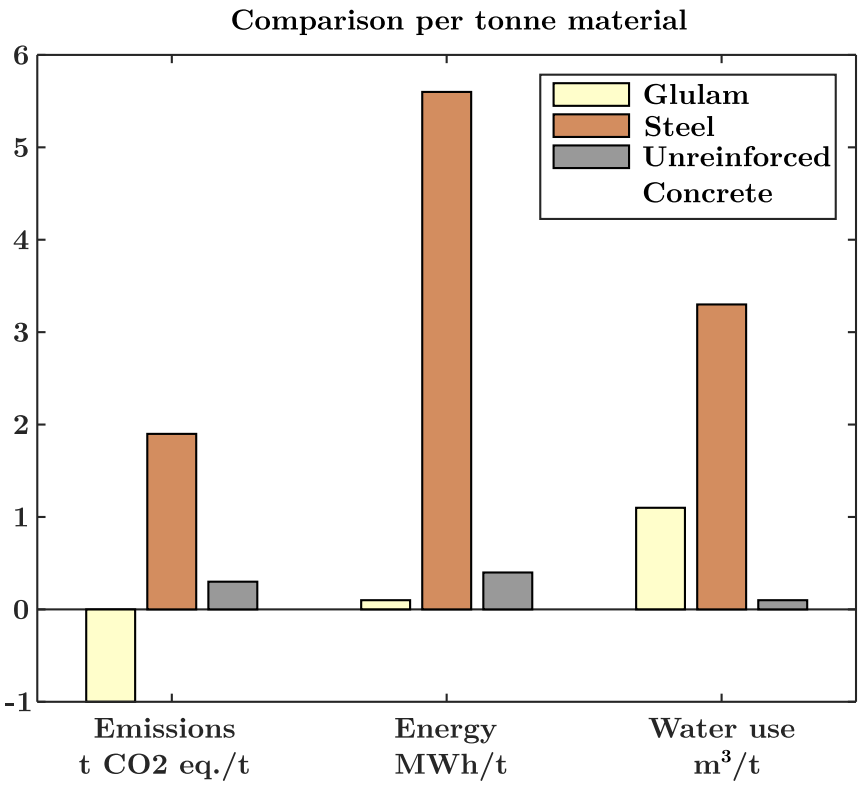

Figure 2.2: A simplified comparison of the three materials evaluated, with numbers found from literature. The bar chart values are based on a Cradle-to-Gate perspective with no particular regard to location. Additionally, some values have been converted.

3 Theoretical background

This chapter presents the necessary background knowledge of mechanical and physical timber properties and a theoretical background regarding the methods used later in this thesis to analyze the crack behavior of glued laminated timber beams with holes. Explanation of a numerical method for analyzing non-linear fracture mechanics is next in line. Finally, current reinforcement design proposals are presented, followed by a literature review summarizing experiments of glulam beams with circular holes.

3.1 Glued laminated timber

Glued laminated timber (Glulam) is a wood-based composite consisting of several layers of sawn timber lamellas bonded together with adhesives. There are two common categories of glulam, namely, homogenous and combined, and the end-letter differentiates them in their description, i.e., Gl30*h* and Gl30*c*, respectively. The number indicates the characteristic bending capacity in MPa. Homogenous elements consist of lamellae with the same strength grading (Figure 3.1a), whereas combined glulam has different strength parts (Figure 3.1b). In a combined glulam cross-section, the outer lamellae are of better quality since external zones are usually the critical area subjected to the highest concentrations of tension and compression stress under normal circumstances. According to EN 14080 [51], each outer lamellae must be at least 17 % of the beam height. For tall beams, it may be necessary with two layers at the bottom and top to reach this requirement [52].

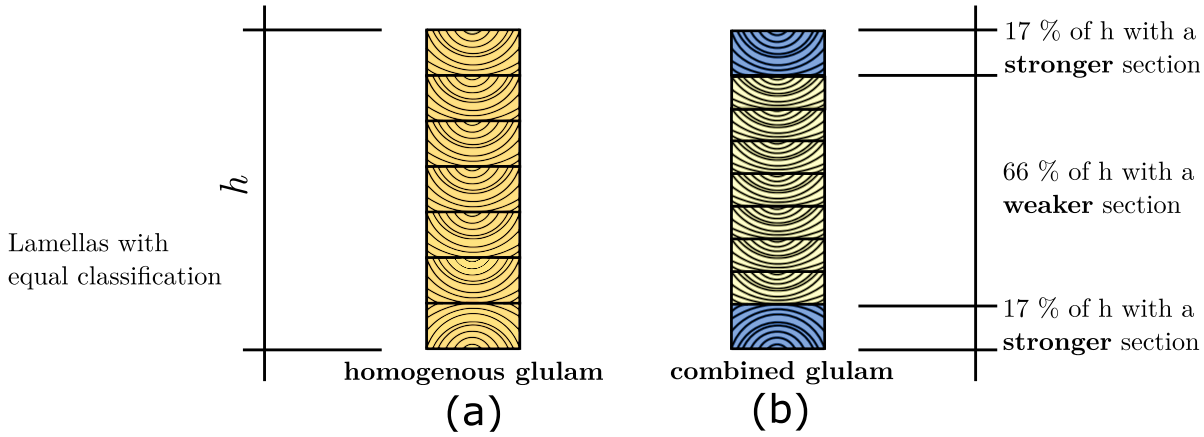

Figure 3.1: (a) Illustration of a homogenous and (b) a combined glulam element.

An equally graded homogenous element has stronger tensile and compression capacity parallel with the grain, contrary to a combined glulam element [51]; however, these are considered equal perpendicular to grain load situations.

Finger-joint is a conventional concept used in both short and long glulam elements. Therefore, it is most accurate to consider the quality of the glue-bond between layers of glulam, particularly finger joints, under bending circumstances [52]. For this present work, the glulam beams contain the adhesive called Emulsion Polymer Isocyanate (EPI), which is a two-component glue with a short curing time and has a strong bond with resistance and flexibility in regards to humidity and temperature conditions [53, 54]. EPI is applied between each lamella to connect the finger joints in the middle section. In contrast, the outer lamellae finger-joints use Phenol Resorcinol Formaldehyde adhesive (PRF) for bonding.

3.2 Mechanical properties of timber

Timber is an anisotropic material with elastic behavior, entering a plastic state during some loading circumstances. Additionally, it is viscoelastic because it is prone to creep [55]. Timber displays different behavior when subjected to substantial loading by either compression (plastic) or tension stresses (semi-brittle), as shown in Figure 3.2(a); however, linear-elastic behavior with a brittle failure is then often assumed for the practical design of timber structures. However, a non-linear approach [56] has shown to give more precise results of the ultimate load capacity.

Timber strength, stiffness, and dimensions fluctuate depending on moisture content and tree species, and it also depends on the stress direction relative to the grain. The terminology of timbers' three directions is commonly referred to as; longitudinal (L), radial (R), and tangential (T) (illustrated in Figure 3.2(b)). Additionally, parallel to grain refers to load subjected in the L-direction and perpendicular to the grain for R- and T-direction. The strength and stiffness in the R-direction are usually slightly stronger than in the T-direction [57].

The anisotropy of wood complicates calculations significantly. Therefore, timber is often considered orthotropic instead of anisotropic. This simplification reduces complexity and thereby the number of unknown engineering constants from 21 to 9. Anisotropy refers to the unique and unidentical effects, such as [58]; variation in growth rings, knots, curvature, and shrinkage. These distinctive effects are disregarded when considering orthotropy. For practical engineering design, further reducing engineering constants can be done by assuming transversal isotropy [58], which means differences in the R- and T-directions are neglected, only considering the material properties of a single perpendicular direction.

Since timber properties are dependent on a wide range of conditions, obtaining reliable data can be extensive because of the stochastic variance in results [56]. Therefore, characteristic strength values provide a safe structural design based on large-scale experiments' 5th-percentile normal distribution.

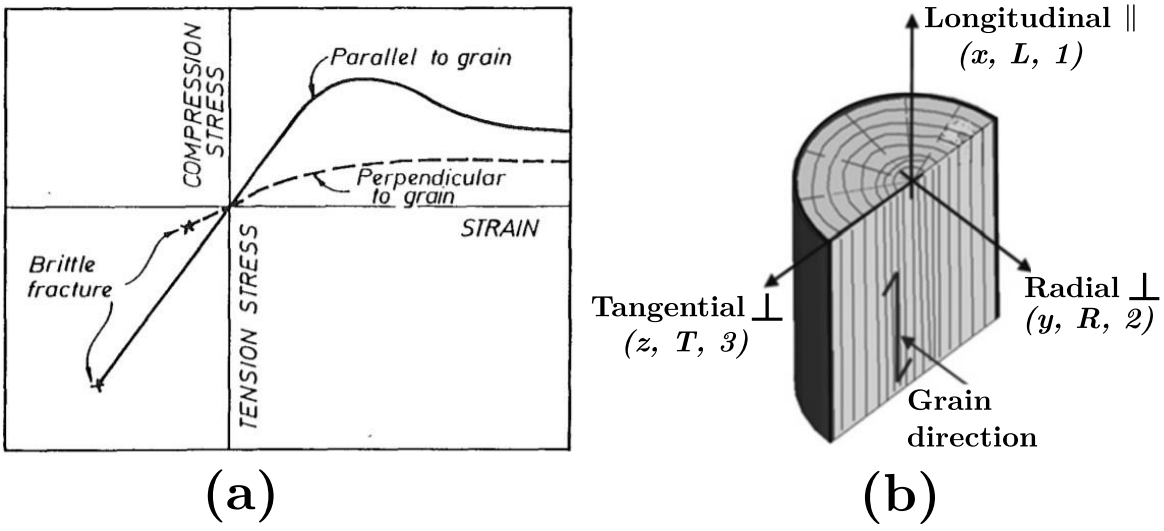

Figure 3.2: (a) Illustrates the constitutive response of timber and the relation between tensile and compressive behavior of wood, both parallel and perpendicular to the grain [59]. The capacity is much lower in the perpendicular directions. Compression forces react more ductile, while tension creates a more brittle failure. Figure (b) illustrates the global and local orientation in a 3D cross-section of a wood stem, adapted from [60].

3.2.1 Orthotropic linear-elasticity

Equations (3.1) to (3.6) describe Hooke's law's generalized constitutive relation of a three-dimensional linear-elastic orthotropic material :

$$\{\varepsilon\} = [C]\{\sigma\} \tag{3.1}$$

Where $[C]$ is the compliance matrix. Further expanded to the following matrix system:

$$\begin{Bmatrix} \varepsilon_{11} \\ \varepsilon_{22} \\ \varepsilon_{33} \\ 2\varepsilon_{23} \\ 2\varepsilon_{13} \\ 2\varepsilon_{12} \end{Bmatrix} = \begin{bmatrix} \frac{1}{E_{11}} & \frac{-v_{21}}{E_{22}} & \frac{-v_{31}}{E_{33}} & 0 & 0 & 0 \\ \frac{-v_{12}}{E_{11}} & \frac{1}{E_{22}} & \frac{-v_{32}}{E_{33}} & 0 & 0 & 0 \\ \frac{-v_{13}}{E_{11}} & \frac{-v_{23}}{E_{22}} & \frac{1}{E_{33}} & 0 & 0 & 0 \\ 0 & 0 & 0 & \frac{1}{G_{23}} & 0 & 0 \\ 0 & 0 & 0 & 0 & \frac{1}{G_{13}} & 0 \\ 0 & 0 & 0 & 0 & 0 & \frac{1}{G_{12}} \end{bmatrix} \begin{Bmatrix} \sigma_{11} \\ \sigma_{22} \\ \sigma_{33} \\ \tau_{23} \\ \tau_{13} \\ \tau_{12} \end{Bmatrix} \tag{3.2}$$

where ε_{ij} is the strain tensor $(i, j = 1,2,3,\ i \neq j)$, E_{ii} is Young's moduli of elasticity (MOE), G_{ij} is the shear moduli, ν_{ij} is Poisson's ratio, stress component tensor σ_{ii} and lastly, shear stress tensor τ_{ij}. The (1,2,3)-coordinate system corresponds to the local timber coordinate system (L, T, R). The relation between Poison's ratio and Young's moduli is given in eq. (3.3), due to symmetry in the compliance matrix $[C]$:

$$v_{ij} = \frac{E_{ii}}{E_{jj}} v_{ji}, \quad i, j = 1,2,3, i \neq j \tag{3.3}$$

Equation (3.1) can be rewritten to (3.4), with $[D]$ being the stiffness matrix:

$$\{\sigma\} = [D]\{\varepsilon\} \tag{3.4}$$

And finally, the stiffness matrix of an orthotropic material in a 3D space with nine independent constants:

$$[D] = \begin{bmatrix} \frac{E_{11}(1-v_{23}v_{32})}{\Psi} & \frac{E_{22}(v_{12}+v_{32}v_{13})}{\Psi} & \frac{E_{33}(v_{13}+v_{12}v_{23})}{\Psi} & 0 & 0 & 0 \\ & \frac{E_{22}(1-v_{13}v_{31})}{\Psi} & \frac{E_{33}(v_{23}+v_{21}v_{13})}{\Psi} & 0 & 0 & 0 \\ & & \frac{E_{33}(1-v_{12}v_{21})}{\Psi} & 0 & 0 & 0 \\ & & & G_{23} & 0 & 0 \\ & Symmetry & & & G_{13} & 0 \\ & & & & & G_{12} \end{bmatrix} \tag{3.5}$$

with

$$\Psi = 1 - v_{12}v_{23} - v_{23}v_{32} - v_{31}v_{13} - 2v_{21}v_{32}v_{13} \tag{3.6}$$

A typical transversal isotropic assumption in eq. (3.7)-(3.8) shows the further reduction of unknown engineering constants. The following relation between moduli of elasticity and shear is assumed [61]:

$$E_{transv} = E_y = E_z = \frac{E_x}{30} \tag{3.7}$$

$$\frac{E_x}{G_{xy}} = \frac{E_x}{G_{zx}} = 16, \quad \frac{G_{xy}}{G_{yz}} = 10 \tag{3.8}$$

3.3 Physical properties

Timber is a hygroscopic material, which means it will absorb moisture from the surrounding air, and conversely, it can release vapor depending on the relative humidity in the atmosphere [62]. As a result, timber continuously shrinks and swells, influencing the dimensions and strength characteristics. The mass of timber is also affected relative to the moisture content, which means that the density is inconsistent. The effect of end-grain moist exposure in beams with holes can be significant [12], and approximately half of the damages recorded in large-span GLT-constructions are due to moisture-induced stress. A proposal for counter-measure [12] is to reduce the initial moisture difference within an element before installing it. External reinforcement installed on the gross-section of a beam can also reduce critical moisture variations [12]. Figure 3.3 illustrates a possible moisture cycle from logging to operation.

In addition to moisture, the temperature is also a contributing factor to physical and mechanical parameters. The combination of; variance in moisture content, temperature, and unidentical anisotropic anatomy makes it difficult to accurately mimic realistic situations in analytical and numerical calculations.

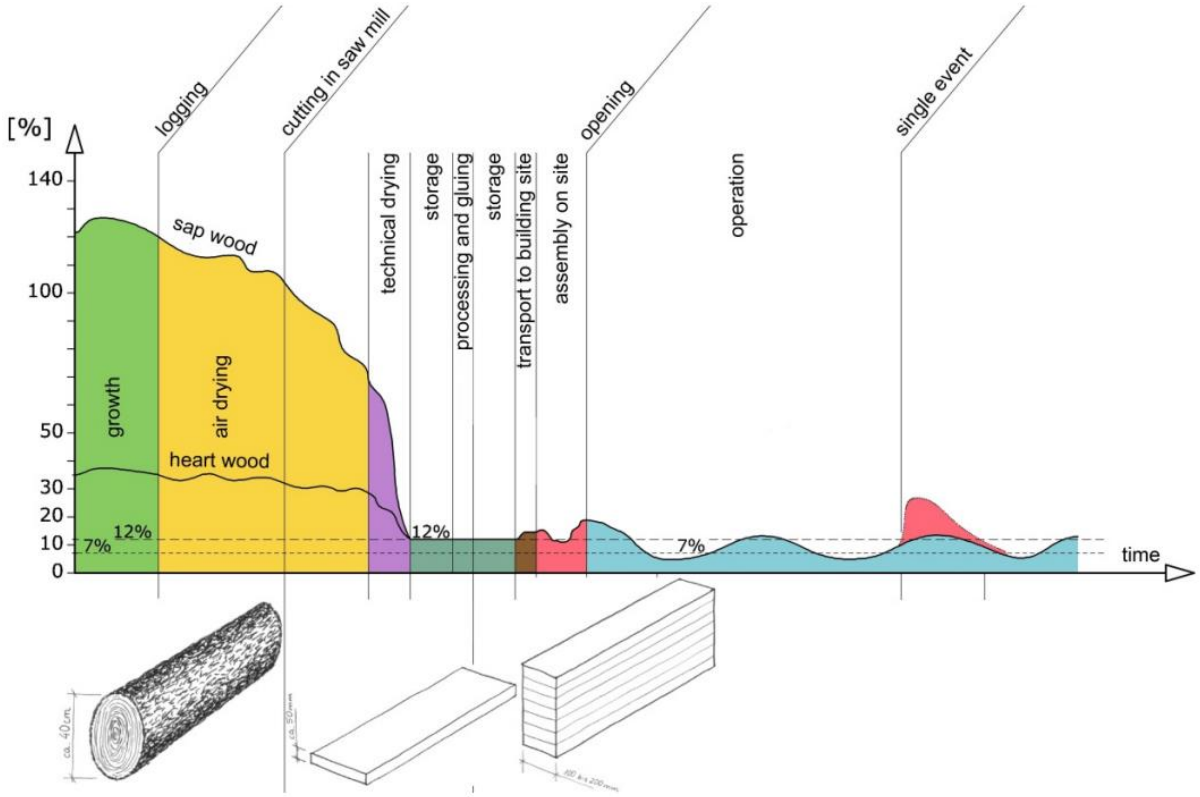

Figure 3.3: Illustration of a possible moisture cycle, from wood stem to installed timber element [3].

3.3.1 Moisture content

The moisture content of $\omega = 12\ \%$, is standardized for experimental testing of timber [65] and is considered the optimal condition. ω can also be calculated in general as expressed in equation (3.9) [56], if the mass of the specimen in dry and moisture condition is known:

$$\omega = \frac{m_{wet} - m_{dry}}{m_{dry}} 100\ [\%] \tag{3.9}$$

And the mass of the water can be derived by the following:

$$m_{\omega} = m_{wet} - m_{dry} \tag{3.10}$$

Determination of the moisture content in a laboratory environment is described in EN 13183-1 [66] with the oven-dry method and EN 13183-2 [67] when using electronic equipment.

3.3.2 Density

Since timber density ρ, volume V, and mass m, vary relative to the moisture content, eq. (3.11) denotes density at any given moisture content:

$$\rho_{\omega} = \frac{m_{\omega}}{V_{\omega}} \tag{3.11}$$

3.4 Stress distribution and crack development in the vicinity of circular holes

Cavities negatively influence the strength of a structural beam or joist, and it may alter the failure mode due to stress concentrations, causing premature failure. Since wood is fragile regarding tension stress, predominantly perpendicular to the grain, as shown in Figure 3.2(a), it is necessary to analyze the contributing factors to stress occurrences.

Aicher & Höfflin [68] show that hole dimension (h_d) and placement affect the tensile and compressive stress distribution in the hole vicinity. They state that the tension stress perpendicular to grain peaks in the bending-compression zone (see illustration in Figure 3.4a). Similar results are found in Ref. [5], of laminated veneer-lumber (LVL) by Ardalany, where the maximum tensile stress perpendicular to the grain, $\sigma_{t,90}$, was achieved at an $\varphi = 45°$ inclination from the neutral axis. Vertical hole eccentricity changes the inclination of stress relative to the neutral axis [69]. It is further proclaimed in Ref. [68] that the first crack occurrence is dependent on the horizontal location of the hole, and results show initial cracking at the following intervals: $\{40° \leq \varphi \leq 60°\}$ *or* $\{220° \leq \varphi \leq 240°\}$. Horizontal hole placement along the beam length is an important consideration because contributions from both shear and moment will be present near a support. Subsequently, if a hole is placed near the middle of a beam, only contributions from bending can be regarded, in which case the stress distributions are changed considerably (Figure 3.4b), where cracking will occur at approximately $\varphi \approx 60°$ and $300°$ instead [70, 71].

Cracking will happen if the hole is large enough to alter the failure mode of the beam. Once the cracking has begun, it works as a bridge for concentrated tension stress [5], stretching the wood apart perpendicular to the grain. Initial cracking in previous research occurred in the center of the beams' cross-sectional width in all 68 tested glulam specimens.

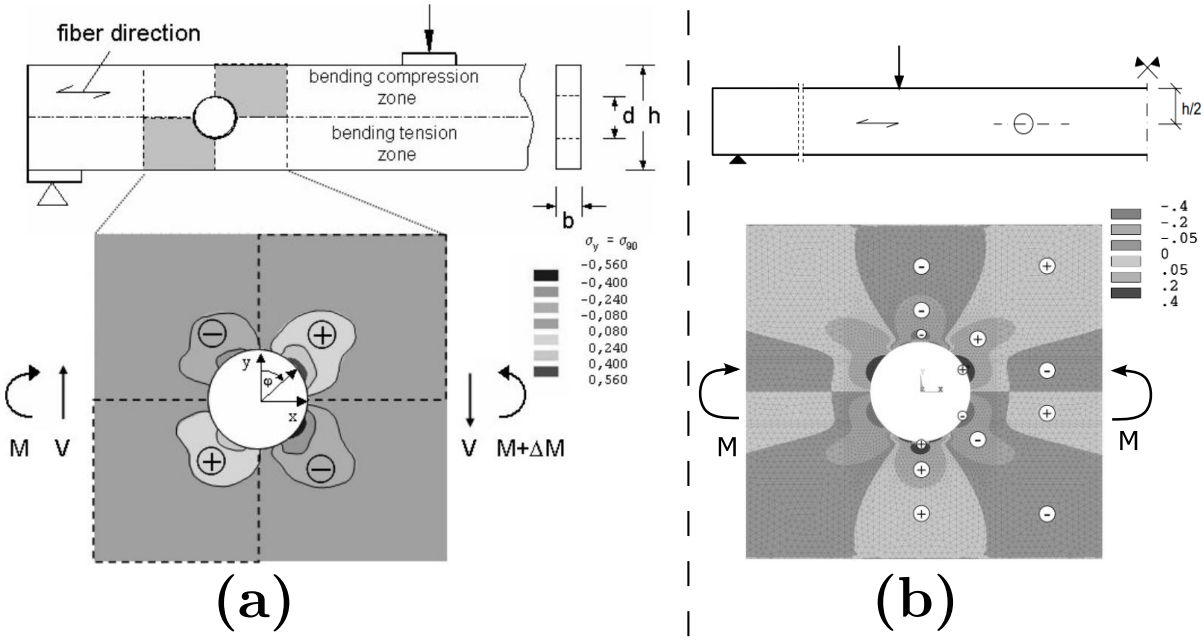

Figure 3.4: (a) Stress distribution in the vicinity of a typical non-reinforced hole in glulam beams subjected to combined shear and bending forces [68], and (b) shows the stress distribution when only moment contributions are present [71]. (+) for tension, (-) compression.

After the initial cracking occurs, further increasing the force will cause the evolution of the crack until the total width is cracked, as seen in Figure 3.5(b, c), and appears on the side of the beam. Finally, cracking continues to develop gradually along the horizontal beam axis (see Figure 3.5(a, d)) until the ultimate failure of the beam is caused by tension stress [72]. The required stress for causing failure is far lower than in an intact beam because of the tensile stresses acting perpendicular to the grain.

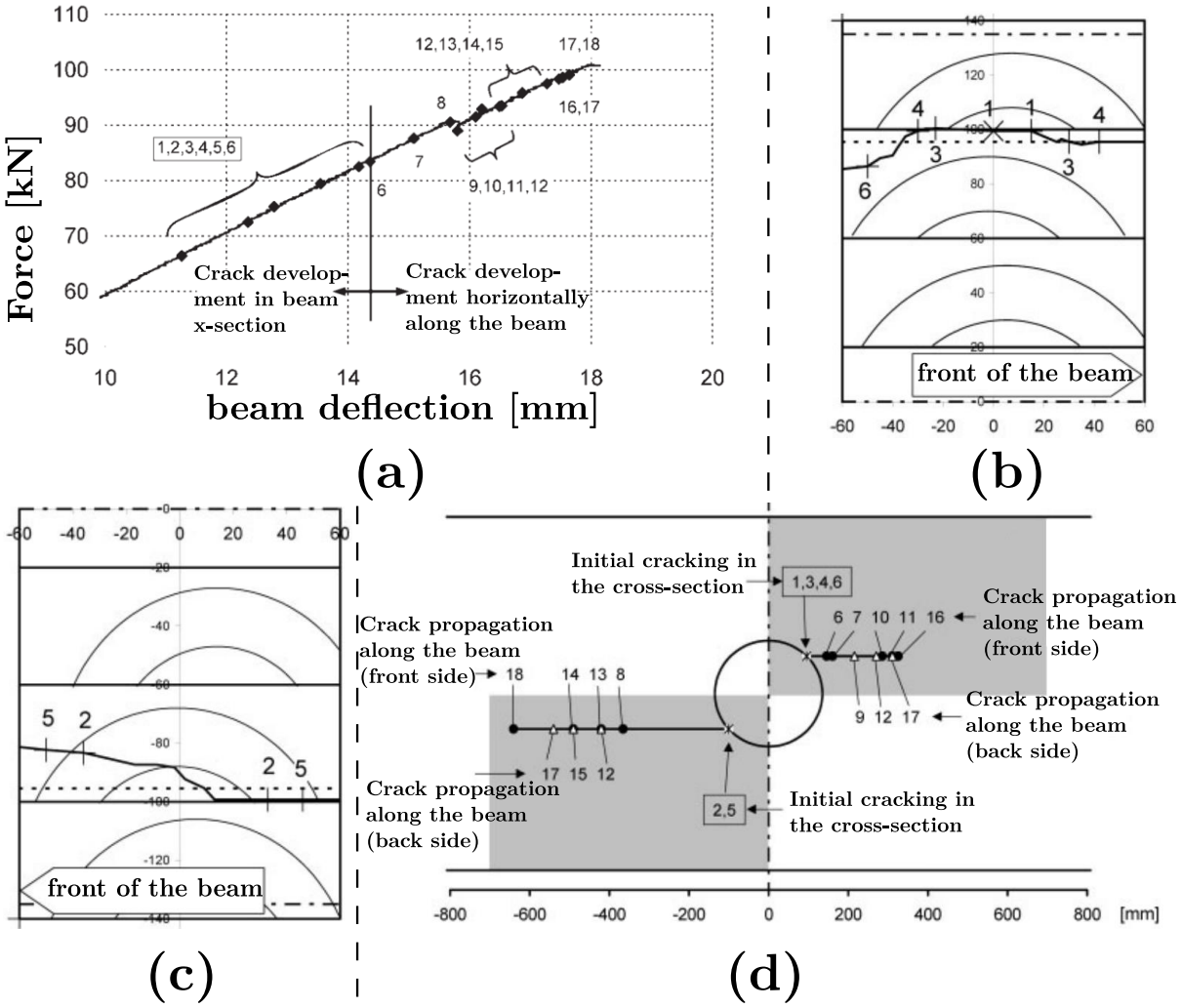

Figure 3.5: (a-d) is translated from German Ref. [72]. (a) Crack propagation relative to force and beam deflection, (b) propagation in the cross-section of the “upper-right”-part of the hole, (c) propagation in the “lower-left”-part of the hole, and finally (d): Crack propagation horizontally along the beam axis.

The stress type to consider is tension and shear perpendicular to the grain near the hole, which is emphasized in a combined glulam beam cross-section since holes typically are placed in the middle of the elevation, which is the weakest part of this type of beam.

3.5 Fracture mechanics

In a conventional structural design situation, strength is the decisive material property. As stated by Anderson [73], there are two variables to consider in a traditional design: (i) The amount of applied stress and (ii) the yield or tensile strength. However, when specific areas of the structure are under stress concentrators, then fracture mechanics (FM) apply [5], where the two critical variables are replaced by three: (i) Applied strength, (ii) crack size, and (iii) fracture toughness [73]. Figure 3.6 presents a graphical comparison of the two design principles.

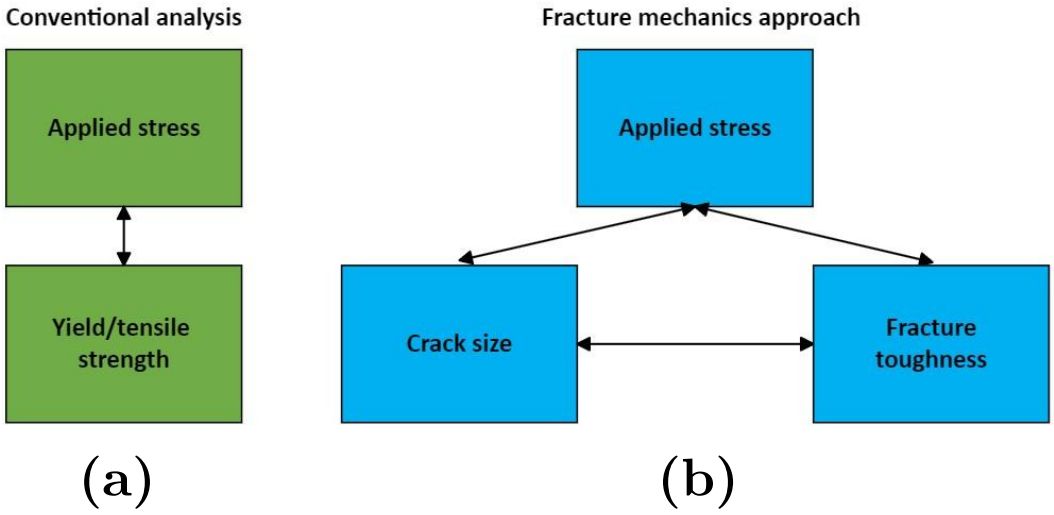

Figure 3.6: Adapted from [73]. (a) shows a conventional structural design analysis, and (b) a structural design analysis using the FM approach.

A fracture mechanics (FM) approach is necessary to provide a safe analysis of a loaded timber beam with large holes because of the stress concentrations and crack tendencies described in chapter 3.4. The crack evolution in a loaded beam can occur in three ways and combinations (Figure 3.7a); opening by tensile action (mode I), shearing by pulling in different directions along the beam (mode II), or by tearing outwards of the beam axis (mode III). The local coordinate system $(n, s, t = I, II, III)$ also refers to each of these modes. Two of these mechanics are present in the analysis performed further in this thesis: Mode I and II [5].

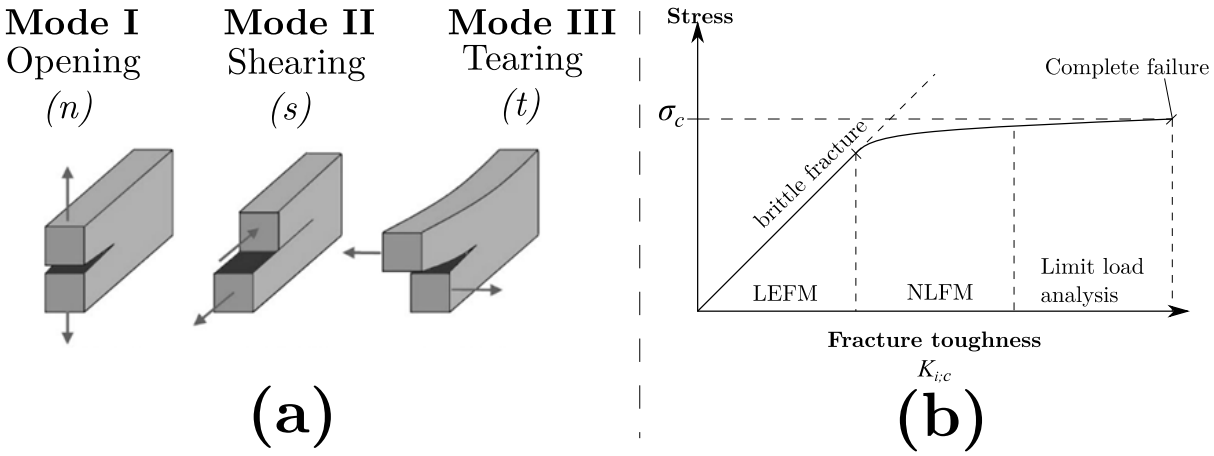

Figure 3.7: (a) The three possible fracture modes; where mode I is due to tensile stress normal to the crack plane, mode II is shearing in the crack plane by parallel sliding, and mode III is tearing out of the beam axis, also called the second shear plane. Illustration adapted from [74]. (b) The graph shows the limitations of LEFM in regards to non-brittle materials with high toughness, adapted from [73].

Various analytical and numerical methods exist for FM analyses, commonly split into two main categories: non-linear fracture mechanics (NLFM) and linear elastic fracture mechanics (LEFM).

In 1921, Griffith [75] applied the minimum potential energy theorem to the crack mechanism in materials. He stated that the critical condition for initial cracking or propagation of a crack happens when the system is in equilibrium and when the system's total energy is kept constant or reduced. Furthermore, when the energy starts to decline, so will the crack propagation. Griffith's research applies to brittle materials with isotropic assumptions.

Since then, the subsequent development of LEFM theory has enabled problem-solving of various materials, using analytical methods in some cases and numerically by utilizing the finite element method (FEM). However, there are some limitations to LEFM methods, such as having a prerequisite requirement of knowing the initial crack opening [5].

NLFM is relevant when both or either is present [61]: (i) General nonlinear material stress and strain relation outside of a fracture zone, or (ii) when a specific region prone to fracture has nonlinear stress and deformation relation. With advanced computer science and broader availability, NLFM has become a relevant tool for analyzing structural cracks; because of the software's ability to efficiently apply known theoretical concepts.

As already mentioned, fracture modes I and II are typical to consider for a glulam beam with holes. Therefore, Wu's mixed-mode (I-II) fracture-criterion (3.12) [76] is further used in this thesis, where *m* and *n* represent 1 and 2 for timber, respectively.

$$\left(\frac{G_I}{G_{Ic}}\right)^m + \left(\frac{G_{II}}{G_{IIc}}\right)^n = 1 \tag{3.12}$$

With G_I and G_{II} being the fracture energy, G_{Ic} and G_{IIc} the critical energy release rate in the opening and shearing mode, respectively.

3.5.1 Cohesive zones

Although the assumed linear-elastic brittle behavior of tension perpendicular to the grain, timber and wood composites require a non-linear fracture model to study the post-failure behavior successfully. Analyzing stiffness degradation after crack initiation can be achieved using the cohesive fracture zone approach. Dugdale [77] and Barenblatt [78] studied cohesive bonds near crack tips, hence the name cohesive zone elements (also referred to as «fictitious crack model»). Dugdale applied his hypothesis to sheet metal slits and Barenblatt to brittle solids. Later, further research was done in the area by Hillerborg [79], and this work applied the Dugdale-Barenblatt model to concrete. Gustafsson [80] finally applied this concept to wood. The cohesive zone method assumes a plastic zone ahead of the crack tip. Hillerborg found a constitutive relation between stress-deformation of tension in the fracture zone, describing the stress softening part behind the crack tip of the fracture area, and this cohesive behavior is a material-dependent property [73].

The cohesive zone method is described in the literature as reasonably applicable to timber because of its quasi-brittle properties . Non-fractured parts of a uniaxially loaded timber beam with holes have elastic behavior, while fracture zones will experience nonlinear softening. The nonlinearity is due to the damage increase while the required stress decelerates [56], as shown in Figure 3.8(b). Moreover, this behavior can sometimes refer to micro-cracking occurrences [10] (Figure 3.9). The fracture process in wood is complex because of several mechanisms that contribute to damage simultaneously.

Consequently, there is no generalized law that can describe the general post-failure behavior, but exponential traction-separation behavior has shown to be applicable for approaching experimental results [81].

The commercial finite element software ABAQUS does not recognize where a crack should occur or how long it should propagate in an elastic FE-model. However, cohesive properties can be defined by either creating a cohesive zone or by characterizing surfaces to behave under these cohesive laws during post-failure. Therefore, a finite element model in ABAQUS is used further in this present work, with a surface-based cohesive zone model (SCZM). The placement of this layer is with regards to the previously discussed theory (Chapter 3.4), and the inclination from the hole center is $\varphi = 45° \ (+180°)$. In situations where crack locations are unknown, it is possible to run an analysis to identify the most prominent stress occurrences. However, the propagation may be challenging to predict or incoherent for some materials.

Three different parameters for each present fracture mode are necessary to perform a cohesive FM analysis in Abaqus, which can be defined by:

(i) Either by; the energy released during fracture G_F, defined by the area outlined of the traction-separation curve (the energy method); or the surface separation point δ_e (the effective separation method),
(ii) the initial slope of the first elastic line, and
(iii) the evolution damage line, which can either be defined as linear or exponential, in which case an evolution-exponent coefficient α has to be specified when using the effective displacement method.

Wang et al. [82] describe exponential softening in ABAQUS as problematic in some cases since the softening rate is equal for both tension and compression. In addition, a recent paper found it quite complex to obtain the correct exponential coefficient for curvature as done by Ostapska et al. in [81] by model-calibrating based on wedge-splitting experiments. Therefore, a bilinear (Figure 3.8a) simplification may sometimes be preferred, as it will lead to a better convergency rate [5], even though it is less accurate, as found in Ref. [56].

The fracture energy G_F can be expressed by the integral in equation (3.13):

$$G_F = \int_0^{\delta_e} T(\delta)\, d\delta \tag{3.13}$$

G_F is the area underneath the traction-separation curve (Figure 3.8), which can be found experimentally, e.g., by the wedge splitting test [83]. The figure represents an arbitrary relation between traction and the separation of either mode I (opening) or II (shearing). Damage initiation criteria occur at δ_c which is when the tensile force exceeds the cohesive bonding strength of the material, which will cause cracking to start (eq. (3.15)). Conversely, if the tension in the fracture zone does not reach the T_{max} limit, then the cohesive stiffness is kept constant [5]. δ_e represents the point when the fracture process is complete. Figure 3.9 shows a two-dimensional sketch of cohesive layers, specifically where cracking will happen when a timber beam with a hole is subjected to combined moment and shear, as described in chapter 3.4. Crack tip opening begins at the maximum stress point, T_{max}, which leads to fiber-bridging due to the tensile stress perpendicular to grain. A micro-cracking

region is ahead of the crack, meanwhile the stress behind it are decreasing . Complete separation is when the crack lips are traction-free [81].

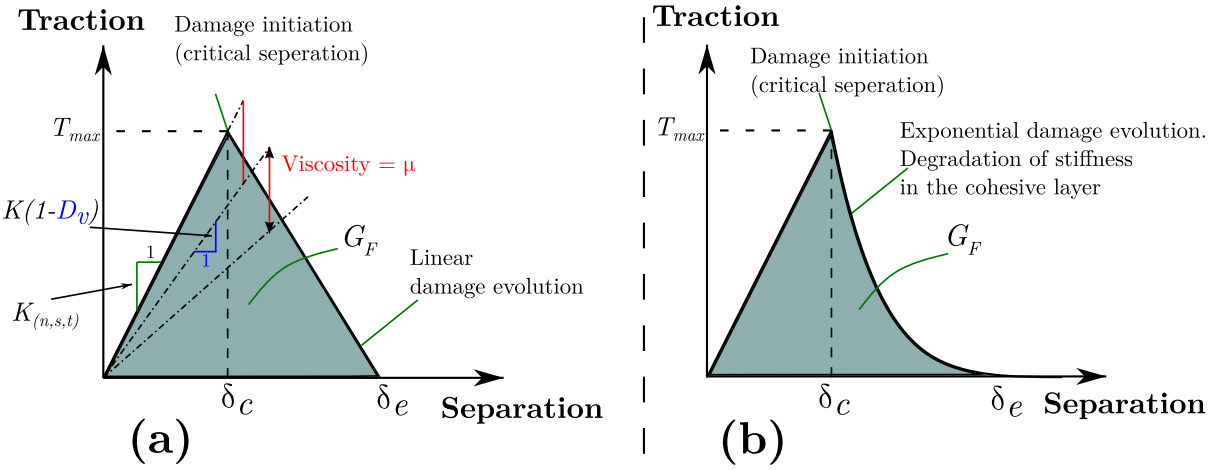

Figure 3.8: A sketch of a traction-separation curve with (a) linear and (b) exponential softening. Damage initiation occurs at the peak traction. Damage evolution means that the stiffness is degraded gradually within the cohesive layer. Fracture energy is the area underneath the curve. K_i is the linear slope before damage initiation in the specific fracture or mixed-mode situation.

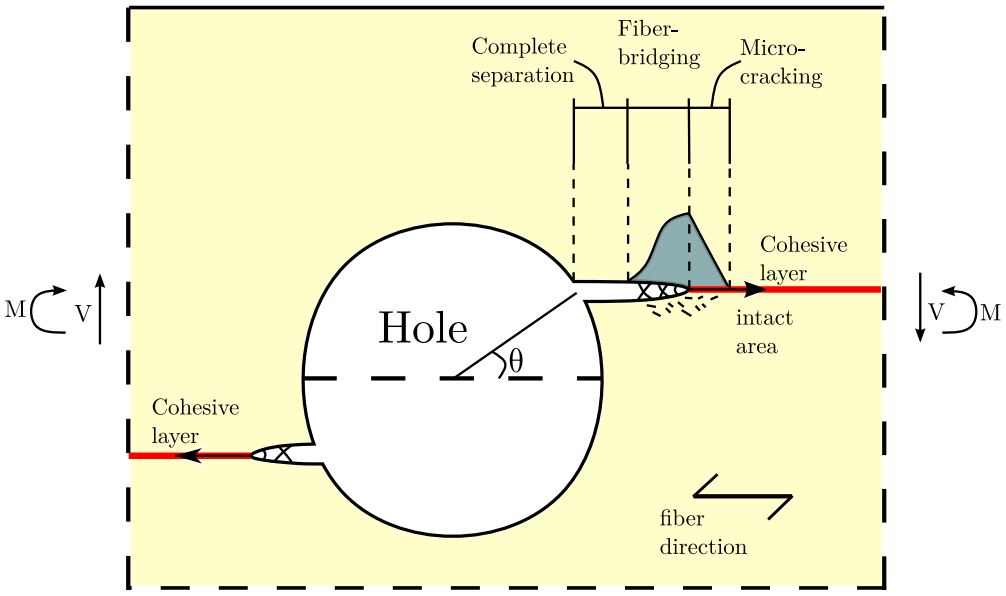

Figure 3.9: A sketch of the crack propagation mechanics with a physical interpretation of the cohesive layer for a beam with a single circular hole without reinforcement, subjected to bending and shear.

It may be necessary to combine the contributions to a single plane for mixed-mode situations. An effective displacement can be determined in a three-dimensional space, accounting for each mode [84], such that:

$$\delta_m = \sqrt{\delta_n^{\,2} + \delta_s^{\,2} + \delta_t^{\,2}} \tag{3.14}$$

Critical separation starts once the criteria in equation (3.15) are met [84]:

$$Max\left\{\frac{T_n}{T_n^{max}}, \frac{T_s}{T_s^{max}}, \frac{T_t}{T_t^{max}}\right\} = 1 \tag{3.15}$$

Additionally, a viscosity coefficient μ is required (illustrated in Figure 3.8a), which is defined by the height of the slope. This is a measure of how many increments Abaqus uses to calculate the tangential stiffness matrix. A lower viscosity coefficient has previously proved to increase the accuracy of an FEA [5]; however, at a higher computational cost. The viscous stiffness degradation variable, D_v, of the curve in Figure 3.8 is defined by Abaqus as [85]:

$$\frac{\partial}{\partial t} D_v = \frac{1}{\mu}(D - D_v) \tag{3.16}$$

Where D is the damage parameter, with a value ranging between 0 to 1, where 0 is undamaged, and 1 is completely damaged (separated). D are calculated by Abaqus as shown in equation (3.17 a) for linear softening and (3.17 b) for exponential softening when using the energy method.

$$D = \frac{\delta_m^e(\delta_m^{max} - \delta_m^c)}{\delta_m^{max}(\delta_m^e - \delta_m^c)} \tag{3.17a}$$

$$D = \int_{\delta_m^c}^{\delta_m^e} \frac{T_m d\delta}{G_F - G_c} \tag{3.17b}$$

The present work uses the energy method with a bilinear traction-separation behavior assumption.

3.6 Reinforcement design for glulam beams with holes

Removing an area from the gross-section of a beam diminishes the strength, although the significance depends on the removed area's placement and size. On the other hand, reinforcing the fracture areas can improve the resistance considerably against premature failure and ideally alter the failure condition to bending or shear. Reinforcement is usually categorized either as internal or external reinforcement. Internal reinforcement is not visible, which could have an aesthetic benefit when the construction is visible. The second may be preferred in practical situations when internal reinforcement is more challenging to install, such as when there is a need to drill holes on-site or in confined spaces after mounting a beam. Previous research introduces several methods for reinforcing timber beams with holes and notches by using:

a) Glued-on plane reinforcement (LVL, plywood, OSB, panels, etc.) [86, 87]
b) Self-tapping screws, vertically and with an angle [88, 89]
c) Predrilled and glued-in steel bars and rods, vertically and with an angle [86, 88, 90]
d) Internal vertically placed LVL reinforcement between glulam layers [91, 92]

The reinforcement methods mentioned above are visualized in Figure 3.10.

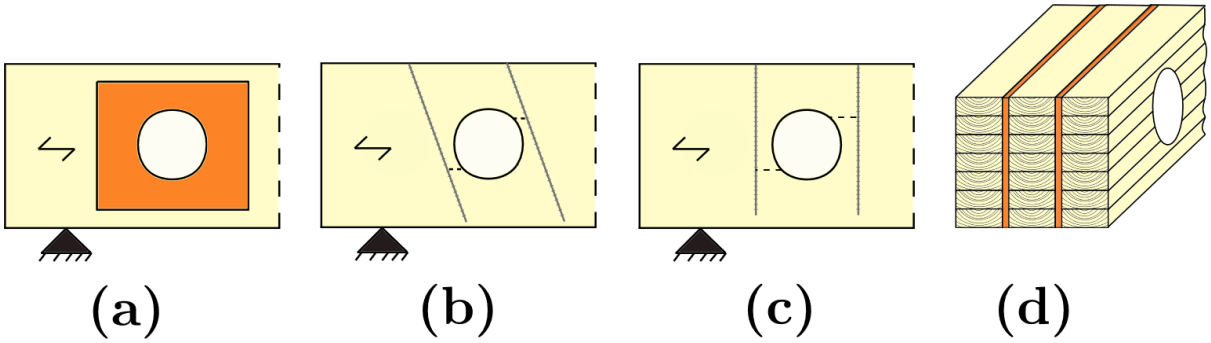

Figure 3.10: (a) glued-on-plane reinforcement, (b-c) fully threaded self-drilling screws or glued-in steel rods vertically and with an inclination. Notice that cracks can still occur between the hole and screws. (d) internal, vertical glued-on reinforcement (e.g., LVL) between layers of glulam.

3.6.1 Glued-on reinforcement criteria according to a draft of the upcoming Eurocode 5

The current Eurocode 5 does not include beam members with holes nor reinforcement; however, a work group at CEN is currently developing a new separate chapter regarding the reinforcement of timber constructions and a section for members with holes [93].
This subchapter presents the current state-of-the-art glued-on reinforcement hole designs, which are currently under development for the new Eurocode 5 version [93]. Design tensile strength perpendicular to the grain must be greater than the relative total tensile stress, as expressed by equation (3.18).

$$\frac{F_{t,90,Ed}}{F_{t,90,Rd}} \leq 1{,}0 \tag{3.18}$$

The total tensile stresses perpendicular to the grain are summarized as follows:

$$F_{t,90,Ed} = F_{t,V,Ed} + F_{t,M,Ed} \tag{3.19}$$

The two following empirical equations can approximate shear and moment contributions:

$$F_{t,V,Ed} = \frac{V_d \cdot h_d}{4h} \cdot \left[3 - \frac{h_d^2}{h^2}\right] \tag{3.20}$$

$$F_{t,M,Ed} = 0{,}09 \cdot \frac{M_d}{h} \cdot \left(\frac{h_d}{h}\right)^2 \tag{3.21}$$

Where h is the beam height, and h_d is the hole diameter, which has limitations according to Table 3.1. Note that the above equations are currently under further evaluation by the committee because they do not account for vertical eccentricity and all tensile contributions from bending [93].

Calculation procedure of perpendicular tensile design resistance $F_{t,90,Rd}$ depends on the reinforcement type, and the current method proposal for glued-on reinforcement, such as LVL, is calculated according to equation (3.22). See Ref. [93] for calculation methods of other reinforcement types.

$$F_{t,90,Rd} = n_r \cdot min \begin{cases} f_{b2,d} \cdot l_{ad} \cdot b_r \\ \dfrac{f_{t,d}}{k_k} \cdot b_r \cdot t_r \end{cases} \tag{3.22}$$

$$l_{ad} = h_1 + 0{,}15 \cdot h_d \tag{3.23}$$

Where:

- $\boldsymbol{n_r}$ is the number of reinforcements, which is either 1 or 2 for glued-on plane reinforcement (each side)
- $\boldsymbol{f_{b2,d}}$ is the design glue-line strength
- $\boldsymbol{l_{ad}}$ is the distance to the reinforcement carried potential crack line as seen in Figure 3.11
- $\boldsymbol{b_r}$ is the width of the plane reinforcement
- $\boldsymbol{f_{t,d}}$ is the design tensile strength of the plate
- $\boldsymbol{t_r}$ is the thickness of the plate
- $\boldsymbol{k_k}$ is a factor of $\{1;\ 1{,}5;\ 2{,}0\}$ depending on the reinforcement function and beam geometry.

Table 3.1: The limitations to horizontal placement along the beam and other geometrical boundaries for reinforced holes. The hole dimension criteria are valid for glued-on reinforcement only.

End distance to the hole	Space between holes	Distance to support from the hole	Hole dimension
$l_V \geq h$	$l_Z \geq h$ $(min.\ 300\ mm)$	$l_A \geq \frac{h}{2}$	$h_d \leq 0{,}4 \cdot h$

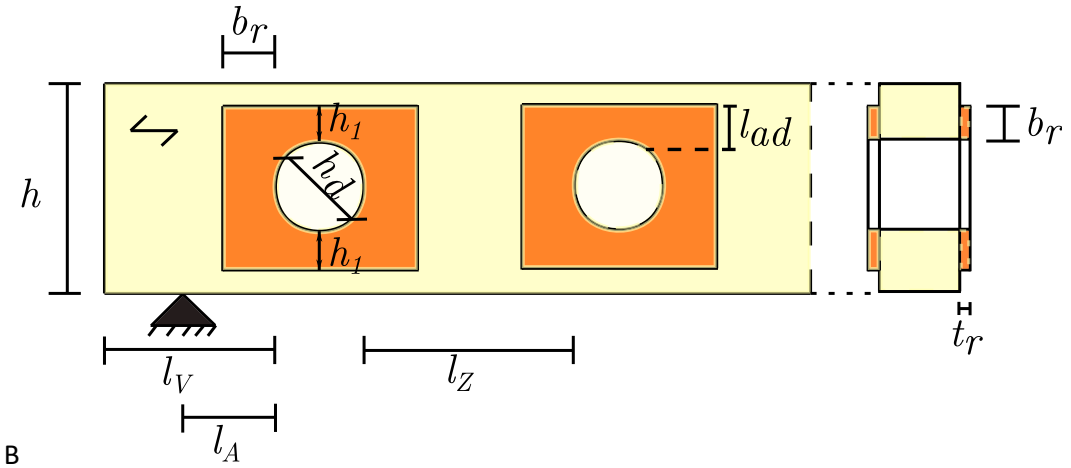

Figure 3.11: Illustration of a reference glulam beam with glued-on reinforcement with circular holes.

3.7 Digital image correlation

This optical method captures displacements over a field and allows the computing of surface strains. Utilizing a two-camera setup allows stereo-triangulation to perceive images in three dimensions, see Figure 3.12. Initially, a speckle pattern is painted onto the object within the field of interest, with a density of approximately 50 %. Then, the software uses the pattern to detect changes between the speckle points, like nodal displacement in a finite element analysis. Distance to the object and between cameras, speckle pattern quality, and size relative to the camera distance and resolution contribute to the accuracy.

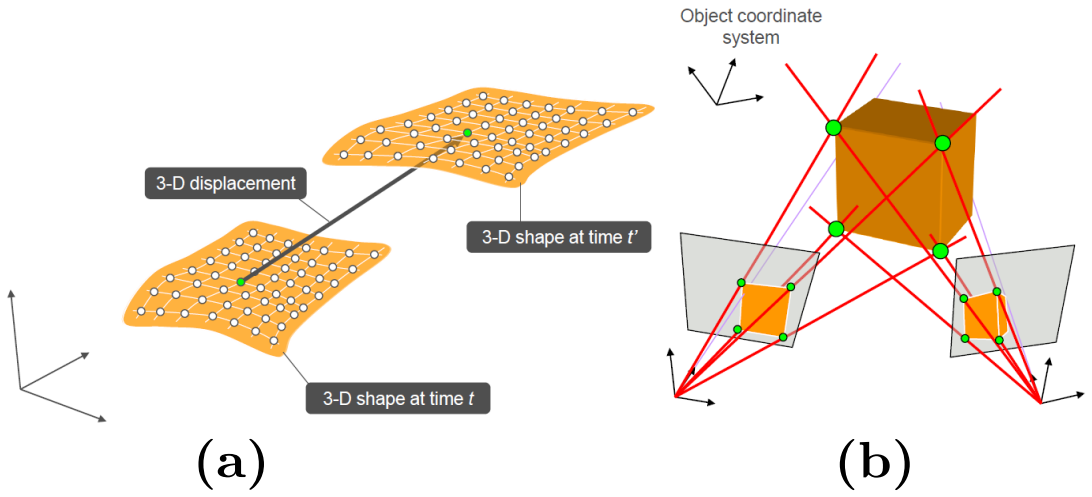

Figure 3.12: (a) Example of a 3D displacement-field, and (b) the stereo-triangulation principle [94].

In post-processing, after selecting an area of interest, a mesh is formed based on the subset size chosen, and step size is the amount of calculation done within each window. Utilizing a smaller step size will result in a more refined analysis but at the cost of computation time. Doing so also decreases grey area, which means undetected zones in post-processing analysis. The software VIC-3D automatically calculates a recommended subset size, which gives a confidence of 0,01 pixel based on an initial set noise level [95]. See eq. (3.24) for recommended relation between step, filter, and subset sizes.

$$\text{Step size} \cdot \text{Filter size} > \text{Subset size} \tag{3.24}$$

Post-processing allows for computing contour plots to detect and illustrate a chosen output variable. Position and displacement of the three dimensions are always calculated relative to the reference image, and additional variables can be selected for extraction, such as strain, velocity, curvature, and rotation from any given point [95]. The formula presented in Figure 3.13 shows the image correlation calculation procedure.

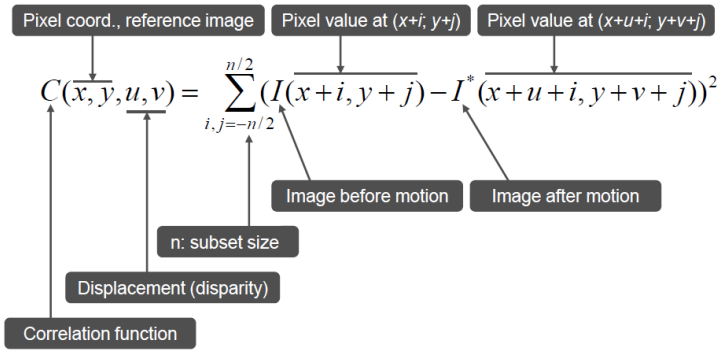

Figure 3.13: VIC-3D calculation procedure for image correlation [94].

3.7.1 Automatic crack detection and measurement (ACDM)

A novel method developed in 2020 [96, 97] uses third-party software MATLAB 2021+ to automatically detect cracks based on image correlation instrumentation's highly accurate displacement fields. The tool identifies crack occurrence based on principle tensile surface-strain areas, which allows the detection of fine cracks. ACDM discovers flaws by comparing a crack at the stabilized stage with the last analyzed image, preventing disjoint cracks. After transforming the extracted DIC data to MATLAB format, ACDM can then process the captured fields and compute the desired data, which depends on the goal of the analysis. The crack detection relies on a defined strain threshold, and it is suggested in [96] that the strain threshold should be greater than the sum of the largest elastic tensile strain and noise interval.

3.8 Literature review of glulam beam experiments with hole(s)

An experimental overview of previous glulam beam research, including circular holes, is presented in this section, both with (n= 206) and without reinforcement (n= 85). Note that experiments with more than two holes, extraordinary dimensions (above one meter tall), curved beams, and experiments with rectangular holes are excluded. Each row indicates a different beam configuration regarding the hole or dimensions. Experiments are divided into other series when a single paper presents multiple test objects with varying beam dimensions. All timber specimens are spruce glulam beams unless expressly stated otherwise. ***L*** indicates the span of the beam between the supports, ***H*** the height, and ***B*** the width. The sample size is shown in column ***n***. $\boldsymbol{L_A + h_r}$ suggests the distance from the closest support to the hole center, and further, $\boldsymbol{L_Z + h_d}$ means the distance from the center to center between the first and the second hole (if multiple holes are present). ***e/h*** is the eccentricity relative to the beam height. Table 3.2 is a reproduction of Danielssons's literature study [11], where the year 1971-2006 are covered without reinforcement.

Table 3.3 presents recent experiments of circular holes without reinforcement, covering the year 2006-2021. Finally, Table 3.4 organizes literature from recent experiments covering 2009-2021 with various reinforcement types.

Table 3.2: Experiments on glulam beams with circular holes without reinforcement. Literature from 1971 to 2006 (adapted from Danielsson [11]).

Author and year	Ref.	Series	L x H x B [mm]	n	$L_A + h_r$ [mm]	$L_Z + h_d$ [mm]	h_d/h [-]	e/h [-]
Bengtsson 1971	[72]	-	5000 x 500 x 90	2	600	-	0,50	0
			5000 x 500 x 90	2	600	-	0,30	0
Kolb 1977	[99]	-	8000 x 550 x 80	2	4000	-	0,55	0
Penttala 1980	[100]	a	4000 x 500 x 90	1	1050	-	0,51	0
			4000 x 500 x 90	1	600	-	0,50	0
			4000 x 500 x 90	1	600	-	0,30	0
		b	5000 x 800 x 115	1	820	-	0,50	0
			5000 x 800 x 115	1	1600	-	0,38	0
Johannesson 1983	[101]	a	5000 x 500 x 90	2	650	-	0,50	0
		a	5000 x 500 x 90	2	1400	-	0,50	0
			5000 x 500 x 90	2	300	-	0,50	0
			5000 x 500 x 90	2	300	-	0,25	0
		b	5000 x 500 x 90	1	2500	-	0,50	0
		d	5000 x 495 x 88	4	1250	-	0,25	0
			5000 x 495 x 88	4	1250	-	0,80	0
		e	5000 x 495 x 88	1	2500	-	0,80	0
Johannesson 1983	[101]	e	5000 x 495 x 88	1	2500	-	0,80	0
Hallström 1995	[76] [77]	-	4000 x 315 x 90	5	875	-	0,45	0
Höfflin 2005	[104]	a	3150 x 450 x 120	5	675	-	0,20	0
			3150 x 450 x 120	6	675	-	0,30	0
			3150 x 450 x 120	4	675	-	0,40	0
		b	6300 x 900 x 120	5	1350	-	0,20	0
			6300 x 900 x 120	6	1350	-	0,30	0
			6300 x 900 x 120	6	1350	-	0,40	0

Table 3.2 continued…								
Author and year	**Ref.**	**Series**	**L x H x B [mm]**	**n**	**$L_A + h_r$ [mm]**	**$L_Z + h_d$ [mm]**	**h_d/h [-]**	**e/h [-]**
Höfflin 2005	[104]	c	4675 x 450 x 120	5	1463	-	0,30	0
		d	9450 x 900 x 120	5	2925	-	0,30	0
Aicher 2006	[46] [79]	a	4675 x 450 x 120	6	1263	-	0,40	0
		b	9450 x 900 x 120	4	2925	-	0,20	0
			9450 x 900 x 120	5	2925	-	0,40	0
		c	4500 x 450 x 120	3	2250	-	0,40	0
		d	9000 x 900 x 120	3	4500	-	0,40	0

Table 3.3: Experiments on glulam beams with circular holes without reinforcement. Literature from the year 2006-2021.

Author and year	**Ref.**	**Series**	**L x H x B [mm]**	**n**	**$L_A + h_r$ [mm]**	**$L_Z + h_d$ [mm]**	**h_d/h [-]**	**e/h [-]**
Aicher 2009	[90]	-	3150 x 450 x 120	3	675	-	0,40	0
Hijikata* 2010	[87]	a	4000 x 330 x 120	3	2000	-	0,40	0.167
		b	4000 x 330 x 120	3	2000	-	0,40	0.120
		c	3000 x 330 x 120	3	300	-	0,40	0.167
			3000 x 330 x 120	3	300	-	0,40	0.120
			3000 x 330 x 120	6	300	-	0,40	0.060
Danzer 2016	[69]	a	2650 x 400 x 120	3	600	-	0,35	-0,175
			2650 x 400 x 120	3	600	-	0,35	-0,100
			2650 x 400 x 120	3	600	-	0,35	0,100
			2650 x 400 x 120	3	600	-	0,35	0,175
		b†	3750 x 400 x 120	3	600	280	0,35	0
			3750 x 400 x 120	3	600	420	0,35	0
			3750 x 400 x 120	3	600	560	0,35	0
		c‡	2650 x 400 x 120	3	600	180	0,25	±0.225
		d	2650 x 400 x 120	3	600	-	0,25	-0,225
			2650 x 400 x 120	3	600	-	0,25	-0,100

Table 3.3 continued…								
Author and year	**Ref.**	**Series**	**L x H x B [mm]**	**n**	**$L_A + h_r$ [mm]**	**$L_z + h_d$ [mm]**	**h_d/h [-]**	**e/h [-]**
Danzer 2016	[69]	d	2650 x 400 x 120	3	600	-	0,25	0,100
			2650 x 400 x 120	3	600	-	0,25	0,225
Karimi 2021	[106]	-	2900 x 420 x 85	2	750	-	0,43	0
Okamoto 2021	[70]	a	1000 x 150 x 105	5	350	-	0,20	0
			1000 x 150 x 105	5	350	-	0,20	0
		b	2000 x 300 x 105	5	700	-	0,10	0
			2000 x 300 x 105	5	700	-	0,20	0
			2000 x 300 x 105	5	700	-	0,33	0
		c	3000 x 450 x 105	5	1050	-	0,07	0
			3000 x 450 x 105	5	1050	-	0,20	0
			3000 x 450 x 105	5	1050	-	0,40	0
Lechner 2021	[92]	-	1920 x 320 x 180	4	480	-	0,40	0

Table 3.4: Experiments from the literature regarding reinforced holes in glulam beams from 2009-2021.

Author and year	**Ref**	**S.**	**Reinf. type**	**L x H x B [mm]**	**n**	**$L_A + h_r$ [mm]**	**$L_z + h_d$ [mm]**	**h_d/h [-]**	**e/h [-]**
Aicher 2009	[90]	-	Steel rods	3150 x 450 x 120	6	675	-	0,40	0
			Screws	3150 x 450 x 120	6	675	-	0,40	0
Hijikata 2010*	[87]	a	Plywood	4000 x 330 x 120	3	2000	-	0,40	0
				4000 x 330 x 120	3	2000	-	0,40	0
			Steel plates	4000 x 330 x 120	3	2000	-	0,40	0
			Steel plate	4000 x 330 x 120	3	2000	-	0,40	0
		b	Steel plate	3000 x 330 x 120	6	300	-	0,40	0
				3000 x 330 x 120	6	300	-	0,40	0
			Steel plates	3000 x 330 x 120	6	300	-	0,40	0
Aicher 2011	[86]	-	Steel rods	3150 x 450 x 120	2	675	-	0,40	0
			Screws	3150 x 450 x 120	6	675	-	0,40	0
			Plywood	3150 x 450 x 120	5	675	-	0,40	0

Table 3.4 continued…									
Author and year	**Ref**	**S.**	**Reinf. type**	**L x H x B [mm]**	**n**	**$L_A + h_r$ [mm]**	**$L_Z + h_d$ [mm]**	**h_d/h [-]**	**e/h [-]**
Danzer 2016	[69]	a	Screws	2650 x 400 x 120	3	600	-	0,35	-0,175
				2650 x 400 x 120	3	600	-	0,35	-0,100
				2650 x 400 x 120	3	600	-	0,35	0,100
				2650 x 400 x 120	3	600	-	0,35	0,175
		b†	Screws	3750 x 400 x 120	3	600	280	0,35	0
				3750 x 400 x 120	3	600	42	0,35	0
				3750 x 400 x 120	3	600	560	0,35	0
		c‡	Screws	2650 x 400 x 120	3	600	180	0,25	±0,225
Lechner 2021	[92]	-	Vertical LVL inside GLT	1920 x 320 x 180	6	480	-	0,40	0

* Based on Scots Pine glulam beams, all reinforcements cover half of the beam height (from bottom to the middle).

† Two holes are arranged horizontally along the beam.

‡ Two holes are arranged vertically with eccentricity. A negative sign indicates eccentricity above the neutral axis and positive means below it.

3.8.1 Summary of the literature review

Various test methods have been applied in the found literature, some using a three- and four-point bending test and other techniques that are not according to standards. Experiments on beams with holes have been with a relatively consistent specimen thickness between 80 to 180 mm. Most found experiments are with a specimen height between 400 to 500 mm. Hole diameter has been consistently below or equal to 40 % of beam height, with a few exceptions challenging this limit regarding unreinforced hole areas. A gap was found regarding reinforced holes greater than 0,4 h_d/h. Only 12 samples of glulam beams with two consecutive holes were observed in this literature review. The reinforcement techniques using plywood or LVL on-plane are also commonly applied in other situations, like for notched and curved beams, which may explain why most of the recent literature with holes has focused on threaded screws and steel rods.

4 Research question

The main goal of this thesis is to contribute to the field of fracture analysis of timber structures by combining multiple established methods to create a finite element model efficiently. Previous research has shown to cover singular, smaller holes mostly. A goal is to shed some light on the reinforcement of multiple large holes in glulam beams, ultimately with a long-term hope to improve the competitiveness of timber constructions, specifically by making room for large technical infrastructure without losing ceiling height.

The problem area presents the following questions:

- How are simply supported glulam beams affected by a large hole when subjected to bending and shear, with and without reinforcement?
    - How can cracks be effectively detected and measured during experiments and used in an FE-model?
    - How does numerical data from finite element analyses correlate to experimental results?
    - How can experimental results from DIC be utilized to update the finite element model?

The limitations of this thesis are as follows:

- Although moisture content in the materials during experiments is documented, the moisture and temperature effects on strength are not calibrated.
- Glue lines are not considered in the FE-model.
- Transversal isotropy is assumed, and perpendicular stiffness is based on a formula.
- A bilinear cohesive traction-separation behavior is assumed, even though previous research indicates exponential degradation to be more accurate.
- Cohesive material properties are based on literature for an initial guess.

The main reasons for simplifications are simply the lack of experimental data on the materials used in this thesis.

5 Materials

The experimental program involves four thin, combined glulam beams of Norway Spruce (Picea abies) species, with two consecutive holes of 170 mm in diameter (0,57 h_d/h), from a single manufacturer. Series A concerns two unreinforced beams, while B is two beams with glued-on plywood. All the specimens had pre-cut holes, and the reinforcement was also preliminarily mounted. Table 5.1 shows the dimensions of the four samples and the reinforcement used.

Table 5.1: (a) Dimensions of experimental specimens, (b) dimension of reinforcement on series B.

Series	L x H x B	n	Reinforcement
A	5700 x 300 x 36	2	None
B	5700 x 300 x 36	2	Plywood on both sides

(a)

Reinforcement on B	l_r x h_r x t_r
Glued-on-plane plywood	1200 x 290 x 12

(b)

The glulam elements have a global MOE of approximately 11 000 MPa, which equals to GL24c class according to EN 14080 [32], with a mean density of 460 kg/m^3 [108]. The outer lamellas in the beam cross-sections are of C30-quality, each measured between 46-50 mm. The middle material section consists of 10 laminated parts, measured height between 18-21 mm. These are of ungraded timber quality, which means that the strength is not tested individually. Therefore, E = 6000 MPa is assumed initially for this section. See Figure 5.2 for photographs of the four beams and the layer compositions.

The hole placement is in the middle of the gravity, which involves the weakest part of the glulam cross-section, as seen in Figure 5.1(a). The reinforced beams in series B have spruce plywood glued on each side [109] and eight small screws. See Figure 5.1(b) for an illustration of the reinforced area.

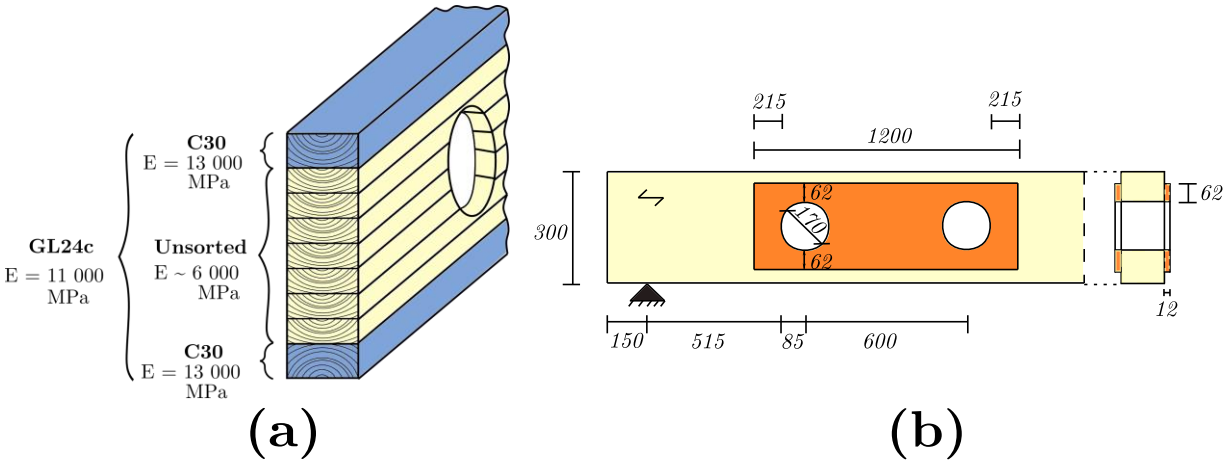

(a) (b)

Figure 5.1: (a) Quality of the glulam beam components in this project. (b) Placement of holes and reinforcement.

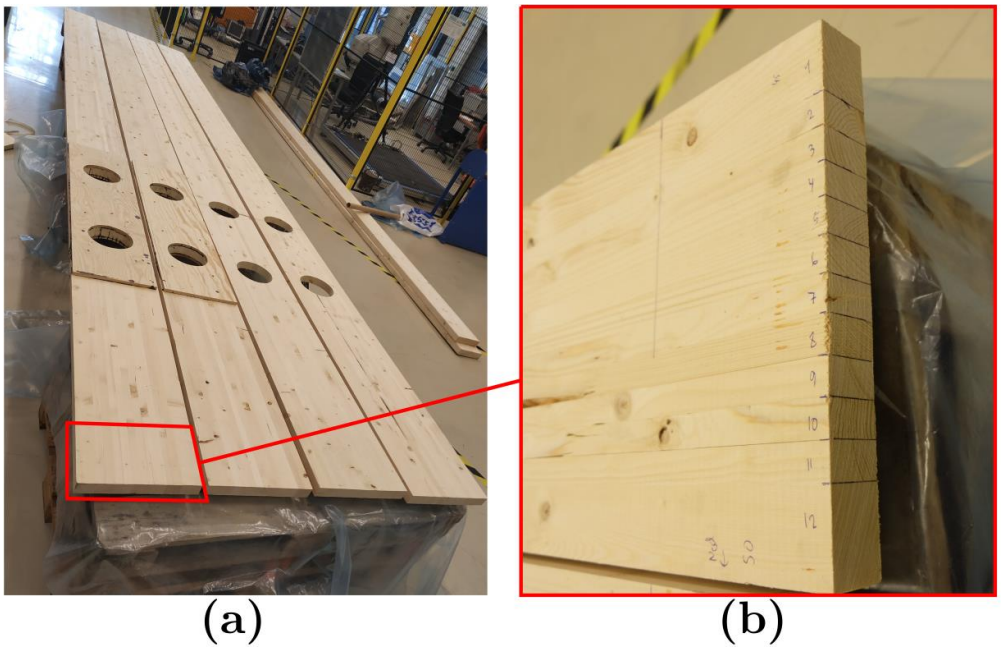

Figure 5.2: Photographs of (a) the four beams and (b) layers of timber (1-10-1).

5.1 Visual observations of material quality and flaws

The beams were straight with no indication of bowing or twisting, without any splitting of end-grain. Test series B did not have any visible flaws due to reinforcement covering the area, and knots on the plywood had been plugged (see Figure 5.5b). Tension and compression lamellas were of high quality, with small knot density. However, there were some natural flaws in the middle part, as can be expected due to low quality (see Figure 5.3 and Figure 5.4 accordingly):

1) A long wane-edge in a critical zone was measured to be approximately 700 mm on specimen A1, which extends to the beginning of the right part of the hole at the expected crack area
2) Large knot density, especially between holes on specimen A1
3) A large knot-hole in the middle of specimen A2
4) All test specimens had finger joints going through all layers of timber at the second hole (the right hole)

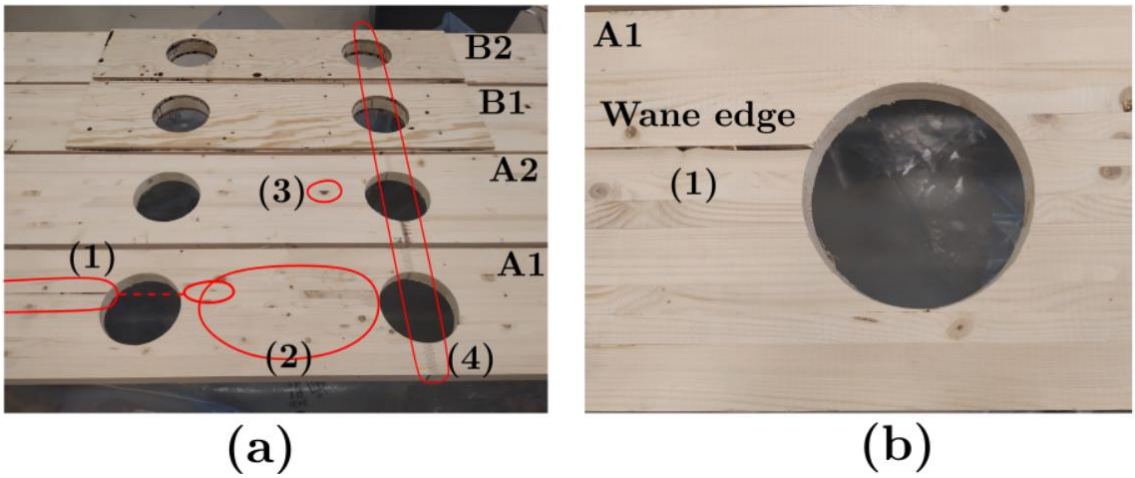

Figure 5.3: Photographs of (a) material flaws (all specimens) and (b) wane edge on specimen A1.

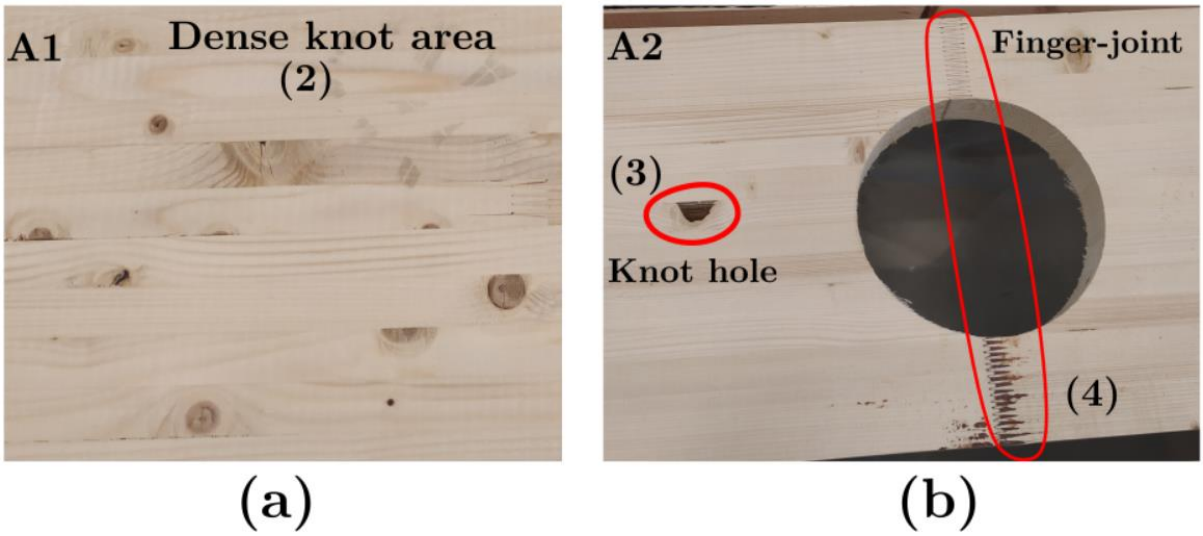

Figure 5.4: Photographs of (a) a dense knot area on specimen A1 and (b) a large knot hole on specimen A2 between the two holes.

One of the specimens, A1, had a significant dimension difference of 6 mm at the finger joint, as seen in Figure 5.5. This caused the beam to curve slightly outwards before any load was applied.

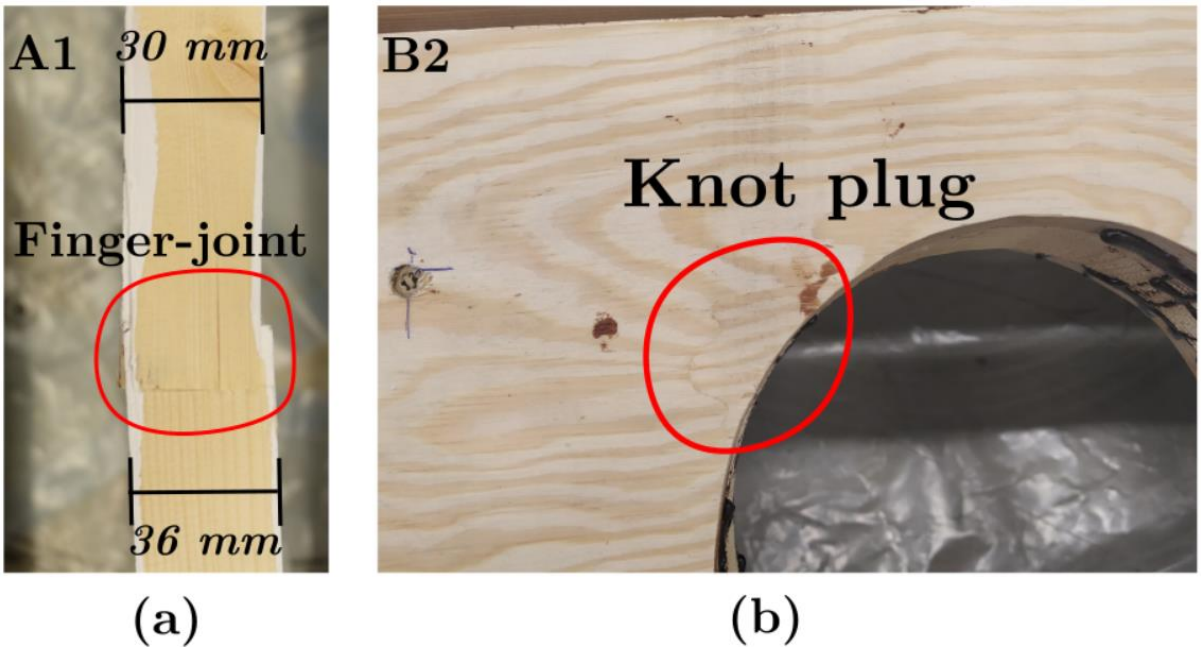

Figure 5.5: Photographs of (a) thickness discrepancy at finger-joint on specimen A1 and (b) knot plugging on the plywood reinforcement.

6 Methods

In this chapter, all used methods are described in the subchapters, consisting of; (i) the experimental setup with explanations and illustrations, (ii) the procedure for the finite element analyses is explained thoroughly in steps, and lastly, (iii) the specific DIC post-processing data extraction procedures.

6.1 Experimental methods

A four-point bending test setup at the University of Agder was used for the experiments consisting of two unreinforced (Series A), and two reinforced (Series B) combined glulam beams, each with two consecutive holes. The experiments were recorded with Digital Image Correlation (DIC) and analyzed through VIC-3D software. The hole areas in series B are reinforced with spruce plywood and attached to the beam with adhesives and eight small screws (see Table 5.1 for dimension and material details).

6.1.1 Four-point bending test setup

All glulam test specimens have two holes, each with a 600 and 1200mm distance to the nearest support. Figure 6.1 illustrates the experimental setup. The selection of test method and hole modification is mainly to achieve a basis of comparable data in correlation to experimental results done by the Norwegian Institute of Wood Technology (NIWT) (Appendix A).

An INP-260 steel beam was subjected to a vertical, centered point load from the actuator with a limit of 200 kN, which then distributed the force on two points onto the glulam beams. According to EN 408 [110], the guidelines state that the width of these points shall not exceed half of the glulam beam depth, which is cylindrical in these experiments and therefore within the requirements. Concrete elements with small steel cylinders supported the glulam beam. Steel brackets on both sides were intended to prevent out-of-plane buckling.

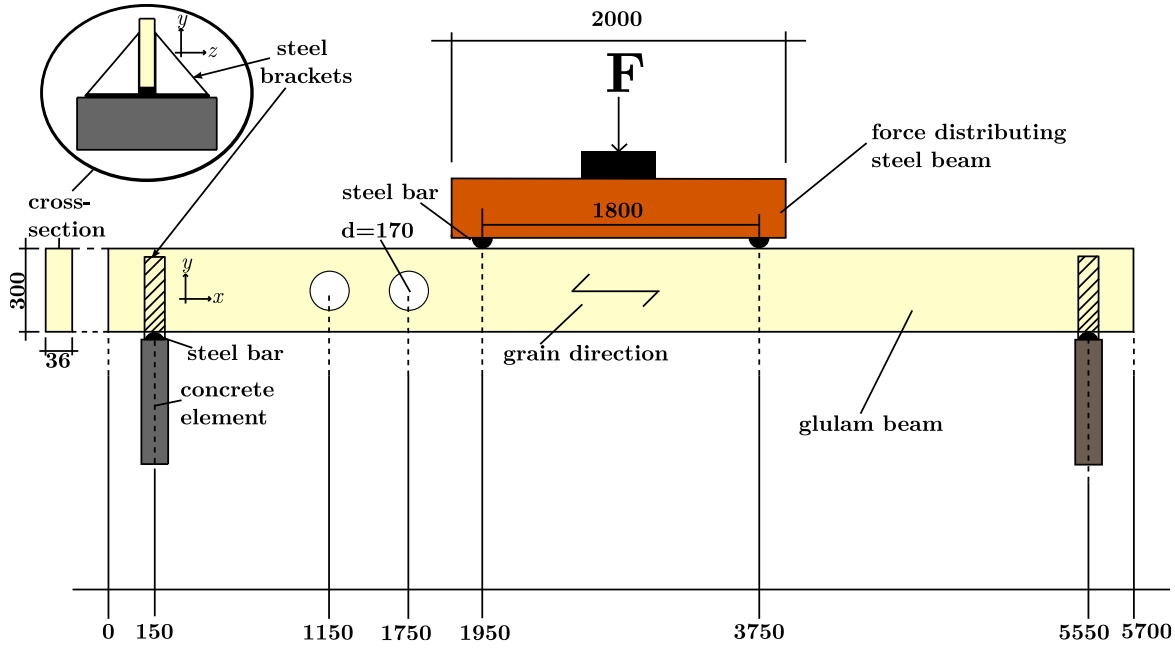

Figure 6.1: The applied test setup of glulam beams, subjected to a centered point-load, distributed by a steel beam. The supports consist of two concrete elements, each with a steel bracket.

In this project, a four-point bending method was selected over a three-point to avoid premature failure due to stress concentrations in the bending area.

The UiA laboratory did not have the necessary equipment to perform a four-point bending test on long beams, both in terms of a support system and load-distributing steel beam. An optimal setup would be a permanent floor-mounted setup with adjustable support distance, with a mechanism to avoid lateral displacement. Moreover, it was not allowed to drill holes in the UiA concrete floor to install secure supports to prevent sliding and tilting. Therefore, alternative solutions were improvised to solve these challenges. Two roadside crash-barrier concrete elements were used to support the beams (Figure 6.2). These elements are stable from sliding and tilting without any mechanical fastening to the floor because of their broad feet and heavy weight. A steel cylinder holds the beams on each end, similar to the load condition. The reason behind the procedure was to secure the glulam beams from rotation and raise the height to surpass the actuator base and allow bending.

Figure 6.2: Support boundary with a frictionless steel bracket working as a lateral restraint.

6.1.2 System data overview

A transducer and different technologies are utilized to gather the required data for further analysis. Figure 6.3 illustrates the interacting parts of the system. The load and transducer outputs are compared with the DIC output relative to the picture index, which accurately represents displacement, load, and time.

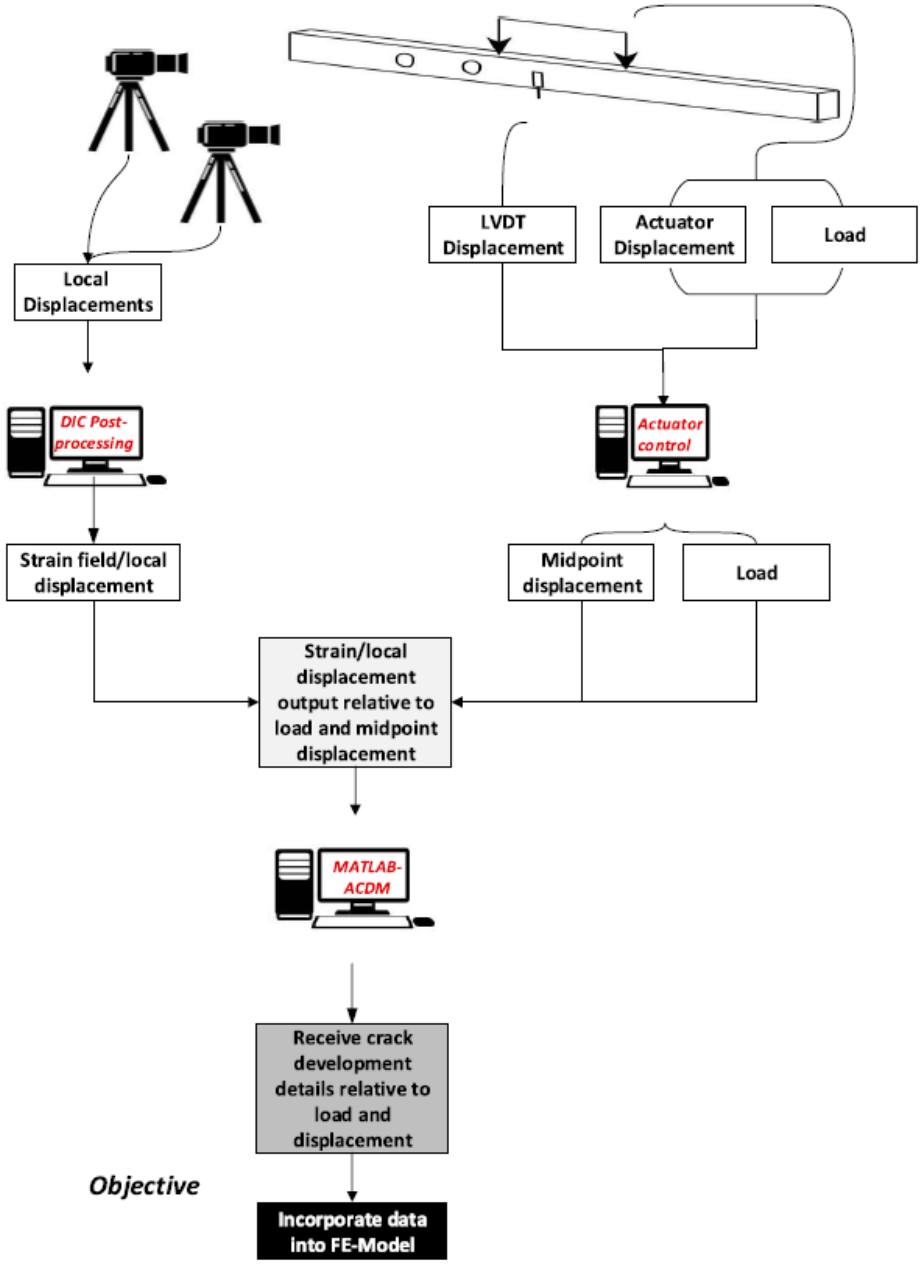

Figure 6.3: Data in- and outputs.

6.1.3 Actuator

The four tests used displacement control, with 0,13 mm/sec constant incrementation, to stay within the interval of $180\ s \leq F_{max} \leq\ 420\ s$, according to EN 408 [110]. The LVDT and actuator registered output two times per second.

6.1.4 Midpoint displacement

The displacement of the experiments was measured using a linear variable differential transducer (LVDT) with a stroke length of 250 mm on beam midpoints. The accuracy of the equipment is ±0,3 % = 0,75 mm. However, the signal output was in voltage originally and was connected to the actuator, and thus a recalibration was necessary to achieve comparable signals. The equipment was

supposed to be linear, but minor discrepancies were detected when measuring preliminary to the experiments. The calibration resulted in an approximate accuracy of ±0,8 mm. Appendix B presents the calibration process with the related calculation formula. Because of the long-stroke length of the equipment, it was necessary to place the LVDT on the side of the beam, with the stroke touching the actuator base, as seen in Figure 6.4. Ideally, the LVDT should be placed oppositely, with the stroke touching the beam instead. The LVDT was attached with duct tape to avoid penetration of the wood with screws/nails, which may affect the results.

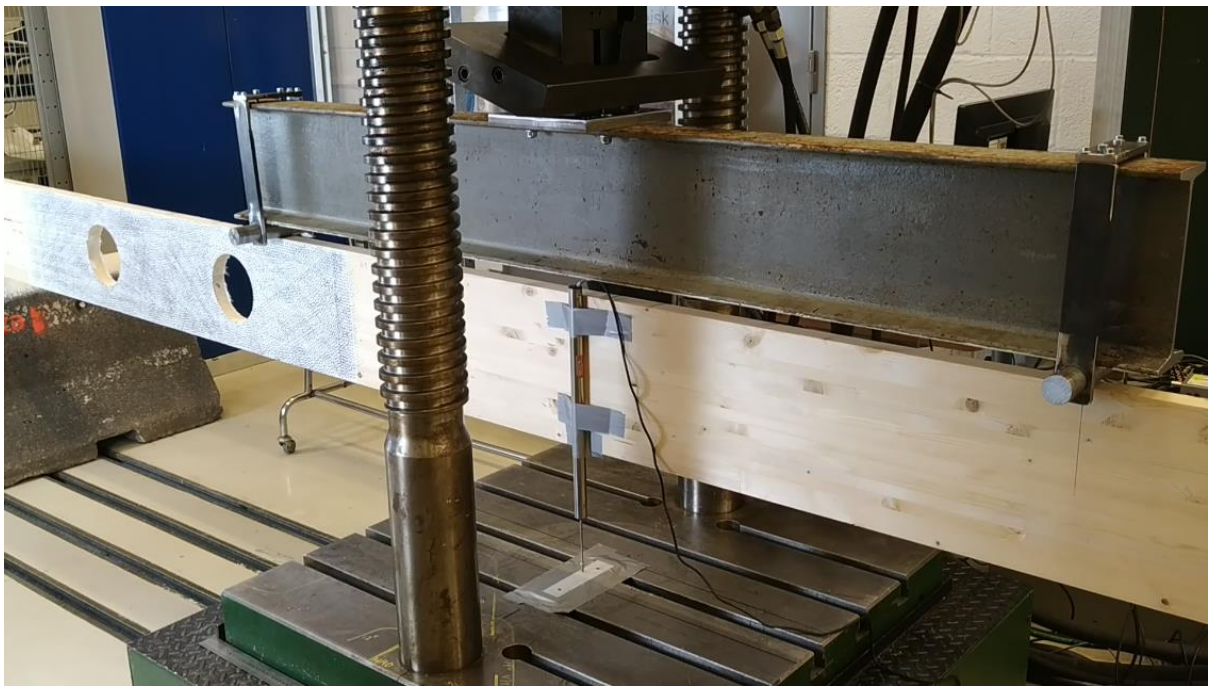

Figure 6.4: Centrical placement of the LVDT with stroke touching the actuator base.

6.1.5 Digital Image Correlation setup and preparations

Initially, white paint was applied on all four test specimens to create a contrast for the cameras to accurately detect displacements, followed by a black speckle pattern application with an ink roller (see Figure 6.5) after at least 24 hours of drying. The dot sizes had a uniform diameter of 1,27 mm (0,05 inches), as instructed by the manual [111] when using 16 MP cameras in a field of view (FoV) within the interval of {770-2060 mm}. Furthermore, the pattern was randomly applied with ink 5-10 times in an attempt to cover half of the area with speckle pigments. The chosen FoV was equal to 215 mm from each side of the holes and covered the beam height (L = 1500, H = 300 mm). The selected length was to produce an analysis field 150 mm adjacent to the reinforcement on each side.

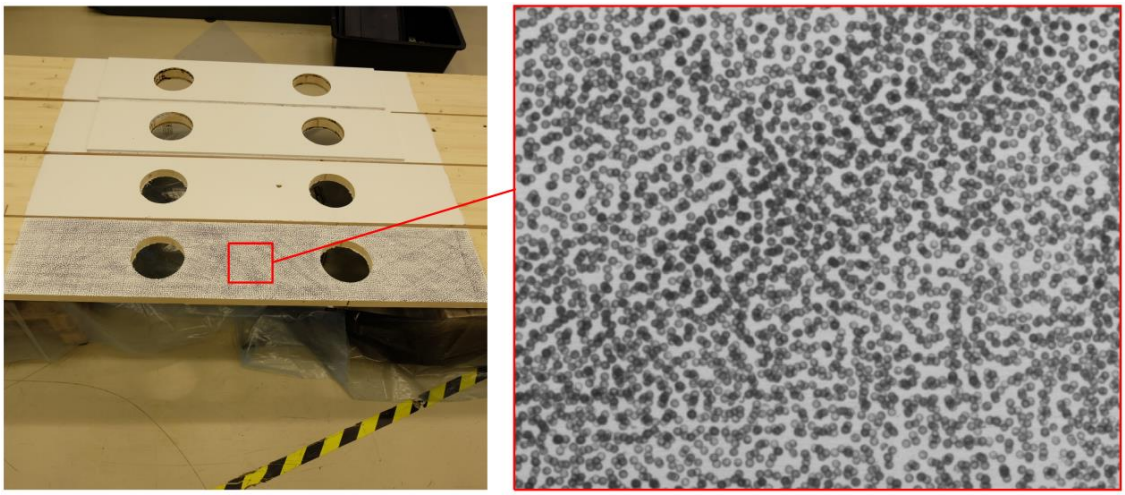

Figure 6.5: Example of a speckled area.

Due to the wide FoV, the camera setup was vertically aligned (see Figure 6.6b) to follow the instructions from technical support. The camera distance to the beams was 1780 mm, which ideally should have been equal to the FoV, but the cameras were placed further back due to calibration focus. An ideal theoretical distance between cameras is equal to half of the depth, which equals 890 mm in this case. It was, however, necessary to decrease this to 830 mm because the camera stand was blocking the view.

Two cold spotlights were facing toward shoot-through umbrellas for adequate light quality to create necessary contrast on the speckles. Both cameras capture five high-resolution pictures every second, which means that the output could either be downscaled relative to the output from the actuator or, conversely, the actuator output upscaled to match the DIC output frequency. Downscaling was chosen to avoid interpolation between measured points.

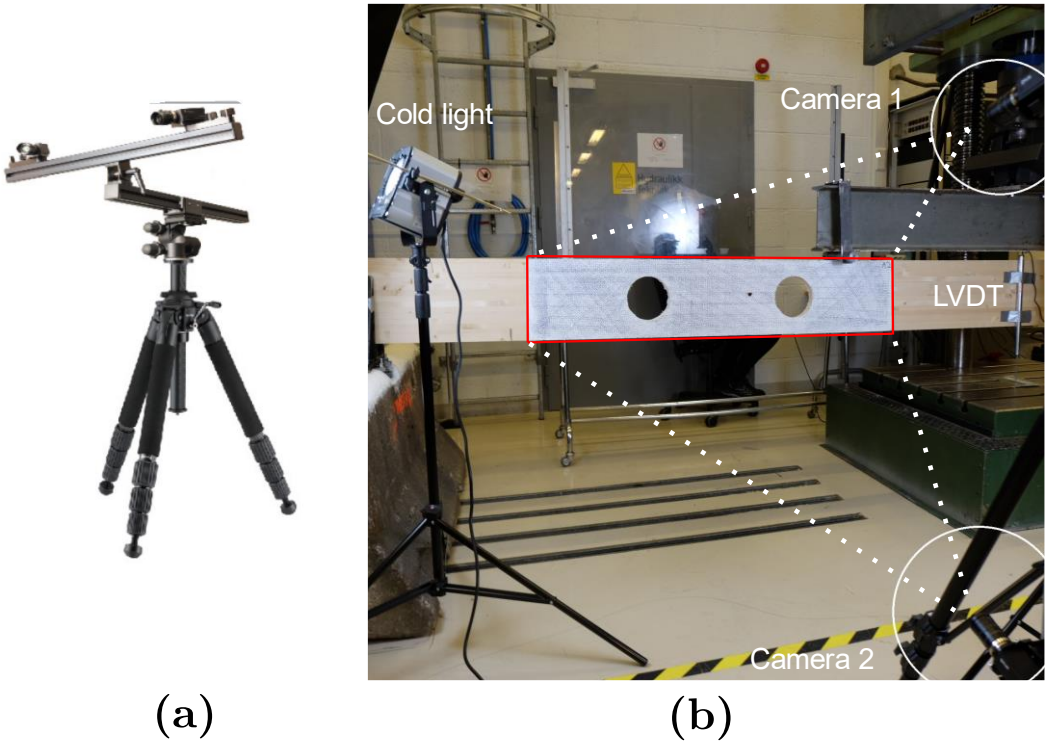

Figure 6.6: (a) shows DIC cameras on an anti-vibration stand as used in this project [112], and (b) shows a picture of the vertical alignment of the cameras facing the speckled area.

6.1.6 Moisture content

A pin-less moisture encounter measured the moisture content right after each test. Figure 6.7 shows a picture of the equipment. It creates an electrical field inside the depth of the material in a range between 10 and 30 mm, ranging from 5 to 30 % moisture content. The moisture content was noted for each meter of the beam span, resulting in five readings per specimen. The measurements were rounded to the nearest 0,5% because the display was difficult to read more accurately (design inaccuracy). Note that this apparatus deviates from the standard EN 13183-2, which recommends equipment with electrode pins. Documentation of values can be found in Appendix C.

Figure 6.7: Tramex moisture content encounter

6.2 Numerical methods

A finite element model was created in ABAQUS with identical dimensions and modifications as the experiments without reinforcement. The modeling process, material, and cohesive layer parameters are further explained in this section.

6.2.1 Finite element modeling details

All modeling was done through ABAQUS/Standard 2020 using python scripts. Every process was edited to variables and defined in the code to calibrate model parameters and execute many analyses automatically.

First, a beam was initially created and cloned two times with identical material and hole dimensions equal to the experiments. Secondly, these were then divided into three different beam parts (top, middle between holes, and bottom, Figure 6.8) to deploy a cohesive layer on the surfaces (SCZM), which allows fracture mechanics considerations in the model (Figure 6.8). Thirdly, partitions divided the beam into heterogenous material sections (higher stiffness on top and bottom, while lower in the mid-lamellae, similar to Chapter 5). Additional vertical partitions and a horizontal was placed centrically at the reinforced area to provide a good mesh division. Figure 6.8 illustrates the sections of the model and the cohesive layer. Master and slave surfaces were defined as the cohesive layer between parts, placed at a 45° angle (+180°) clockwise. These are the expected crack-plane locations, based on literature for holes within the moment and shear region, as previously introduced in Chapter 3.4. The surface interaction acts as a hard contact between the model elements in an

undamaged state while tangentially frictionless. Next, bilinear traction-separation cohesive law was introduced to the model (theory in Chapter 3.5.1). The four-point bending test setup from the experiments (section 6.1.1) was replicated, while the load was a 100 mm vertical imposed displacement. Moreover, the power-law criteria in eq. (3.12) is applied to the model.

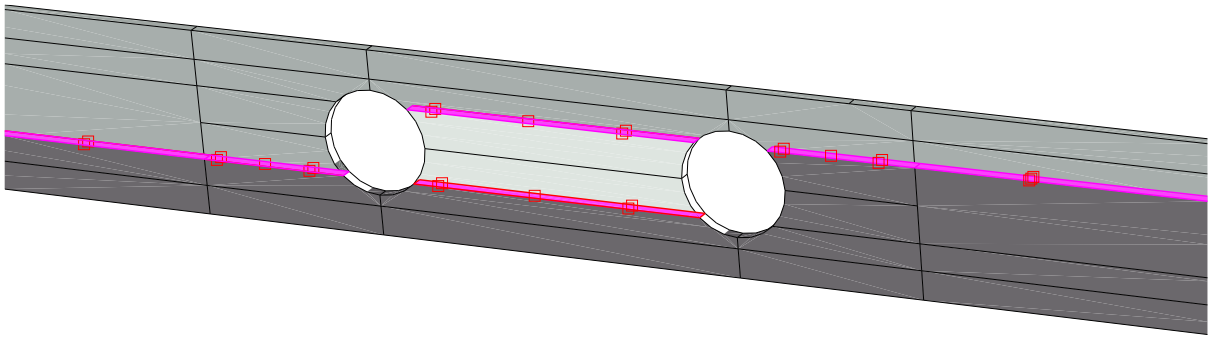

Figure 6.8: Shades of grey indicate different parts of the model divided into three. The purple lines illustrate the cohesive surface layer.

Z-symmetry was applied across the surfaces on the vertical y-plane; this reduces model size in half and computation time. Additionally, it simplifies the model by neglecting the effects of torsional rotation. An eight-node hexagonal mesh was used with reduced integration (C3D8R), with a global size of 18 mm. Re-meshing was done with half the size, 9 mm, near the hole vicinity, which encloses the same area as the FoV in the DIC setup. Moreover, this mesh was chosen to achieve two brick elements in the width, thus further reducing computation time. See illustrations in Figure 6.9-Figure 6.10 of the mesh area divided into model parts, a zoomed picture of the hole vicinity, and the reinforced model.

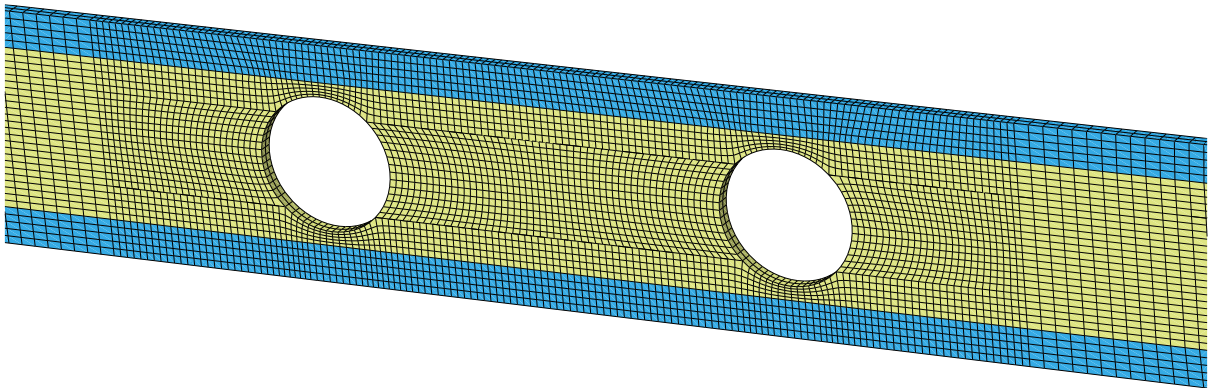

Figure 6.9: Illustration of the transition between coarse (18 mm) and refined (9 mm) mesh.

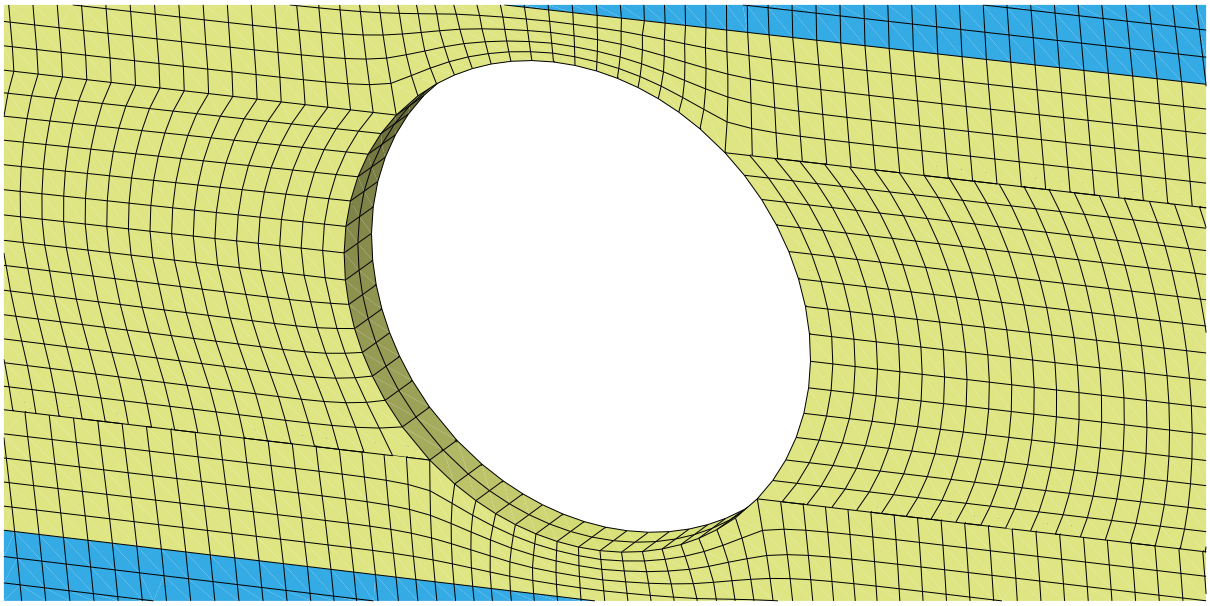

Figure 6.10: Zoomed illustration of the mesh grid.

6.2.2 Material parameters

Linear-elastic orthotropic material properties are used on the beam globally while in undamaged conditions and outside the fracture zone outlined by the cohesive layers. Known material parameters are shown in Table 6.1, with their associated references based on experimentally derived data of similar material quality and dimensions.

Table 6.1: Material properties

Part	E_x [MPa]	E_{transv} [MPa]	G_{xy} [MPa]	G_{xz} [MPa]	G_{yz} [MPa]	v_{xy} [–]	v_{xz} [–]	v_{yz} [–]
Ref.	App. A	Eq. (3.7)	Eq. (3.8)	Eq. (3.8)	Eq. (3.8)	[113]	[113]	[113]
Glulam beam (global)	11 000	367	688	688	69	0,02	0,02	0,3
Ref.	[109]	[109]	[109]	[109]	[109]	[114]	[114]	[114]
Plywood Reinf.	10 235	1 765	350	350	350	0,06	0,4	0,4

Note that the global glulam beam parameters are listed; this is due to the unknown quality of the middle section. Therefore, a parametric, linear-elastic sensitivity analysis was carried out to achieve values that reflect the heterogenous cross-section.

6.2.3 Elastic analysis

A simple linear-elastic beam FE-model without contributions from cohesive layers and linear geometry (no holes) was analyzed to find the optimal moduli of elasticity and shear of the individual lamellae. Sobol's Sensitivity Analysis [115] was used with the Python module *SALib.sample.saltelli* [116]. After that, the optimized parameters were applied to the cohesive model. The number of iterations is $N * 2D + 2 = 5120$, where N is the integers $(= 512)$ and D are E_x and G_{xy}, for both top/bottom and middle lamellae $(= 4)$, which are the material parameters to be analyzed (Table 6.2).

Table 6.2: Range of elastic parameters regarded in the optimization analysis

Parameter	$E_{x,top/bot}$	$G_{xy,top/bot}$	$E_{x,mid}$	$G_{xy,mid}$
Range	$13000 \pm 25\%$	$750 \pm 25\%$	$6000 \pm 25\%$	$450 \pm 25\%$

Another series of elastic analyses were conducted using a single hole to determine the change in stress distribution relative to hole placement along the beam length, with 5 mm increments. The hole location is within the interval of 385 to 2850 mm, which is according to upcoming design rules that set a minimum distance between hole to beam end, L_V (Table 3.1). The end point indicates the mid-span of the beam (symmetry). A total of $\frac{2850-385}{5} = 493$ model iterations were carried out.

6.2.4 Initial guess of cohesive layer properties

Ideally, fracture parameters are determined experimentally. However, since this is beyond the scope of this thesis, cohesive layer properties are found based on existing literature. Table 6.3 presents these values, where σ_{ini} and τ_{ini} are the maximum nominal and shear stress to initiate damage in modes I and II. Furthermore, G_{FI} and G_{FII} are the fracture energy related to modes I and II, and μ is the viscosity parameter.

Table 6.3: Cohesive layer properties (initial guess values used in this thesis)

Part	σ_{ini} [MPa]	τ_{ini} [MPa]	G_{FI} [N/mm]	G_{FII} [N/mm]	μ [–]
Ref.	[5]	[5]	[5]	[5]	[5]
Initial input	2	6,2	0,7	1,2	0,0001

6.3 DIC post-processing

All four beams were analyzed according to the rule of thumb in eq. (3.24) with minor discrepancies depending on the calibration of the software. Initial analyses with step size 20 were used (Figure 12.3, Appendix D), but some grey areas around holes were not detected. Therefore, a step size of 10 was used instead (Table 6.4), which gave a low uncertainty interval (see an example of this in Figure 6.11) without missing parts throughout the analysis. A further decrease in step size was tested but decreasing from 10 to 5 resulted in a computation time increase from 4 to 13 hours for each simulation, without including the extra data export processing, which was not feasible in this project.

Decreasing the subset size resulted in some missing areas throughout the analysis. Furthermore, the recommended subset setting proved to be the most consistent, then used for all cases. The area of interest (AOI) was defined with a rectangle to cover the speckled area (see Figure 6.12), with some minor adjustments around the load condition and removal of holes. For the reinforced beams, it was necessary to define the AOI by three individual rectangles because the program would neglect a large part of the beam otherwise, likely because of the sudden jump in-depth at the transition from beam to reinforcement.

Table 6.4: Details of the step, filter, and subset sizes

Series	Step size	Filter size	Subset size (Recommended)
A	10	7	61
B	10	7	63

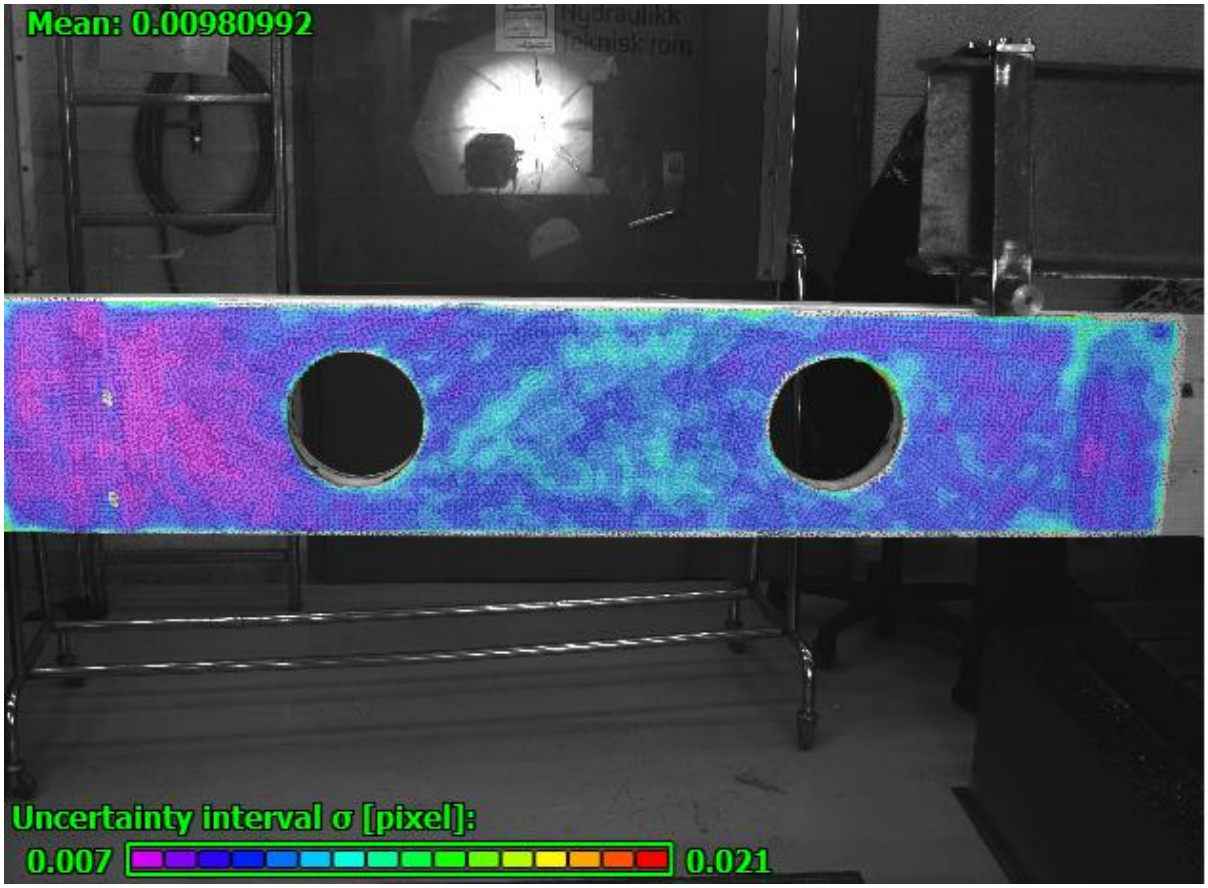

Figure 6.11: Uncertainty interval related to subset size. The darker, purple/blue areas indicate better accuracy. Notice some small grey spots at the reinforcement edge because of the depth difference. This example is from specimen B1.

Figure 6.12: Defined area of interest with a cutout around the hole area. This example is from specimen B1.

6.3.1 Data extraction

Peak-strain area levels were evaluated by selecting four points perpendicular to the grain ε_{yy}, where cracking occurred on both unreinforced beams. An additional six points of ε_{xx} were extracted, then compared to the FE-analyses. Figures are presented together with these points and their respective data in the following chapter (Figure 7.3 and Figure 7.7).

6.3.2 MATLAB-ACDM post-processing of DIC results

The images gathered from the DIC experiments were further processed in MATLAB 2021a using the automatic crack detection and measurement (ACDM) tool [96]. Cracks were rendered by the tool in a 1:1 coordinate system (mm), which enabled the calculation of crack occurrence and its diagonal length relative to the picture numbers, load, and displacement. However, some minor adjustments were made because line crooking was not adaptable to the cohesive layer in ABAQUS: A diagonal length was calculated for start/end nodes for each crack length increment. Furthermore, the recommended strain threshold was estimated to be 10 mm/m (≈ 1+9 mm/m) [96]. However, manual measurements indicated that 5 mm/m would give the best representation of experiments; it was, therefore, used to compute the crack length.

7 Results

First off, this chapter presents the experimental results of the four glulam specimens, which are conducted according to the four-point bending procedure (see details of materials in Chapter 5 and section 6.1 for the test setup and methods). Next, the results from elastic FE-analyses are presented, including best-fit material parameters and hole placement to angle relation by applying a four-point setup and an evenly distributed load. Then, the unreinforced cohesive FE-model is compared with experimental results regarding force and crack length relative to displacement. Finally, a method and function are developed to update the cohesive layer parameters, although not validated in this present work.

7.1 Experimental results

7.1.1 Unreinforced beams

Figure 7.1 shows the force/displacement behavior (left y-axis, blue line) of experiment A1 but also presents an issue regarding out-of-plane displacement (right y-axis, orange line), which was seen visually during tests and measured from the DIC stereo-triangulation. Therefore, results after this issue occurs, e.g., up to 40 mm displacement (black vertical line), will be disregarded further in FE-model validation. Additionally, the crack initiation and propagation were analyzed during DIC post-processing, utilizing the ACDM MATLAB extension to detect cracks relative to the displacement output from the LVDT. Fracture points are shown by red circles in Figure 7.1 and ordered by numbers, compared with Figure 7.2, which shows the crack length increments.

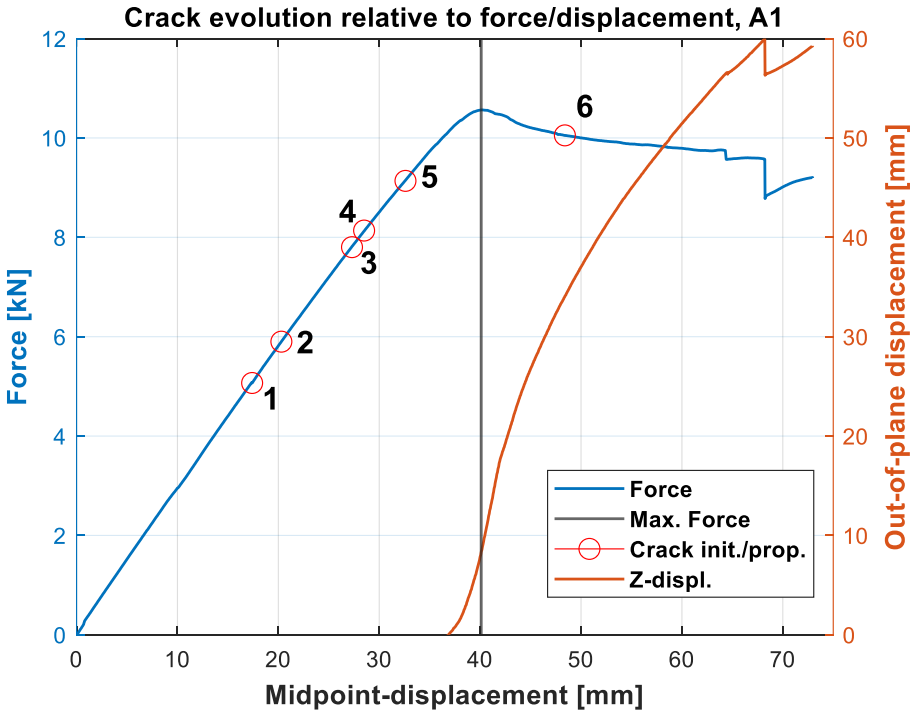

Figure 7.1: Crack evolution relative to force and displacement of specimen A1.

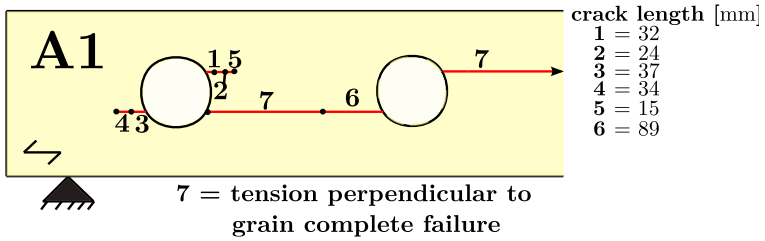

Figure 7.2: Sketch of the crack evolution of specimen A1. Crack length increments are shown to the right.

Ten points are defined in the DIC post-processing software (Figure 7.3), which will later be used to compare with the FE-model. Six of these points (P0-P5) are used to extract strain data along the grain (Figure 7.4a), and the other four (P6-P9) extract strain data perpendicular to the grain (Figure 7.4b). These are chosen with regards to the first crack occurrences. P8 is the most intense point in this case. In the area near the loading condition, P5 (+ for tension) and P2 (- for compression) have the most significant strain outcome along the grain. For more illustrations/contours of DIC post-processing, see Appendix D. Moreover, the numerical data of strain and crack length can be found in Appendix E.

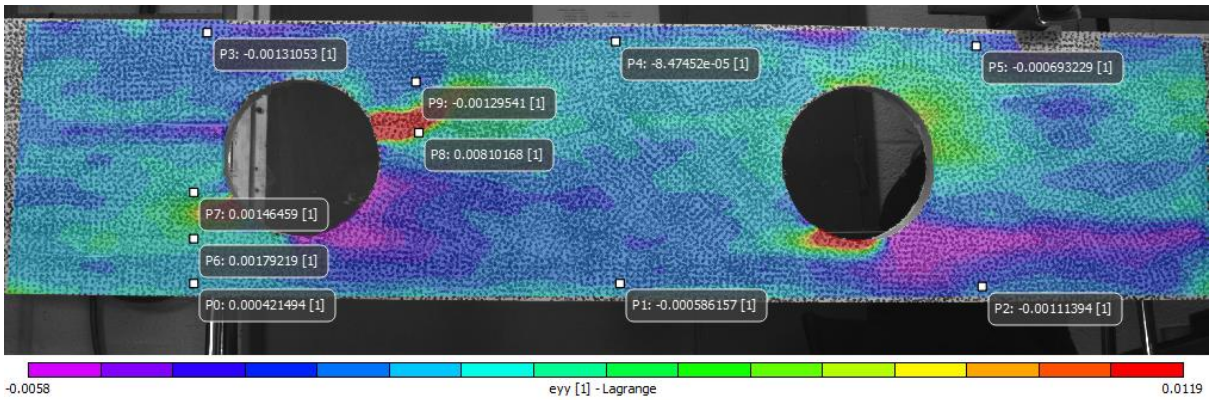

Figure 7.3: Contour and points marked for data extraction of strain (ε_{xx} P0-P5, and ε_{yy} P6-P9) on specimen A1. Results of these are seen in Figure 7.4(a-b). The legend explains the contour colors, where negative and positive indicate compression and tension.

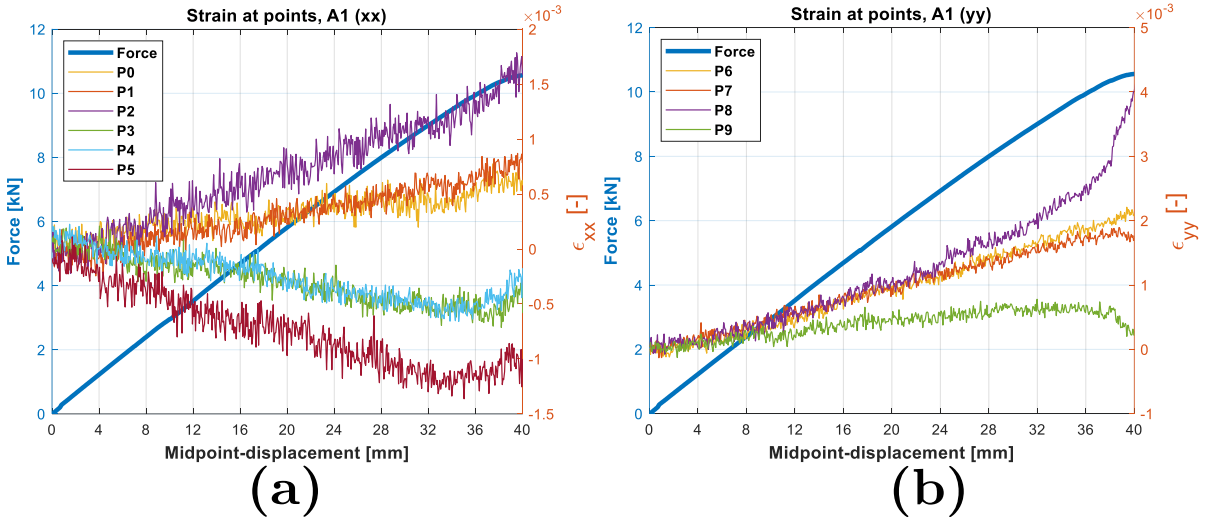

Figure 7.4: (a) Strain perpendicular to the grain ε_{yy} at four high peak points can be seen on the right y-axis. (b) Strain along the beam length on the right y-axis. The blue line refers to force/displacement until 40 mm. The location of points P0-P9 is shown in Figure 7.3.

The same process is repeated for the other unreinforced specimen, A2, where the crack evolution and force-displacement are shown in Figure 7.5 coupled with Figure 7.6 to illustrate the crack occurrences. Data after 40 mm displacement is also disregarded for this case for further analysis.

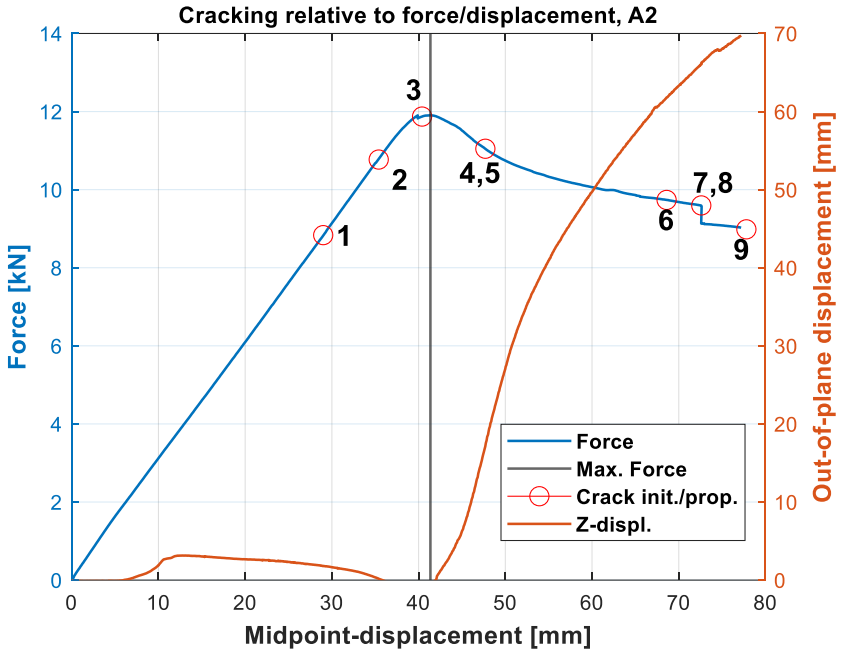

Figure 7.5: Crack evolution relative to force and displacement of specimen A2.

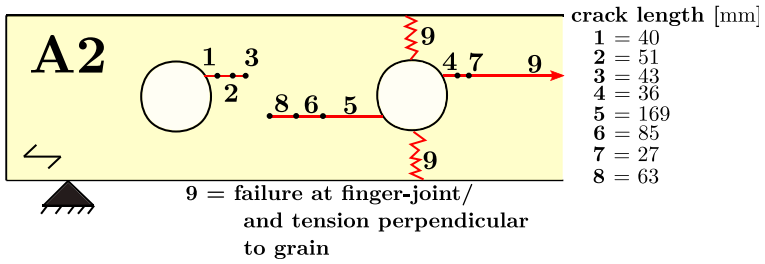

Figure 7.6: Sketch of the crack evolution of specimen A2. Crack length increments are shown on the right.

Similarly, P8 on specimen A2 (Figure 7.7), on the upper right side of the left hole, is registered as the highest strain area, which is the start of crack occurrence. No cracks were detected at the bottom-left side of the hole closest to the support, even though this was the second-highest strain perpendicular to the grain (Figure 7.8). The failure mode resulted in a sudden finger-joint failure combined with tension cracks perpendicular to the grain, as illustrated in Figure 7.6.

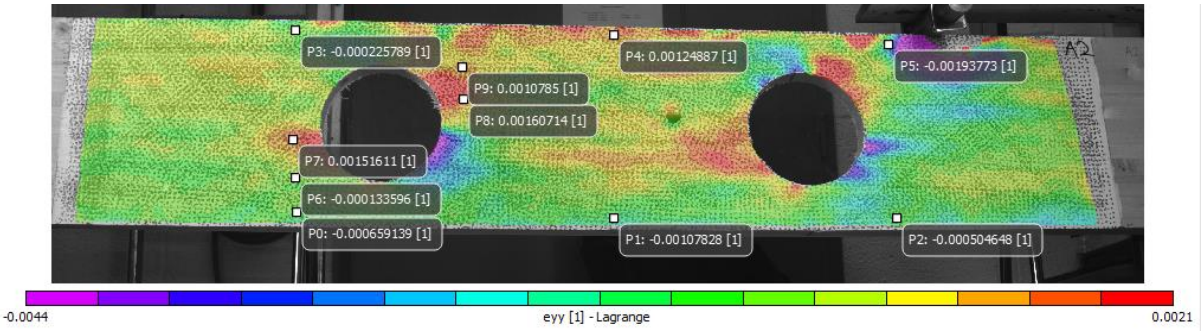

Figure 7.7: Contour and points marked for data extraction of strain (ε_{xx} P0-P5, and ε_{yy} P6-P9) on specimen A2. Results of these are seen in Figure 7.8(a-b).

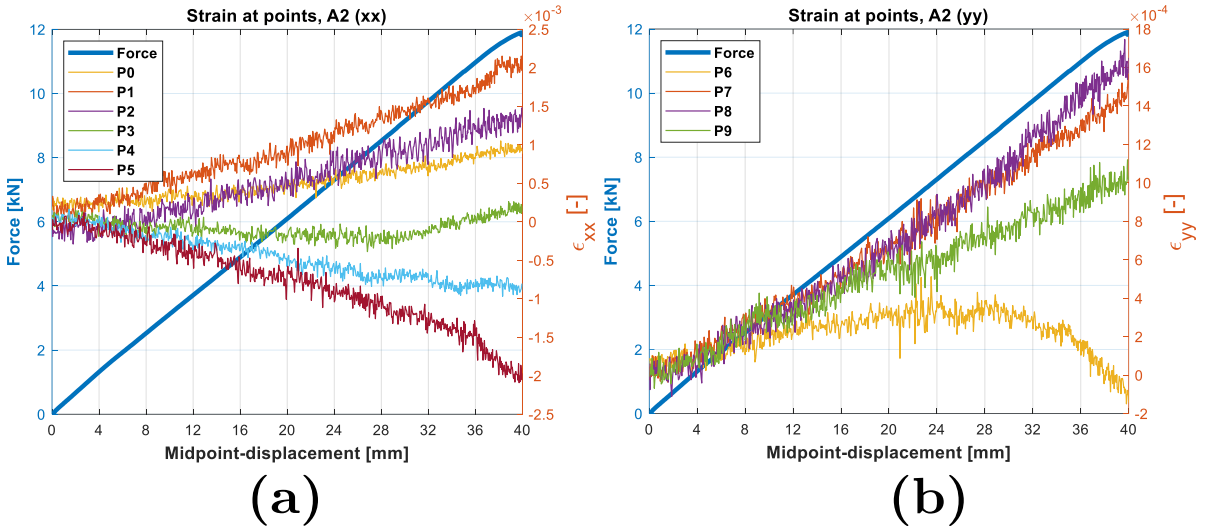

Figure 7.8: (a) Strain perpendicular to the grain ε_{yy} at four high peak points on the right y-axis. (b) Strain along the beam length on the right y-axis. Refer to Figure 7.3 for the placement of points labeled in the legends.

7.1.2 Reinforced beams

Two beams with glued-on plane plywood reinforcement were also tested, which did not experience any cracks in the hole areas. The same problem was encountered with displacement out of the plane, resulting in a decrease of force after maximum load. In addition, the beams experienced tension failure due to bending at the mid-span. Again, the strain behavior was analyzed in the DIC post-processing; however, there was no significant strain at the hole vicinity (Figure 12.8, Appendix D). The most prominent peak strain was identified at the transition between unreinforced and plate area, yet no cracks at these points were seen visually nor registered by ACDM. The main reason for these two experiments was to assess if the beams would retain the failure mode and strength as if the beams were intact without any holes. The first argument can be confirmed from the experiments; however, the second cannot because of lateral buckling.

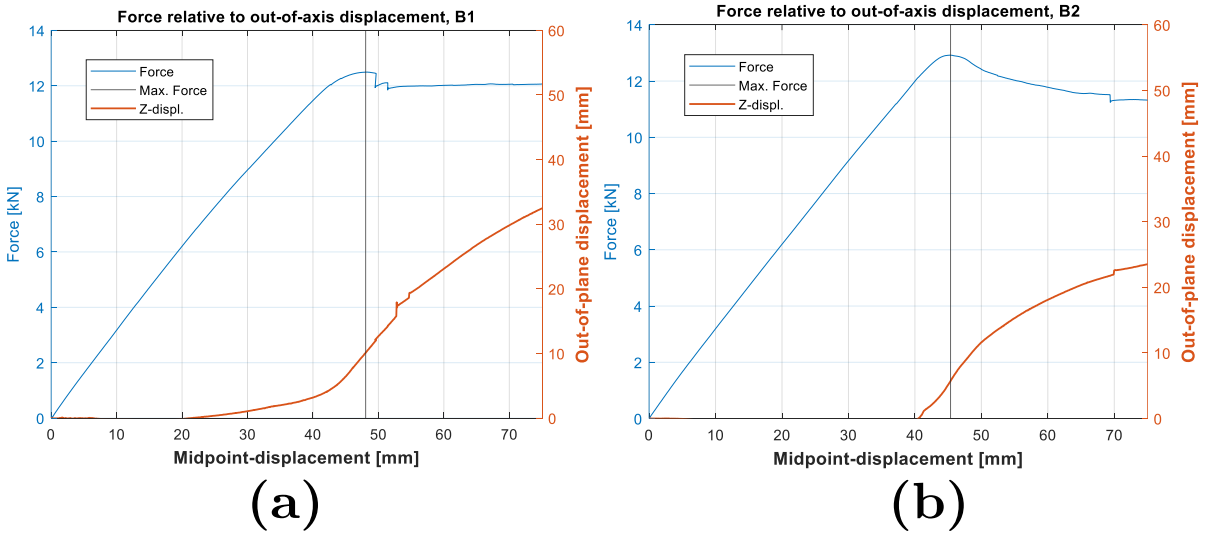

Figure 7.9: Force-displacement relation of (a) B1, and (b) B2.

7.1.3 Experiment summary

All load-displacement and crack initiation results are summarized in Table 7.1 to illustrate the differences. Crack initiation shows that the reinforced beams did not experience cracking in the DIC-recorded area. A1 had a quicker initiation than A2.

Table 7.1: Load, displacement, and first crack occurrence of all four experiments.

Specimen	Maximum load [kN]	First crack initiation [kN]	Displacement [mm] (at max. load)
A1	10,6	5,1	40,1
A2	11,9	8,8	41,3
B1	12,5	-	48,0
B2	12,9	-	45,3

7.2 Finite element elastic analyses

Elastic analyses were conducted preliminary to applying the cohesive layers to determine material properties for the individual parts applied to the final model. Additional results were extracted using a FE beam model with one hole to determine normalized stress relative to the angle at the hole.

7.2.1 Elastic material parameter sensitivity analysis

A sensitivity analysis was conducted to find the best fitting moduli of elasticity parallel to the fibers along beam length, distinguishing between the middle and outer lamellae of the glulam beam concerning its global parameters (method described in section 6.2.3). These values are then applied to the FE-model accordingly. The plot in Figure 7.10 shows the relation between the top/bottom and middle lamellae. Additionally, shear moduli are shown with colors, where the green color is aligned on the best fitting plane. The material parameters used further in the FE-model are listed in Table 7.2.

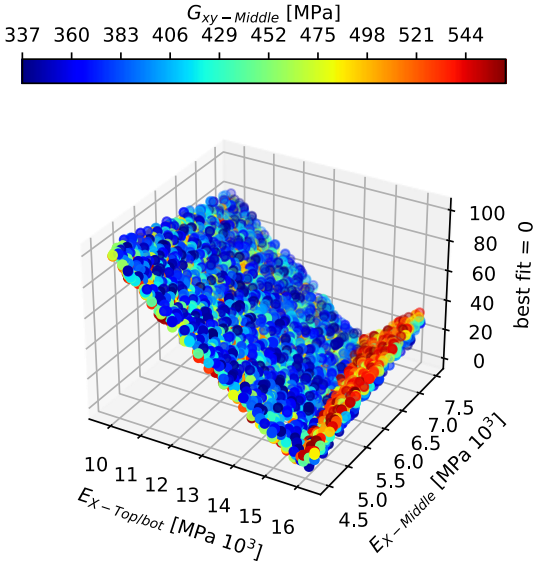

Figure 7.10: Four-dimensional sensitivity plot to determine material parameters.

Table 7.2 Elastic material properties used in the cohesive FE-model. (See section 3.2.1 for an explanation of these parameters)

	E_x [MPa]	E_{transv} [MPa]	G_{xy} [MPa]	G_{xz} [MPa]	G_{yz} [MPa]	v_{xy} [–]	v_{xz} [–]	v_{yz} [–]
Ref.	Sens. An.	Eq. (3.7)	Sens. An.	Eq. (3.8)	Eq. (3.8)	[113]	[113]	[113]
Middle lamellas	7 000	233	440	440	38	0,02	0,02	0,3
Top/bot. lamellas	13 000	433	810	810	81	0,02	0,02	0,3

7.2.2 The inclination of stress distribution in the hole vicinity

Further elastic FE-analyses were done to estimate the stress behavior in the hole vicinity, which is shown in Figure 7.11 (method explained in section 0). The graph shows the inclination of where the current peak σ_{yy} is located (right y-axis, red line) relative to the hole location along the beam length. The maximum stress inclination at the hole vicinity is between 40 and 50° until the first point load, which shifts to around 30° between the two load points. Note that stress is the maximum absolute value, which can either be tension or compression ($\sigma_{t,90}$ or $\sigma_{c,90}$). A normalized stress plot is also demonstrated (on the left y-axis with a blue line) to indicate relative stress at any given point along the beam length. Peak normalized σ_{yy} occurs before the load point, due to a combination of moment and shear. Bending moment is present alone past the load point, hence why the normalized stress curve has a steep drop and then stabilizes at ≈ 30°.

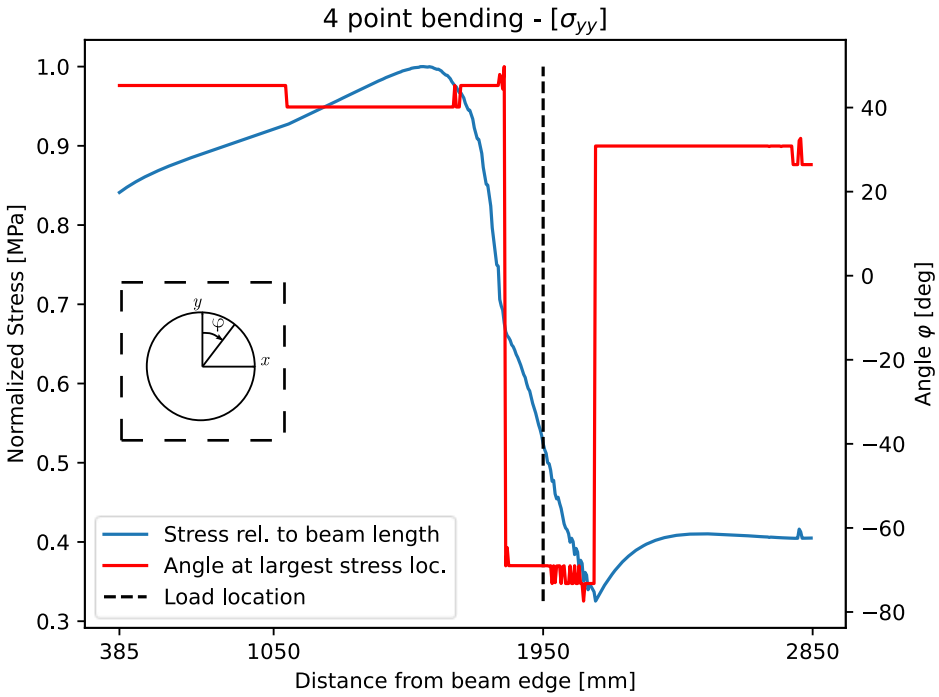

Figure 7.11: Normalized stress (blue line, left y-axis) and angle (red line, right y-axis) relative to the distance between beam edge and hole center, using a four-point bending setup.

A similar graph is shown in Figure 7.12, with an evenly distributed load every 900 mm along the beam, starting at 150 mm from the end, above the support. The maximum absolute stress σ_{yy}, at a specific angle (red line, right y-axis), in addition to the normalized stress along beam length (blue line, left y-axis) are shown. Here, the angle of the largest tensile stress is reduced by approximately 4° as the hole placement along the beam reaches a new load, although somewhat unpredictable right below the loads.

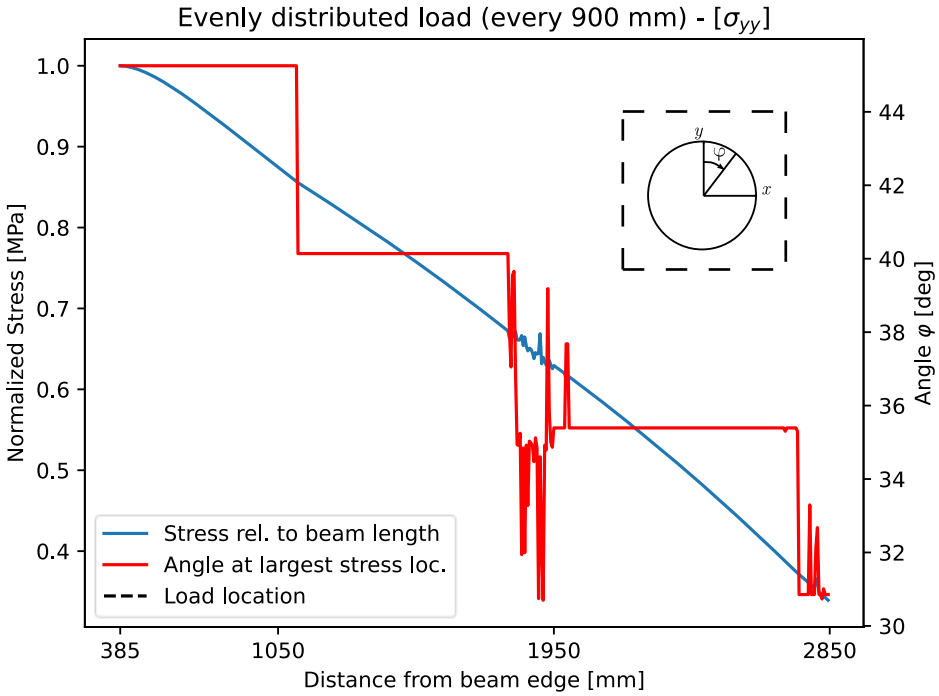

Figure 7.12: Normalized stress/angle relative to the distance between beam edge and hole center, with evenly distributed load every 900 mm.

7.3 Results of the cohesive FE-model

Figure 7.13 presents the results of the FE-model (see section 6.2 for methodology description) compared with both unreinforced experiments, along with their relative crack progression and capacity. Lines represent force-displacement (left y-axis), and dots and dash plotlines represent crack lengths relative to displacement (right y-axis) of the upper-right (u-r) and bottom-left (b-l) planes, respectively. All crack length plots refer to the first (left-side) hole. Colors indicate individual experiment or FE-model, where; A1 is green, A2 is red, and FE-result is blue. Additionally, the chart is marked with a black vertical line at the point where out-of-plane displacement began. Finally, the mean maximum force/displacement of experiments (n = 10) conducted by The Norwegian Institute of Wood Technology (Appendix A) is displayed as a purple star to demonstrate where ultimate failure was likely to happen without rotation issues. Crack evolutions are listed in steps in Appendix E. Additionally, a contour of the FE-model is shown (Figure 7.14) in a cracked state (see previous steps in Appendix F).

The two reaction forces are added and multiplied by two because Z-symmetry was implemented at half of the depth in the model. Figure 7.13 shows that the FE-modelled beam (27 kN) has around double the capacity compared to experiments conducted in this project (11-12 kN) and by NIWT

(14 kN). Additionally, crack initiation in the FE-model appears significantly later, at 72 mm displacement, compared to 17 and 28 mm. The line slope is in correspondence with the experiments. Refinement of the cohesive layer properties is necessary to match the maximum force and crack initiation.

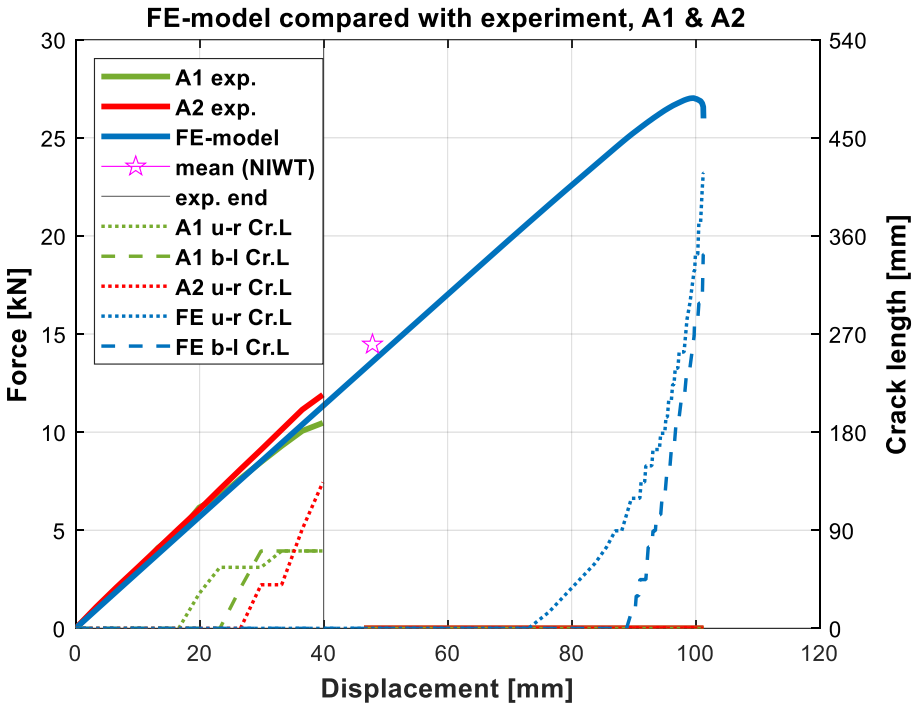

Figure 7.13: Finite element-model results compared with unreinforced experiments, A1 and A2.

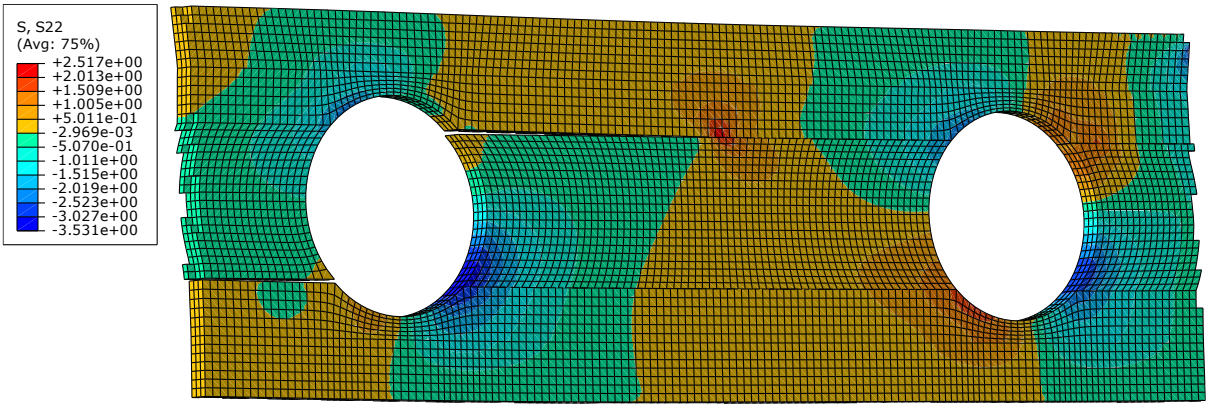

Figure 7.14: Increment 300 (Convergence) of the FE-model. Red indicates tension and blue compression.

7.4 FE-model updating procedure

This section presents a strategy to correct the FE-model based on the crack length and strain fields extracted from DIC. First, ten displacement points were defined where the desired data was extracted from the FE-model, ranging between 4-40 mm displacement. A history output of strain was then obtained at the related coordinates corresponding to the ten points in Figure 7.3 and Figure 7.7. Finally, crack initiation and propagation were calculated in the model by identifying the node IDs

associated with the cohesive layer. The ABAQUS parameter BDSTAT returns the damage condition, a value between 0-1 indicating when cracking starts.

An optimization algorithm can adjust model parameters based on the current iteration error. The SciPy toolkit Differential Evolution (DE) is suggested to tune the model parameters based on Python's programming language. DE is a stochastic population-based method that automatically searches for a solution through large data areas by mutating the search parameters. When the script detects improvements, they are then used as new parameters in the FE-model; if not, then they are disregarded, and the parameters change once again until the best match is identified [117, 118, 119]. A function (7.1) determines the error between experimental and numerical parameters, which calculates each trial of cohesive properties within the chosen boundaries:

$$C = \sum_{i=1}^{M} \left[\sum_{j=1}^{N} \left(\frac{\varepsilon_{11,ij}^{exp} - \varepsilon_{11,ij}^{num}}{\varepsilon_{11,ij}^{exp}} \right)^2 + \sum_{k=1}^{O} \left(\frac{\varepsilon_{22,ik}^{exp} - \varepsilon_{22,ik}^{num}}{\varepsilon_{22,ik}^{exp}} \right)^2 + \sum_{l=1}^{P} \left(\frac{|a_{il}^{exp} - a_{il}^{num}|}{a_{il}^{exp}} \right)^2 \right] \quad (7.1)$$

Where the apex $(*)^{exp}$ is an experimentally (DIC) calculated variable, $(*)^{num}$ is a numerically calculated variable from the FE-model, ε_{11} and ε_{22} are the strain parallel and perpendicular to the grain, and a is the crack length measured by ACDM, which is compared to the calculated distance of damaged node coordinates in the FE-model (*BDSTAT*). M describes the number of steps $\{i = 1, 2 \dots, 10\}$ where each step indicates 4 mm displacement increments, *N* is the number of strain points parallel to grain measured by DIC $\{j = 1,2 \dots, 6\}$ and O perpendicular to grain $\{k = 1, 2 \ \dots, 4\}$. Finally, P is the number of crack planes $\{l = 1, 2\}$. The cohesive parameters suggested to change are the normal and shear stress required to initiate a crack (σ_{ini} and τ_{ini}). All the experimentally measured inputs to the above formula are listed in Appendix E.

Given the time-consuming process of non-linear cohesive FEA, combined with the DE-method, the model-updating and validation of this method are purposed for future work.

8 Discussion

Experiments were studied using Digital Image Correlation-instrumentation in a four-point bending test setup on four beams. Two of the beams were reinforced with plywood glued at the hole vicinity. All specimens had two adjacent holes with a 0,57 h_d/h ratio, with the first being 1000 mm from the support to the center and the next at 1600 mm, which is 200 mm left from the first load. The strain concentrations were directly extracted from the post-processing software VIC-3D, allowing comprehension of the consequences of holes in a loaded beam. Additionally, the crack length was calculated with ACDM (MATLAB extension) to interpret the DIC results, then analyzed relative to the global displacement.

8.1 Evaluation of experimental setup, instrumentation, and post-processing

The experiments underwent lateral-torsional buckling at approximately 40 mm displacement during loading, mainly due to insufficient lateral restraints. Therefore, results after 40 mm mid-point displacement (bending) were disregarded because this presented multiple uncertainties. A preliminary test on a 48x198x6000 mm sawn timber specimen without holes did not experience this issue. This leads to the argument that other factors may have contributed to the lateral buckling, e.g., thin, tall, and heterogeneous cross-section, long span, non-linear geometry (holes), and finger-joints at the load. This problem could be reduced significantly in future experiments by utilizing a restraint at every meter along the beam. However, it might be challenging to eliminate twisting while retaining a friction-free constraint as the standard testing methods require.
The concrete support base was a solid solution, as they did not move and tolerated the load. During the laboratory tests, minor crushing of wood fibers was observed at the cylindrical steel support and loading points; this could be diminished by providing a larger contact area in future experiments. The author believes the maximum limit specified in the standard (EN 408) should be used, with half beam depth (18 mm in this case) and a thin layer of rubber between a plate and rounded edges to minimize fiber-crushing.

Securing the transducer with duct tape showed to be adequate, although it is uncertain whether this caused any minor irregularities. The linearity of the readings indicates that duct tape was sufficient. Still, a smaller piece of equipment placed underneath would have been more efficient because it would not be necessary to reattach it between every experiment.

The moisture content of all specimens was within a reasonable range of optimal test conditions (11-12%), given that the measurements were from a pin-less instrument that deviates from EN 13183-2.

DIC instrumentation met accuracy expectations, although the setup and post-processing were quite complex and time-consuming. Vertical camera alignment was used due to the broad field of view, and it met the expectations for the experiments. The speckle pattern and application were reasonable because they provided minimal grey areas with the recommended subset size. An initial attempt with a step size of 20 showed missing parts near the holes. A step size of 10 provided good accuracy within a reasonable timeframe of 13 hours per experiment.

In the absence of a better verification method, visual and manual measurements were performed on beam A1 to validate a few control points to compare with ACDM with different threshold settings. The settings were set to a 5 m/mm threshold, which deviates from the recommended settings; however, this gave the best correlation to the measurements. Crooked lines showed to be a limitation of the

software extension. Length of cracks was calculated diagonally, with no regard to jagged lines, which probably had a minor effect.

8.2 Analysis of experimental results

For both unreinforced beams (7.1.1), the most prominent strain concentrations were observed at the first hole, specifically at the upper-right side, which indicates that the shear force contribution has had a considerable effect on that specific hole. Initial cracking occurred at 17 and 28mm mid-span displacement for specimens A1 and A2. A limitation of the DIC setup is that the two cameras only capture one side of the beam; thus, one side is undocumented. The early crack initiation of A1 is likely due to the wane edge flaw, as seen in Figure 5.3, although this cannot be statistically confirmed. The ultimate failure happened at the second hole (after twisting), where a long crack propagated between the holes. In addition, A2 experienced a very brittle finger-joint failure, although the author believes this was influenced by lateral buckling, which caused tearing (fracture mode III). Nevertheless, it still indicates that finger-joint placement is not optimal, and an ideal placement would be on the opposite side of the beam. The low quality in the mid-section presents another uncertainty, emphasizing the need to do more tests. It would be more consistent in load-bearing joints to use high-grade timber with greater homogeneity or to ensure that flaws are not present in the tension zone, especially when fracture mechanics are present. Despite this, it is advantageous to evaluate worst-case scenarios in laboratory testing to ensure safety in these situations. Manufacturers may not consider the consequences of finger-joint placements and other imperfections in critical areas.

The two reinforced beams (7.1.2) did not experience any cracks in the hole area. Instead, tensile bending failure was detected at the mid-span, suggesting that plywood reinforcement can prevent stress concentrations and premature failure for beams with two large holes. The DIC analysis further confirmed this due to minimal strain values at the hole vicinity. The literature review uncovered a gap in reinforced glulam beam experiments with holes larger than 0,4 h_d/h; however, more extensive statistical support is necessary without the influence of lateral buckling to confirm if the upcoming Eurocode 5 section is too conservative regarding hole size.

8.3 Analysis of numerical results and methods

An optimization analysis initially estimated the moduli of elasticity and rigidity (7.2.1), which was based on known parameters of the entire beam (Gl24c) and the outer lamellae stiffness (C30). Although experimentally determined values give the most accurate result, estimating these values based on the best fit from the analyses is considered a good alternative solution by the author.

Further FE analyses were simulated with many iterations, and for that reason, the mesh type (C3D8R) and size (18mm global) were chosen to reduce computation time. Various mesh types and sizes have not been compared to verify the effects this could have on the results. Previous research indicated that selecting a higher viscosity parameter is not ideal; this was then chosen to a low value of 0,0001.

FE-analyses (7.2.2) with one hole uncovered that the stress distribution is dependent on hole location relative to the support and load. In most areas, the maximum absolute stress perpendicular to the grain σ_{yy} was found to be between approximately 45° and 30° degrees, except near the load. Thus deviating from the literature (Chapter 3.4) near loads, where crack planes were discovered at 60° or 300°. Only σ_{yy} was considered in this analysis, and σ_{xx} will have a greater contribution near the mid-

span which explains this deviation. When the hole is close to or beneath the load, the maximum stress location is unstable and challenging to accurately predict when stress contributions change from shear and bending to pure bending. Keep in mind that this is generated from a model and not validated by laboratory testing. In addition, glue lines are not considered in the model and have an unknown effect.

Numerical crack length data and force-displacement relation (7.3) were compared with this thesis's experimental results and previous findings. The force-displacement slope line of the FE-model correlated to the experiments, which suggests that elastic parameters agree with the glulam beams. Even with limitations of transversal isotropy and numerically generated values. The numerical results greatly overestimated the force to reach ultimate failure and the initiation of cracks, which signifies that the cohesive material parameters are not in accordance with reality, which is expected when values are found from the literature of different material strengths. The placement of the cohesive layer does not entirely represent the actual crack propagation, as some cracks tend to extend away from the horizontal plane. Moreover, ultimate failure at the second hole happened at a lower position in the cohesive zone. The bilinear traction-separation assumption may also explain why the cracks are rapidly propagating.

Experimentally determined fracture energy will most likely provide the best fitting model parameters, but these test methods require special equipment and are not included in the scope of this thesis. The author believes that the stress needed to initiate cracks (σ_{ini}, τ_{ini}) needs to be lowered to reflect the actual crack-timing better. This led the author to create an expression (7.1) which is believed to describe the error realistically based on strain changes and crack evolution to adjust the cohesive parameters. It can be argued that using ultimate force as the variable can allow for quicker convergence. Still, it is the author's opinion that this would not correctly represent the overall progression of the material behavior compared to DIC results.

9 Conclusion

Cutting holes in load-bearing timber beams cause failure due to concentrations of tension perpendicular to the grain, which has been addressed in this thesis. Utilizing modern methods to analyze this type of damage or failure and other topics outside of building codes can be advantageous in providing knowledge for practitioners and motivating further research.

The research questions created the basis for the theme of this project, which is repeated and answered below:

- **How are simply supported glulam beams affected by large holes when subjected to bending and shear, with and without reinforcement?**

A standard four-point bending was used to conduct experiments on two unreinforced glulam beams with two consecutive holes, each constituting 57% of beam height in diameter. Crack initiation began at 45° of the closest hole to the support, but the next crack plane differed between the experiments. A detailed analysis utilizing two Digital Image Correlation-cameras uncovered that tensile stress perpendicular to the grain was the cause of the crack occurrence, which is the weakest strength direction of timber.

The same setup was used for two reinforced beams with equivalent dimensions and hole sizes. The reinforcement successfully prevented tensile stress concentrations at the holes, which resulted in no cracks being detected in this area, and strain levels were found minimal in the post-processing of DIC. The beams experienced failure at mid-span in the tensile bending area.

- **How can cracks be effectively detected and measured during experiments and used in an FE-model?**

A method to use the high-resolution images from DIC, called “Automatic Crack Detection and Measurement (ACDM),” was utilized on the gathered data of the four experiments after extracting it to a MATLAB format. This tool effectively detected cracks in the experiments, and their length was calculated through the software, with some limitations. Nevertheless, the data indicated to be in unity with the experimental findings, given a selected strain threshold of 5 mm/m. A surface-based cohesive zone FE-model (SCZM) was created in ABAQUS to analyze cracks and capacity numerically, with equal hole placements and dimensions in resemblance to the beam experiments. No existing methods were identified to correct an FE-model relative to DIC results directly. Instead, a technique to extract specific points of cracks along the cohesive layer in ABAQUS was devised by identifying the parameter that causes separation (*BDSTAT*). These points were then manually compared to the equivalent DIC coordinates.

- **How does numerical data from finite element analyses correlate to experimental results?**

The numerical and experimental results were compared with others findings of equivalent beam modifications. Elastic parameters of the model were partly determined by actual test values combined with numerically optimized values to fill in missing parameter gaps, which resulted in a great match between the force-displacement curve slopes.

Cohesive layer parameters were found in the literature and applied to the FE-model, but they did not correlate with experimental findings of crack initiation and ultimate failure load. Consequently, the FE-model overestimated the capacity by approximately twofold compared to experiments, and cracks were initiated at a later stage.

- **How can experimental results from DIC be utilized to update the finite element model?**

Adjusting the maximum nominal stress required to initiate cracks of the cohesive layer was necessary due to the inconsistencies between the model and experiments. Hence, a method to optimize these parameters was presented based on the high-quality images from DIC.

The suggested procedure involves a stochastic optimization algorithm using Python script, which identifies the degree of correlation between chosen data from the model and experiments and replaces model parameters until an improvement is made, which will continue until the best fit is found. An error function was defined based on three different measurements from DIC: four high-strain points perpendicular to the grain where cracks initiate, and six points of strain along the grain, in addition, to crack length. The author believes that the cohesive parameters, σ_{ini} and τ_{ini}, should be corrected by the optimization to create a more precise correlation between the FE-model and experiments. However, this hypothesis has not been validated within the framework of this study.

To summarize, a novel combination of existing, although advanced methods were utilized in this thesis to gather information on crack and strain behavior in timber beams, which can be directly used to update an equivalent FE-model with cohesive layers by Python scripts. Experiments proved that unreinforced glulam beams with large holes are subject to stress concentrations, which causes cracks and premature failure to occur, although this can be prevented by applying plywood with adhesives to the beam faces. This thesis does not provide enough statistical material and control group (beam without holes) to conclude that it retains its strength as if there were no holes. However, it raises the question that research until now has not covered large, reinforced holes. The results of a non-linear finite model with cohesive layers emphasized the importance of acquiring realistic material parameters. The model proved to overestimate the strength given the literature-based parameters, which was the motivation to find a method to tune the model automatically.

Modeling in ABAQUS by Python code was initially very time-consuming. Still, it showed to be highly advantageous for creating an automated process since it allowed to iterate thousands of analyses with small differences in dimensions and material parameters. Dual-camera DIC proved to be excellent for analyzing strain at specific points and measuring any unwanted issues, such as lateral buckling. The post-processing of DIC did not provide any means to detect or measure cracks itself, but the ACDM-method showed to be an efficient extension for this purpose. However, it requires validation to assure correct threshold settings. Moreover, extracting strain and crack data from the FE-model showed to be more challenging than initially expected, as sets of specific node IDs must be defined, which required significant manual labor.

10 Recommendations

During the work of this thesis, some questions emerged that were outside the framework, besides finding some undiscovered areas in current research.

- **Reinforced glulam beams with large holes**

A research gap was found in reinforced holes larger than 40 % of the beam height. The author urges future research to follow this up with experiments, especially with a new Eurocode 5 within reach and improving timber's competitiveness.

- **Validation of the proposed model-updating method**

The author believes that DIC data can be used to update a model based on the stochastic optimization procedure. It is highly recommended that this method is validated in future work.

- **Experimental determination of material fracture parameters**

The reliability of FE-models is imperative for practitioners; therefore, the author recommends further studies to determine fracture parameters for different materials.

- **Utilizing DIC data to an FE-model and creating a common format**

Direct use of DIC strain-field in combination with crack length to update an FE-model seems unexplored; thus, the author is hopeful that this thesis will be a foundation for future work on this topic. Furthermore, the author is optimistic about creating efficient, reliable models that reflect realistic situations based on DIC experiments. Locating and extracting data from specific nodes in the FE-model to correlate with DIC proved to be complicated and tedious during the work with this thesis. The author is confident that additional research and software development can lead to successful collaboration between FE-software and DIC-instrumentation and lead to automatization. Consequently, this can advance new ways of analyzing practical situations of structures based on acquired knowledge from experiments.

- **Applying ACDM in more case studies of different materials**

Supplementary experiments of cracks utilizing ACDM are recommended to establish more knowledge of the consequence regarding the chosen threshold and a validation procedure to confirm its accuracy.

11 References

[1] M. Frese and H. Blass, 'Failure Analysis on Timber Structures in Germany Failure Analysis on Timber Structures in Germany a Contribution to Cost Action E55', 2007. https://www.semanticscholar.org/paper/Failure-Analysis-on-Timber-Structures-in-Germany-on-Frese/e65971bd4721684f39fb9c8b90d0c538cd333d15 (accessed Mar. 26, 2022).

[2] S. Franke, B. Franke, and A. M. Harte, 'Failure modes and reinforcement techniques for timber beams – State of the art', *Construction and Building Materials*, Oct. 2015, doi: 10.1016/j.conbuildmat.2015.06.021.

[3] P. Dietsch, A. Gamper, M. Merk, and S. Winter, 'Monitoring building climate and timber moisture gradient in large-span timber structures', *Journal of Civil Structural Health Monitoring*, Jul. 2014, doi: 10.1007/s13349-014-0083-6.

[4] J. Schmidt and M. Kaliske, 'Models for numerical failure analysis of wooden structures', *Engineering Structures*, Feb. 2009, doi: 10.1016/j.engstruct.2008.11.001.

[5] M. Ardalany, 'Analysis and design of laminated veneer lumber beams with holes', Ph.D, University of Canterbury, Department of Civil and Natural Resources Engineering, 2012.

[6] P. W. Harper and S. R. Hallett, 'Cohesive zone length in numerical simulations of composite delamination', *Engineering Fracture Mechanics*, Nov. 2008, doi: 10.1016/j.engfracmech.2008.06.004.

[7] J.-L. Coureau, S. Morel, and N. Dourado, 'Cohesive zone model and quasibrittle failure of wood: A new light on the adapted specimen geometries for fracture tests', *Engineering Fracture Mechanics*, Sep. 2013, doi: 10.1016/j.engfracmech.2013.02.025.

[8] 'Eurocode 5: Design of timber structures - Part 1-1: Common rules and rules for buildings', EN 1995-1-1.

[9] S. Aicher and L. Höfflin, 'Fracture behaviour and design of glulam beams with round holes', *10th World Conference on Timber Engineering 2008*, vol. 1, pp. 132–139, Jan. 2008.

[10] H. Danielsson, 'Perpendicular to grain fracture analysis of wooden structural elements - Models and applications', Ph.D Dissertation, Lund University, 2013. Accessed: Mar. 28, 2022. [Online]. Available: http://lup.lub.lu.se/record/3633863

[11] H. Danielsson, 'The strength of glulam beams with holes. A survey of tests and calculation methods', Lund University, Sweden, 2006.

[12] P. Dietsch, 'Reinforcement of timber structures - a new section for Eurocode 5', presented at the WCTE World conference on Timber Engineering 2016, Vienna, Austria, Aug. 2016.

[13] 'Eurocode 5: Bemessung und Konstruktion von Holzbauten - Allgemeine Regeln und Regeln fur den Hochbau (German annex to Eurocode 5)', DIN EN 1995-1-1/NA, 2012. [Online]. Available: https://www.beuth.de/de/norm/din-en-1995-1-1/134637145

[14] J. Fröbel, *Limträhandbok - Projektering av limträkonstruktioner. Part 2*. 2016. [Online]. Available: https://www.svenskttra.se/publikationer-start/publikationer/limtrahandbok/

[15] Y. Wang, 'Earth science research contributing to sustainability of our home planet', *All Earth*, vol. 34, 2022, doi: 10.1080/27669645.2022.2056220.

[16] Y. Malhi *et al.*, 'Climate change and ecosystems: threats, opportunities and solutions', *Philosophical Transactions of the Royal Society B: Biological Sciences*, Mar. 2020, doi: 10.1098/rstb.2019.0104.

[17] Regjeringen (The Norwegian Government), 'A European Green Deal. Norwegian perspectives and contributions', Oslo, 2021. [Online]. Available: https://www.regjeringen.no/contentassets/38453d5f5f5d42779aaa3059b200a25f/a-european-green-deal-norwegian-perspectives-and-contributions-20.04.2021.pdf

[18] United Nations, 'Sustainable consumption and production', *United Nations Sustainable Development*. https://www.un.org/sustainabledevelopment/sustainable-consumption-production/ (accessed Mar. 22, 2022).

[19] S. Bouckaert and al. et., 'Net Zero by 2050 - A Roadmap for the Global Energy Sector', International Energy Agency, IEA, 2021.

[20] 'Goal 15 | Department of Economic and Social Affairs'. https://sdgs.un.org/goals/goal15 (accessed Mar. 22, 2022).

[21] Forest Stewardship Council, 'Global Strategy (2021-2026)', 2020. [Online]. Available: https://fsc.org/en/newsfeed/fsc-global-strategy-2021-2026-demonstrating-the-value-and-benefits-of-forest-stewardship

[22] United Nations, 'The Global Forest Goals Report 2021', 2021. [Online]. Available: https://www.un.org/en/desa/global-forest-goals-report-2021

[23] European Commission, 'Proposal for a regulation on deforestation', Nov. 2021. https://ec.europa.eu/environment/publications/proposal-regulation-deforestation-free-products_en (accessed Mar. 22, 2022).

[24] IPCC, 'Special Report on Climate Change and Land'. https://www.ipcc.ch/srccl/ (accessed Mar. 22, 2022).

[25] G. R. van der Werf *et al.*, 'CO2 emissions from forest loss', *Nature Geosci*, Art. no. 11, Nov. 2009, doi: 10.1038/ngeo671.

[26] FAO, *Global Forest Resources Assessment 2020: Main report*. Rome, Italy: FAO, 2020. doi: 10.4060/ca9825en.

[27] D. Schimel, B. B. Stephens, and J. B. Fisher, 'Effect of increasing CO2 on the terrestrial carbon cycle', *Proceedings of the National Academy of Sciences*, Jan. 2015, doi: 10.1073/pnas.1407302112.

[28] FOREST EUROPE, 'State of Europe's Forests 2020', 2020. [Online]. Available: https://foresteurope.org/publications/

[29] 'The National Forest Inventory, 1990-2020'. Statistisk Sentralbyrå (Statistics Norway), 2021. [Online]. Available: https://www.ssb.no/en/statbank/table/06289/tableViewLayout1/

[30] 'Forestry', *Government.no*, Dec. 03, 2014. https://www.regjeringen.no/en/topics/food-fisheries-and-agriculture/skogbruk/innsikt/skogbruk/id2009516/ (accessed Mar. 22, 2022).

[31] 'Tracking Industry 2021 – Analysis', *IEA*. https://www.iea.org/reports/tracking-industry-2021 (accessed Mar. 22, 2022).

[32] Energy Transitions Commission, 'Mission Possible - Reaching Net-zero carbon emissions from harder-to-abate sectors by mid-century', Nov. 2018. [Online]. Available: https://www.energy-transitions.org/wp-content/uploads/2020/08/ETC_MissionPossible_FullReport.pdf

[33] R. Bergman, M. Puettmann, A. Taylor, and K. E. Skog, 'The Carbon Impacts of Wood Products', *Forest Prod. J.*, 2014, doi: 10.13073/FPJ-D-14-00047.

[34] P. W. Ellis *et al.*, 'Reduced-impact logging for climate change mitigation (RIL-C) can halve selective logging emissions from tropical forests', *Forest Ecology and Management*, Apr. 2019, doi: 10.1016/j.foreco.2019.02.004.

[35] A. M *et al.*, 'Carbon Emission Assessment From Different Logging Activities in Production Forest of Pahang, Malaysia', *Journal of Tropical Forest Science*, 2019, doi: DOI:10.26525/jtfs2019.31.3.304.

[36] R. Bergman and S. Bowe, 'Environmental impact of producing hardwood lumber using life-cycle inventory', *Wood and fiber science: journal of the Society of Wood Science and Technology*, Jul. 2008, [Online]. Available: https://www.fs.usda.gov/treesearch/pubs/31113

[37] Athena SMI, 'A Cradle-to-Gate life cycle assessment of cross-laminated timber and glued-laminated timber manufactured by structurlam', Athena Sustainable Materials Institute, 2019. [Online]. Available: https://www.structurlam.com/wp-content/uploads/2021/02/Structurlam-Life-Cycle-Assessment-Report.pdf?x71093

[38] S. Thale, 'Limsystemer for limtre og sponplater', SINTEF, 94, 2012. [Online]. Available: https://www.sintefbok.no/book/index/919/limsystemer_for_limtre_og_sponplater

[39] L. Bushi, J. Meil, and G. Finlayson, 'A cradle-to-gate life cycle assessment of North American wood product resin systems', *Athena report*, 2022, Accessed: May 09, 2022. [Online]. Available: http://www.fs.usda.gov/treesearch/pubs/64106

[40] P. Wood Building the Future, 'Wood and Climate'. http://www.wooddays.eu/en/woodclimate/ (accessed May 09, 2022).

[41] A. Hasanbeigi, 'Global Steel Industry's GHG Emissions', *Global Efficiency Intelligence*, Aug. 2021. https://www.globalefficiencyintel.com/new-blog/2021/global-steel-industrys-ghg-emissions (accessed Mar. 22, 2022).

[42] A. Hasanbeigi and C. Springer, 'How clean is the U.S. Steel industry?', Nov. 2019. [Online]. Available: https://www.globalefficiencyintel.com/new-blog/2019/12/3/new-report-how-clean-is-the-us-steel-industry

[43] W. Sun, Q. Wang, Y. Zhou, and J. Wu, 'Material and energy flows of the iron and steel industry: Status quo, challenges and perspectives', *Applied Energy*, Jun. 2020, doi: 10.1016/j.apenergy.2020.114946.

[44] F. Morris, S. Allen, and W. Hawkins, 'On the embodied carbon of structural timber versus steel, and the influence of LCA methodology', *Building and Environment*, Dec. 2021, doi: 10.1016/j.buildenv.2021.108285.

[45] Global Cement and Concrete Association, 'Global Cement and Concrete Industry Announces Roadmap To Achieve Groundbreaking "Net Zero" CO2 Emissions by 2050', *GCCA*, Mar. 22, 2022. https://gccassociation.org/news/global-cement-and-concrete-industry-announces-roadmap-to-achieve-groundbreaking-net-zero-co2-emissions-by-2050/ (accessed Mar. 22, 2022).

[46] 'Cement – Analysis', *IEA*. https://www.iea.org/reports/cement (accessed Mar. 22, 2022).

[47] P. Gursel and C. Ostertag, 'Comparative Life-Cycle Impact Assessment of Concrete Manufacturing in Singapore', *The International Journal of Life Cycle Assessment*, Feb. 2017, doi: 10.1007/s11367-016-1149-y.

[48] 'Cement: the Most Destructive Material in the World or a Driver of Progress?' https://www.renewablematter.eu/articles/article/cement-the-most-destructive-material-in-the-world-or-a-driver-of-progress (accessed Mar. 22, 2022).

[49] Y. L. Mack-Vergara and V. M. John, 'Life cycle water inventory in concrete production—A review', *Resources, Conservation and Recycling*, Jul. 2017, doi: 10.1016/j.resconrec.2017.01.004.

[50] A. B. Robertson, F. C. F. Lam, and R. J. Cole, 'A Comparative Cradle-to-Gate Life Cycle Assessment of Mid-Rise Office Building Construction Alternatives: Laminated Timber or Reinforced Concrete', *Buildings*, Sep. 2012, doi: 10.3390/buildings2030245.

[51] 'Timber structures - Glued laminated timber and glued solid timber - Requirements', EN 14080, 2013.

[52] Blaß, H J and C. Sandhaas, *Timber Engineering - Principles for Design*. 2017. [Online]. Available: https://publikationen.bibliothek.kit.edu/1000069616

[53] B. Pitzner and P. Lind, 'Gluing of Norway spruce and Scots pine with an EPI-adhesive (emulsion polymer isocyanate)', Norwegian Institute of Wood Technology, 2005. [Online]. Available: https://www.treteknisk.no/publikasjoner/rapport/60-gluing-of-norway-spruce-and-scots-pine-with-an-epi-adhesive-emulsion-polymer-isocyanate-

[54] K. Grøstad and R. Bredesen, 'EPI for Glued Laminated Timber', in *Materials and Joints in Timber Structures*, Dordrecht, 2014, pp. 355–364. doi: 10.1007/978-94-007-7811-5_32.

[55] T. Ozyhar, S. Hering, and P. Niemz, 'Viscoelastic characterization of wood: Time dependence of the orthotropic compliance in tension and compression', *Journal of Rheology*, vol. 57, no. 2, pp. 699–717, Mar. 2013, doi: 10.1122/1.4790170.

[56] D. Schoenmakers, 'Fracture and failure mechanisms in timber loaded perpendicular to the grain by mechanical connections', Ph.D, Technische Universiteit Eindhoven, 2010. doi: 10.6100/ir673053.

[57] D. Keunecke, S. Hering, and P. Niemz, 'Three-dimensional elastic behaviour of common yew and Norway spruce', *Wood Sci Technol*, Dec. 2008, doi: 10.1007/s00226-008-0192-7.

[58] I. Smith and S. Vasic, 'Fracture behaviour of softwood', *Mechanics of Materials*, vol. 35, pp. 803–815, Aug. 2003, doi: 10.1016/S0167-6636(02)00208-9.

[59] A. H. Buchanan, 'Bending Strength of Lumber', *Journal of Structural Engineering*, May 1990, doi: 10.1061/(ASCE)0733-9445(1990)116:5(1213).

[60] M. Khelifa and A. Khennane, 'Numerical Analysis of the Cutting Forces in Timber', *Journal of Engineering Mechanics*, Mar. 2014, doi: 10.1061/(ASCE)EM.1943-7889.0000671.

[61] S. Aicher, P. J. Gustafsson, P. Haller, and H. Petersson, 'Fracture Mechanics Models for Strength Analysis of Timber Beams with a Hole or a Notch - A Report of RILEM TC-133', 2002.

[62] B. Time, 'Hygroscopic Moisture Transport in Wood', Ph.D, Norwegian University of Science and Technology, NTNU, 1998.

[63] E. Frühwald, E. Serrano, T. Toratti, A. Emilsson, and S. Thelandersson, 'Design of safe timber structures - How can we learn from structural failures in concrete, steel and timber?', Lund University, Report TVBK-3053., Div. of Struct. Eng., 270, 2007.

[64] P. Dietsch, A. Gamper, S. Merk, and S. Winter, 'Building climate-long-term measurements to determine the effect on the moisture gradient in large-span timber structures', Växjö, 2012, p. CIB-W18/45-11-1.

[65] 'Structural timber - Strength classes', EN 338, 2016.

[66] 'Moisture content of a piece of sawn timber - Part 1: Determination by oven dry method', EN 13183-1, 2002.

[67] 'Moisture content of a piece of sawn timber - Part 2: Estimation by electrical resistance method', EN 13183-2, 2002.

[68] S. Aicher and L. Höfflin, 'Fracture behaviour and design of glulam beams with round holes', *10th World Conference on Timber Engineering 2008*, vol. 1, pp. 132–139, Jan. 2008.

[69] M. Danzer, P. Dietsch, and S. Winter, 'Reinforcement of round holes in glulam beams arranged eccentrically in groups', presented at the World Conference on Timber Engineering (WCTE 2016), 2016. Accessed: Mar. 25, 2022. [Online]. Available: https://mediatum.ub.tum.de/1346435

[70] S. Okamoto, N. Akiyama, Y. Araki, K. Aoki, and M. Inayama, 'Study on the strength of glued laminated timber beams with round holes: difference in structural performance between homogeneous-grade and heterogeneous-grade timber', *Journal of Wood Science*, Jan. 2021, doi: 10.1186/s10086-021-01941-3.

[71] S. Aicher and L. Höfflin, 'A contribution to the analysis of glulam beams with round holes'. Otto-Graf-Journal Vol. 11, 2000.

[72] S. Aicher, L. Höfflin, and H.-W. Reinhardt, 'Runde Durchbrüche in Biegeträgern aus Brettschichtholz – Teil 2: Tragfähigkeit und Bemessung', *Bautechnik*, vol. 84, no. 12, pp. 867–880, Dec. 2007, doi: 10.1002/bate.200710074.

[73] T. L. Anderson, *Fracture Mechanics - Fundamentals and Applications*, 3rd edition. CRC Press, 2017. [Online]. Available: https://doi.org/10.1201/9781315370293

[74] C. Rountree, R. Kalia, E. Lidorikis, A. Nakano, L. Van Brutzel, and P. Vashishta, 'Atomistic Aspects of Crack Propagation in Brittle Materials: Multimillion Atom Molecular Dynamics Simulations', *Annu. Rev. Mater. Res*, Aug. 2002, doi: 10.1146/annurev.matsci.32.111201.142017.

[75] A. A. Griffith, 'VI. The phenomena of rupture and flow in solids', *Philosophical Transactions of the Royal Society of London. Series A, Containing Papers of a Mathematical or Physical Character*, Jan. 1921, doi: 10.1098/rsta.1921.0006.

[76] E. M. Wu, 'Application of Fracture Mechanics to Anisotropic Plates', *Journal of Applied Mechanics*, Dec. 1967, doi: 10.1115/1.3607864.

[77] D. S. Dugdale, 'Yielding of steel sheets containing slits', *Journal of the Mechanics and Physics of Solids*, May 1960, doi: 10.1016/0022-5096(60)90013-2.

[78] G. I. Barenblatt, 'The Mathematical Theory of Equilibrium Cracks in Brittle Fracture', in *Advances in Applied Mechanics*, H. L. Dryden, Th. von Kármán, G. Kuerti, F. H. van den Dungen, and L. Howarth, Eds. Elsevier, 1962. doi: 10.1016/S0065-2156(08)70121-2.

[79] A. Hillerborg, M. Modéer, and P.-E. Petersson, 'Analysis of crack formation and crack growth in concrete by means of fracture mechanics and finite elements', *Cement and Concrete Research*, Nov. 1976, doi: 10.1016/0008-8846(76)90007-7.

[80] P.-J. Gustafsson, 'Fracture mechanics studies of non-yielding materials like concrete : modelling of tensile fracture and applied strength analyses', Doctoral Thesis (monograph), Division of Building Materials, LTH, Lund University, 1985.

[81] K. Ostapska and K. A. Malo, 'Calibration of a combined XFEM and mode I cohesive zone model based on DIC measurements of cracks in structural scale wood composites', *Composites Science and Technology*, Jan. 2021, doi: 10.1016/j.compscitech.2020.108503.

[82] M. Wang, X. Song, and X. Gu, 'Three-Dimensional Combined Elastic-Plastic and Damage Model for Nonlinear Analysis of Wood', *Journal of Structural Engineering*, Aug. 2018, doi: 10.1061/(ASCE)ST.1943-541X.0002098.

[83] K. Ostapska and K. A. Malo, 'Wedge splitting test of wood for fracture parameters estimation of Norway Spruce', *Engineering Fracture Mechanics*, Jun. 2020, doi: 10.1016/j.engfracmech.2020.107024.

[84] Simulia, 'Abaqus Analysis User's Manual v. 6.9-EF', 2009. http://130.149.89.49:2080/v6.9ef/books/usb/default.htm?startat=pt09ch33s01alm62.html (accessed Mar. 20, 2022).

[85] Simulia, 'Abaqus 6.14 Theory Manual', 2014. [Online]. Available: http://130.149.89.49:2080/v6.14/books/stm/default.htm

[86] S. Aicher, 'Glulam beams with internally and externally reinforced holes - tests, detailing and design', Aug. 2011. [Online]. Available: https://www.researchgate.net/publication/261878057_Glulam_beams_with_internally_and_externally_reinforced_holes_-_tests_detailing_and_design

[87] K. Hijikata, H. Idota, and N. Tsujimoto, 'Strength Estimation and Reinforcement of Glue-Laminated Timber Beams with Circular Through-Hole', presented at the WCTE 2010, 2010. doi: 10.3130/aijs.77.397.

[88] C. Tapia and S. Aicher, 'Holes in glulam-Orientation and design of internal reinforcements.', Vienna University of Technology, Austria, 2016.

[89] H. Blass and I. Bejtka, 'Reinforcements perpendicular to the grain using self-tapping screws', in Proceedings of the 8th world conference on timber engineering , 2004, vol. 1.

[90] S. Aicher and L. Höfflin, 'Glulam beams with holes reinforced by steel bars', *Intl. Council for Research and Innovation in Building and Construction, Working Commission 18-Timber Structures*, 2009.

[91] S. Aicher and C. Tapia, 'Novel internally LVL-reinforced glued laminated timber beams with large holes', *Construction and Building Materials*, Apr. 2018, doi: 10.1016/j.conbuildmat.2018.02.178.

[92] M. Lechner, P. Dietsch, and S. Winter, 'Veneer-reinforced timber – Numerical and experimental studies on a novel hybrid timber product', *Construction and Building Materials*, Sep. 2021, doi: 10.1016/j.conbuildmat.2021.123880.

[93] P. Dietsch, 'Reinforcement of Timber Structures: Standardization Towards a New Section for EC 5', in *Reinforcement of Timber Elements in Existing Structures: State-of-the-Art Report of the RILEM TC 245-RTE*, J. Branco, P. Dietsch, and T. Tannert, Eds. Cham: Springer International Publishing, 2021, pp. 99–132. doi: 10.1007/978-3-030-67794-7_6.

[94] University of South Carolina, 'Digital Image Correlation: Overview of Principles and Software. SEM 2009 Workshop'. 2009.

[95] Correlated Solutions, *VIC-3D Software Manual Version 8.4*. [Online]. Available: https://www.correlatedsolutions.com/supportcontent/VIC-3D-8-Manual.pdf

[96] N. Gehri, J. Mata-Falcón, and W. Kaufmann, 'Automated crack detection and measurement based on digital image correlation', *Construction and Building Materials*, Sep. 2020, doi: 10.1016/j.conbuildmat.2020.119383.

[97] N. Gehri, J. Mata-Falcón, and W. Kaufmann, 'Refined extraction of crack characteristics in large-scale concrete experiments based on digital image correlation', *Engineering Structures*, Jan. 2022, doi: 10.1016/j.engstruct.2021.113486.

[98] S. Bengtsson and G. Dahl, 'Inverkan av hål nära upplag på hållfastheten hos limträbalkar', Lund Tekniska Högskola, 1971.

[99] H. Kolb and P. Frech, 'Untersuchungen an durchbrochenen Bindern aus Brettschichtholz', *Holz als Roh- und Werkstoff*, Apr. 1977, doi: 10.1007/BF02625327.

[100] V. Penttala, 'Reiällinen liimapuupalkki (Glulam beams with holes)', Helsinki University of Technology, Otaniemi, Pub. 33, 1980.

[101] B. Johannesson, 'Limträbalkar med hål (Glulam beams with holes)', Chalmers University of Technology, Göteborg, Pub. S83:1, 1983.

[102] S. Hallström, 'Glass fibre reinforced holes in laminated timber beams', *Wood Sci.Technol.*, Oct. 1996, doi: 10.1007/BF00223552.

[103] S. Hallström, 'Glass fibre reinforcement around holes in laminated timber beams', 95, 1995.

[104] L. Höfflin, 'Runde Durchbruche in Brettschichtholzträger - Experimentelle und theoretische Untersuchungen.', Ph.D Dissertation, University of Stuttgart, MPA Otto-Graf-Institute, 2005.

[105] S. Aicher, 'Tragfähigkeit und Bemessung von Brettschichtholzträgern mit runden Durchbrüchen - Sicherheitsrelevante Modifikationen der Bemessungsverfahren nach Eurocode 5 und DIN 1052', *Baufachinformation*, 2006. https://www.baufachinformation.de/mobil/forschungsbericht/tragfaehigkeit-und-bemessung-von-brettschichtholztraegern-mit-runden-durchbruechen-sicherheitsrelevante-modifikationen-der-bemessungsverfahren-nach-eurocode-5-und-din-1052/226643 (accessed Apr. 19, 2022).

[106] A. Karimi-Nobandegani and H. Valipour, 'Timber beams with openings: Laboratory testing and nonlocal finite element modelling', *Engineering Structures*, Oct. 2021, doi: 10.1016/j.engstruct.2021.112867.

[107] 'Timber structures - Glued laminated timber and glued solid timber - Requirements', EN 14080, 2013.

[108] 'K-Bjelke og K-Bjelke Plus SINTEF Certification'. https://www.sintefcertification.no/product/index/357 (accessed Feb. 09, 2022).

[109] MetsäWood, 'Declaration of Performance - NO. MW/PW/421-001/CPR/DOP', 2019, [Online]. Available: https://www.metsawood.com/global/Tools/DoP/Pages/DOPSearch.aspx

[110] ‘Timber structures - Structural timber and glued laminated timber - Determination of some physical and mechanical properties’, EN 408, 2010.

[111] Correlated Solutions, ‘Speckle Kit User Manual’. Unknown date.

[112] ‘Correlated Solutions – Products’. https://www.correlatedsolutions.com/products/ (accessed Apr. 23, 2022).

[113] H. Danielsson and P. J. Gustafsson, ‘A three dimensional plasticity model for perpendicular to grain cohesive fracture in wood’, *Engineering Fracture Mechanics*, Jan. 2013, doi: 10.1016/j.engfracmech.2012.12.008.

[114] C. Gerrand, ‘The equivalent orthotropic elastic properties of plywood’, *Wood Sci. Technol.*, Dec. 1987, doi: 10.1007/BF00380201.

[115] I. M. Sobol’, ‘Global sensitivity indices for nonlinear mathematical models and their Monte Carlo estimates’, *Mathematics and Computers in Simulation*, Feb. 2001, doi: 10.1016/S0378-4754(00)00270-6.

[116] SALib Documentation, ‘FAST - Fourier Amplitude Sensitivity Test’. [Online]. Available: https://salib.readthedocs.io/en/latest/api.html

[117] ‘SciPy v1.8.0 Manual’. https://docs.scipy.org/doc/scipy/reference/generated/scipy.optimize.differential_evolution.html (accessed May 17, 2022).

[118] R. Storn and K. Price, ‘Differential Evolution – A Simple and Efficient Heuristic for global Optimization over Continuous Spaces’, *Journal of Global Optimization*, Dec. 1997, doi: 10.1023/A:1008202821328.

[119] D. P. Pasca, A. Aloisio, M. Fragiacomo, and R. Tomasi, ‘Dynamic Characterization of Timber Floor Subassemblies: Sensitivity Analysis and Modeling Issues’, *Journal of Structural Engineering*, Dec. 2021, doi: 10.1061/(ASCE)ST.1943-541X.0003179.

12 Appendices

The list below provides an overview of the content in all appendices:

A. The Norwegian Institute of Wood Technology conducted Experiments on beams with equal dimensions and modifications as in this thesis.
B. Documentation of the LVDT calibration procedure.
C. Data from moisture content readings.
D. Collection of pictures and illustrations gathered from post-processing of DIC and ACDM results
E. A sample of the data gathered from DIC and ACDM is listed, which is a part of the suggested model-updating procedure
F. Contours of the finished Finite Element model

Additional electronic appendices:

- A3-Poster
- Actuator, load, and displacement data are within the Excel file, and the DIC extracted data.
- CSV file of numerical analysis
- Python code of the models and analyses (Note: copy the model code into the ABAQUS command line)

Model data and python code can be shared upon request.

A. Experimental results (by NIWT)

These experiments were conducted by the Norwegian Institute of Wood Technology before this project, with the same beam and hole configurations as in the present work. Table 12.1 shows the maximum force, displacement

Table 12.1: (Source is raw data from NIWT)

Experiment number	Max Force [kN]	Displacement at max F [mm]	E [MPa]
1	12,52	39,7	10497,0
2	15,50	46,3	10832,7
3	14,26	49,0	11466,8
4	14,26	51,7	11249,0
5	15,54	57,0	10658,1
6	14,88	44,4	11164,4
7	13,82	48,5	11335,8
8	14,60	45,6	10343,1
9	14,66	50,2	10313,7
10	14,70	46,4	11414,9
mean	**14,47**	**47,9**	**10928**
std	0,87	4,64	452,1

B. Calibration of LVDT equipment

Details on how the LVDT signal is recalibrated are described in this appendix.

Creating a line of the first and last non-zero point of the signal output data, as shown in Table 12.2, the straight line can be expressed as:

$$y = mx + b \quad \Rightarrow \quad y \approx \frac{13}{25}x - \frac{27}{10} \tag{12.1}$$

Assuming the measured distance of the LVDT to be $y = x$, then the calibration formula is:

$$x \approx \frac{y + 2{,}7}{0{,}52} \tag{12.2}$$

Where x is the recalibrated distance and y is the signal output. This gives an accuracy of ± 1 mm but can be further reduced by slightly adjusting the formula to:

$$x \approx \frac{y + 2{,}3}{0{,}52} \tag{12.3}$$

This results in an accuracy interval of approximately ± 0,8 mm, as presented in Table 12.2.

Table 12.2: Data used for recalibrating the LVDT output. The signal output presented in the table is the average of three measurements.

Measured stroke length on the LVDT [mm]	Signal output, avg. n=3 [mm]	Recalibrated according to eq. (12.3) [mm]	Difference [mm]
0	0	0	0
30,0	12,9	29,2	-0,8
60,0	28,5	59,2	-0,8
90,0	44,3	89,6	-0,4
120,0	60,1	120,0	0
150,0	75,7	150,0	0
180,0	91,7	180,8	+0,8
210,0	107,2	210,6	+0,6
240,0	122,1	239,2	-0,8

C. Moisture content

Moisture content was measured using electronic apparatus. Values in Table 12.3 are rounded to the closest 0,5 value because of difficulties reading precise decimal values.

Table 12.3: Moisture content of each experiment.

Measured point x [m]	Moisture content [%]			
	A1	A2	B1	B2
1	9,5	11,5	11,5	9,5
2	10,5	12,0	11,5	10,5
3	13,0	12,5	12,0	12,0
4	11,0	11,0	12,0	13,0
5	10,0	10,5	12,5	12,0
mean	**11,0**	**11,5**	**12,0**	**11,5**

D. DIC and ACDM post-processing pictures

Illustrations of ACDM contours of A1 and A2 are shown in this annex. Additionally, the contour of strain perpendicular and parallel to grain from DIC are shown. Lastly, two photographs show the failure mode of the unreinforced beams. The reinforced beams were not photographed because cracks were not visible in the middle of the beams when not loaded.

Figure 12.1: ACDM crack contour plot of specimen A1 before complete failure

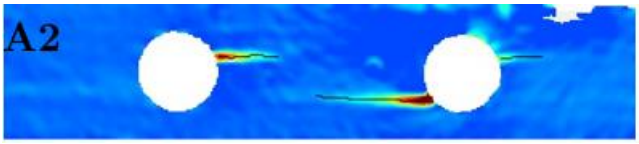

Figure 12.2: ACDM crack contour plot of specimen A2 before complete failure

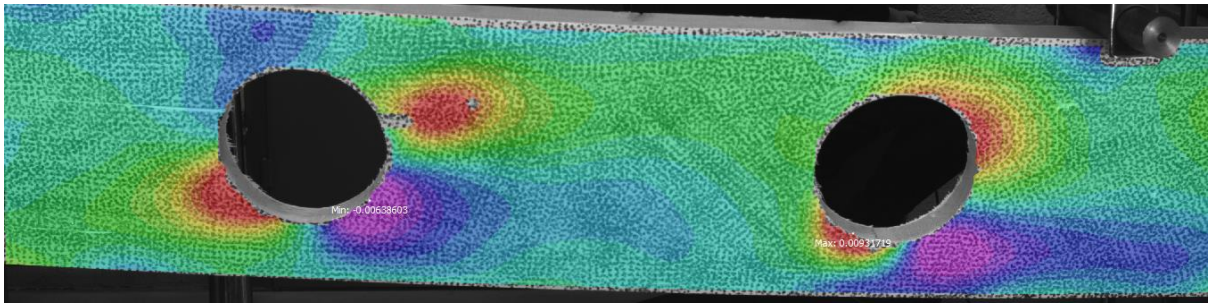

Figure 12.3: Contour plot (ε_{yy}) of specimen A1 with a step size of 20.

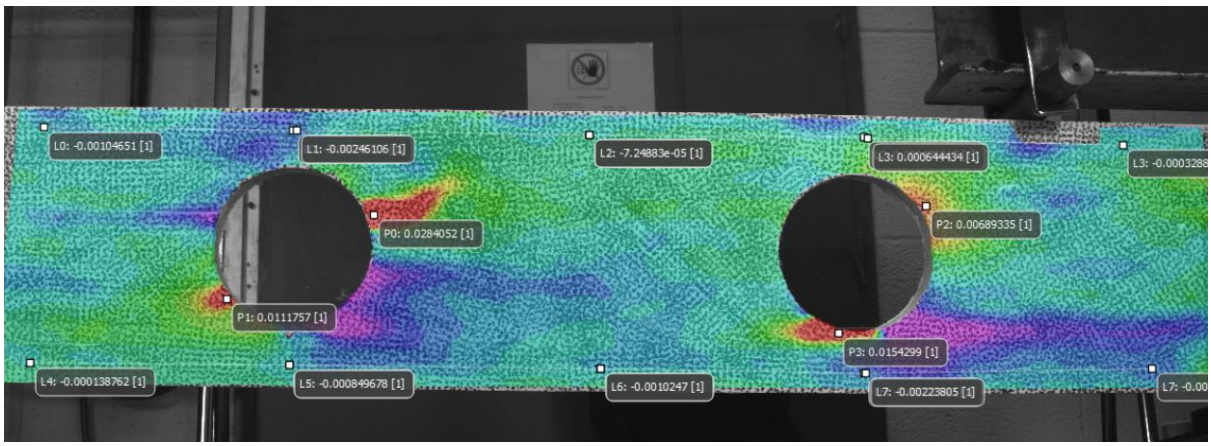

Figure 12.4: Contour plot (ε_{yy}) of specimen A1 with a step size of 10 showing significantly more details and fewer grey areas around the hole vicinity.

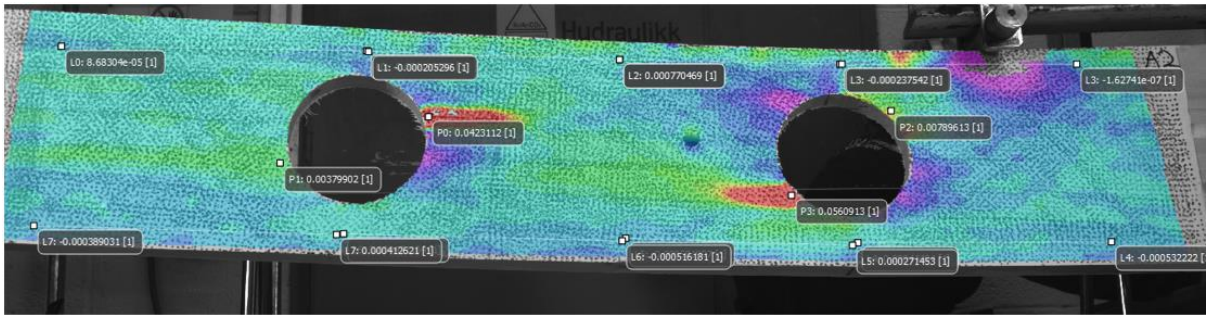

Figure 12.5: Contour plot (ε_{yy}) of specimen A2 with step size 10.

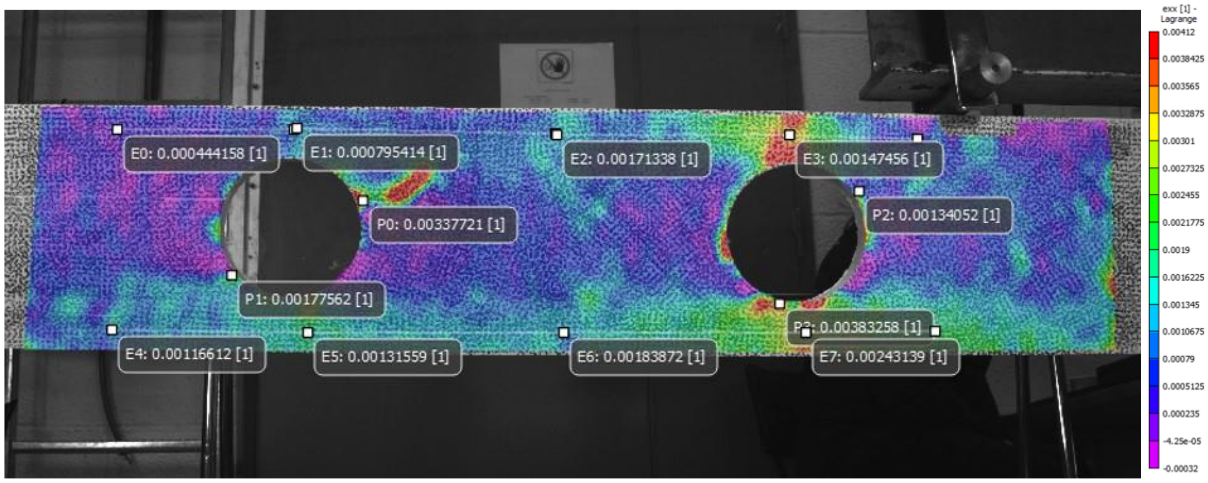

Figure 12.6: DIC contour of A1 (ε_{xx}).

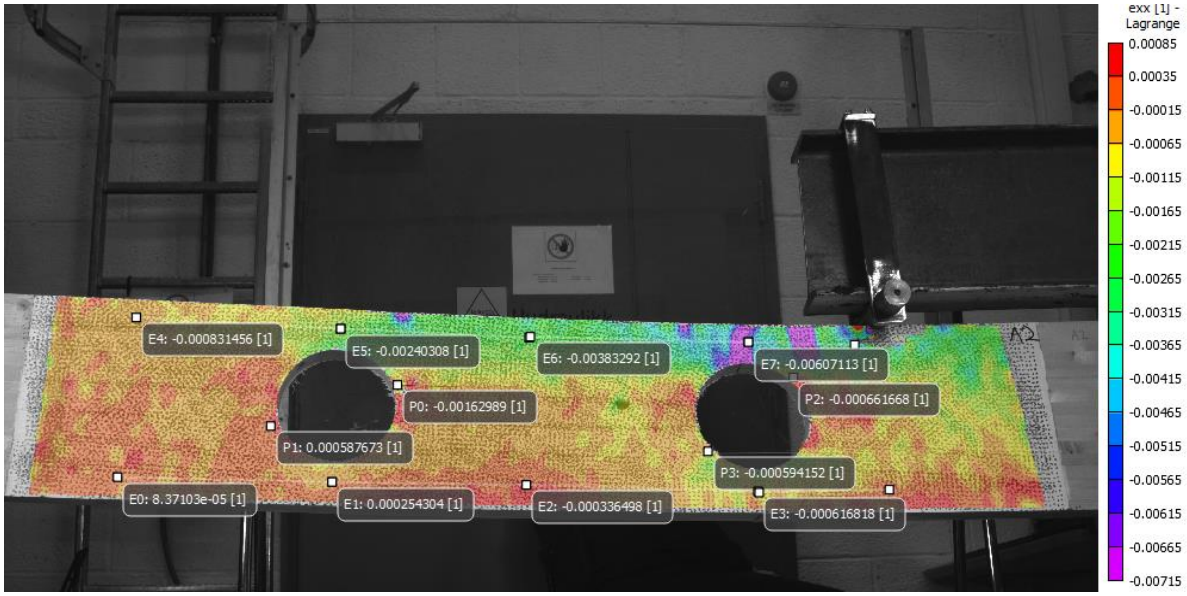

Figure 12.7: DIC contour of A2 (ε_{xx}).

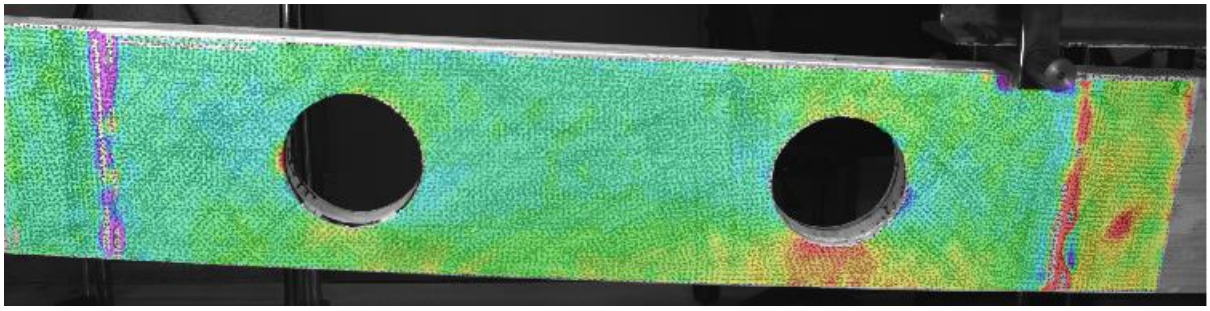

Figure 12.8: Contour plot (ε_{xx}) of reinforced specimen B2 with a step size of 10. The picture shows the largest strains at the transition of reinforcement. Some grey areas are due to depth differences.

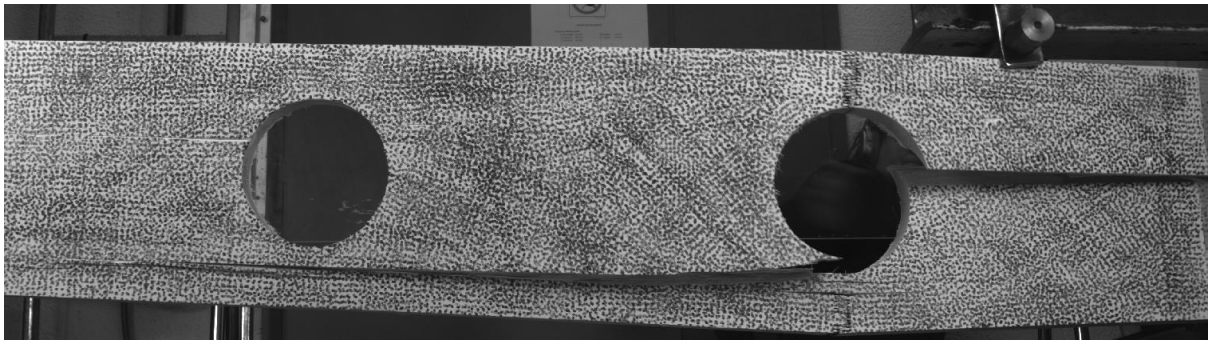

Figure 12.9: Failure cause of A1: Tensile stress perpendicular to the grain.

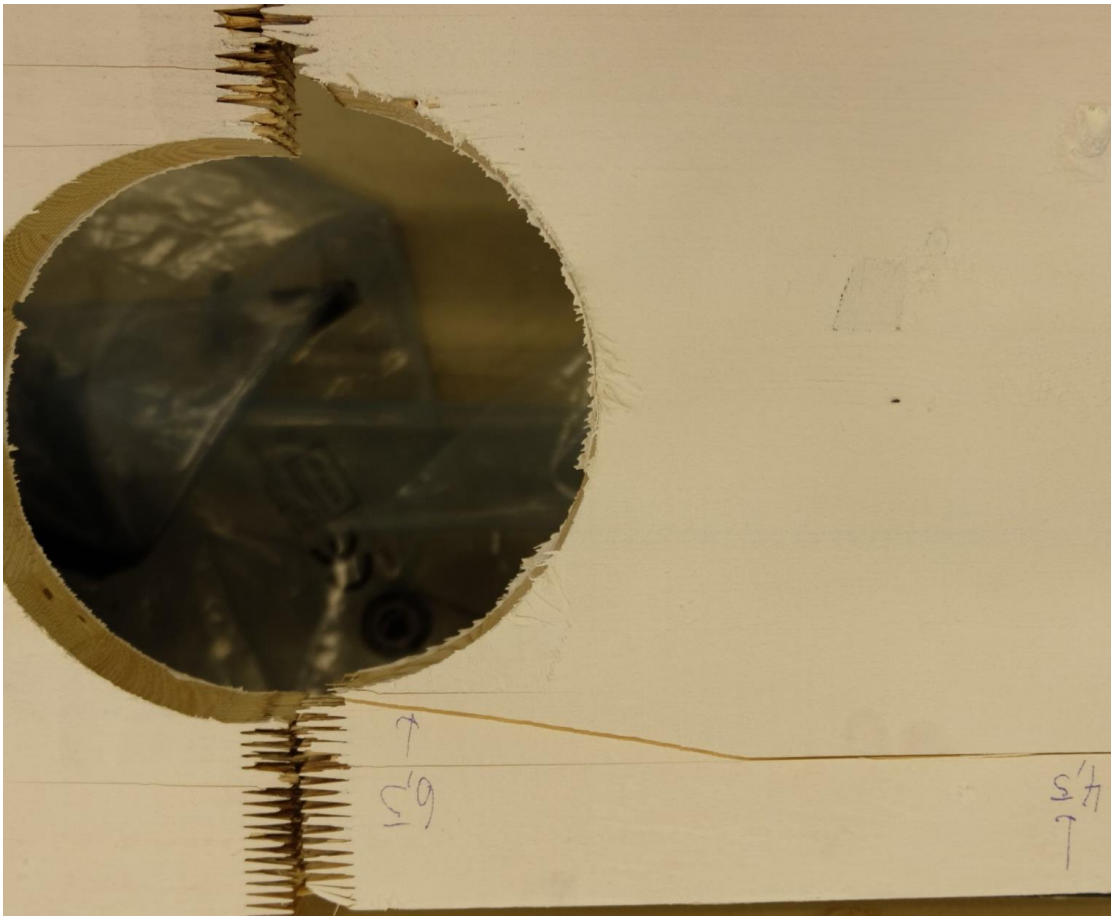

Figure 12.10: Failure cause of A2 at the right hole. Tensile stress perpendicular to the grain and finger-joint failure.

E. Strain and crack data at displacement points

Table 12.4: Experimental data at specific points (A1). Each point is displayed in Figure 7.3. Surface (S) 1 and 2 are the bottom-left and upper-right crack planes of the first (left) hole.

A1		Displacement [mm]									
		4	8	12	16	20	24	28	32	36	40
e_{xx} [10^{-4}]	P0	-0.163	1.635	3.618	2.277	3.680	3.347	4.269	3.686	5.640	6.225
	P1	-0.867	1.880	0.889	2.895	2.247	4.611	5.099	5.771	5.789	7.845
	P2	-0.557	2.997	3.837	5.572	7.734	6.832	9.416	10.624	12.311	15.921
	P3	0.730	-2.939	-1.260	-1.613	-2.710	-3.469	-4.933	-5.023	-5.837	-3.336
	P4	0.001	-1.154	-0.417	-1.888	-3.864	-3.741	-4.929	-4.227	-5.081	-2.696
	P5	-2.959	-4.032	-4.990	-6.786	-9.692	-8.586	-8.370	-10.699	-11.576	-10.655
e_{yy} [10^{-4}]	P6	0.695	2.159	4.123	6.255	9.501	12.056	14.779	16.890	18.834	20.937
	P7	1.787	3.065	6.700	7.905	9.507	12.002	14.008	15.901	17.695	17.009
	P8	0.460	3.716	5.919	8.059	10.382	13.152	15.959	20.741	24.295	40.067
	P9	0.952	2.296	1.982	3.523	3.862	5.180	5.409	7.074	5.704	2.162
a [mm]	S1	0	0	0	0	0	0	37	71	71	71
	S2	0	0	0	0	32	56	56	71	71	71

Table 12.5: Experimental data at specific points (A2). Each point is displayed in Figure 7.7. Surface (S) 1 and 2 are the bottom-left and upper-right crack planes of the first (left) hole.

A2		Displacement [mm]									
		4	8	12	16	20	24	28	32	36	40
e_{xx} [10^{-4}]	P0	1.296	2.439	3.382	3.729	4.828	5.052	6.173	5.964	8.221	9.429
	P1	3.497	5.022	5.863	7.707	9.843	11.795	14.273	16.092	17.455	19.628
	P2	-0.515	0.669	1.197	3.756	4.234	6.241	7.862	7.444	12.535	14.830
	P3	-1.880	-1.535	-1.422	-2.390	-1.999	-1.372	-2.339	-1.544	0.371	1.277
	P4	-0.047	-2.903	-3.674	-3.783	-5.824	-5.418	-7.341	-6.753	-8.425	-8.049
	P5	-0.408	-2.532	-4.466	-4.854	-6.626	-8.402	-11.265	-13.344	-13.581	-20.547
e_{yy} [10^{-4}]	P6	1.049	1.068	2.164	2.443	3.344	3.291	3.875	2.819	1.839	-0.971
	P7	0.930	2.368	4.184	4.506	6.517	9.344	9.726	11.613	13.008	15.624
	P8	0.493	2.694	3.457	5.381	7.115	8.654	9.889	12.480	14.071	15.709
	P9	1.616	1.815	2.890	3.770	6.002	6.495	7.204	8.453	9.015	10.170
a [mm]	S1	0	0	0	0	0	0	0	0	0	0
	S2	0	0	0	0	0	0	40	91	91	134

F. Finite Element model contour

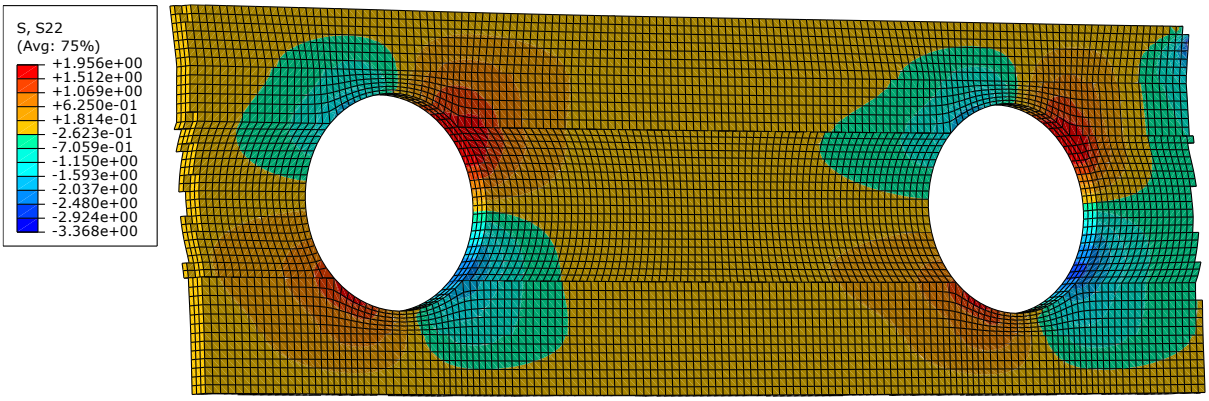

Figure 12.11: Increment 30 of the FE-model

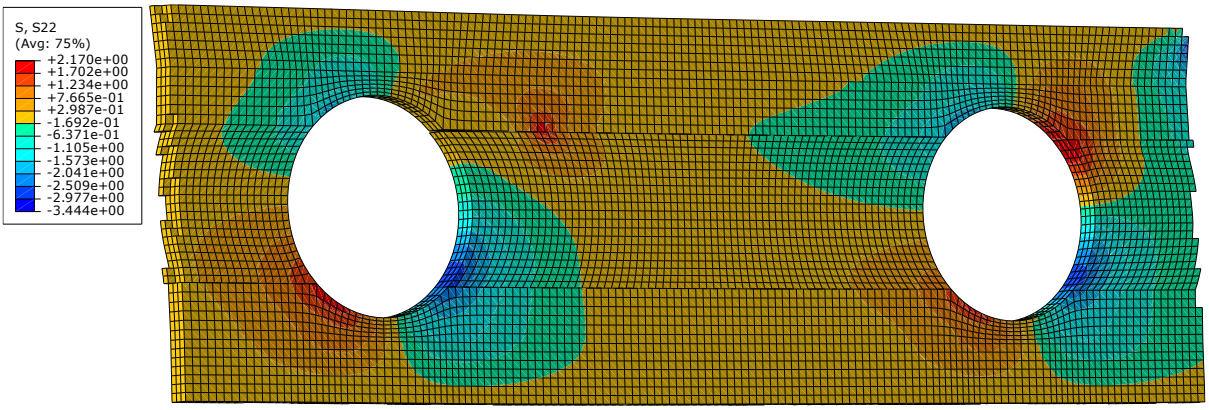

Figure 12.12: Increment 60 of the FE-model

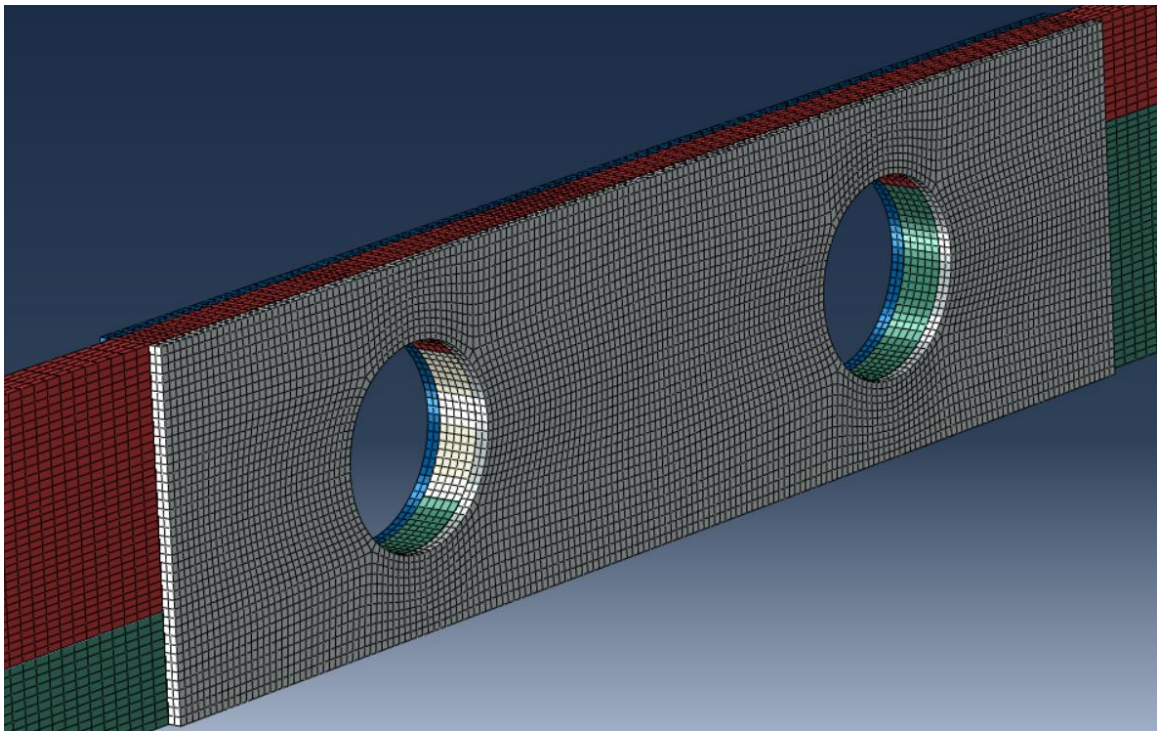

Figure 12.13: Mesh of a reinforced model. This was not analyzed due to the twisting of the beams.